Loss analysis of back-contact back-junction thin-film monocrystalline silicon solar cells

Von der Fakultät für Mathematik und Physik
der Gottfried Wilhelm Leibniz Universität Hannover
zur Erlangung des Grades
Doktor der Naturwissenschaften
Dr. rer. nat.
genehmigte Dissertation

von
Dipl.-Phys. Felix Haase
geboren am 18.08.1981 in Nürnberg

2013

Referent: Prof. Dr. Rolf Brendel
Korreferent: Prof. Dr. Jörg Osten
Tag der Promotion: 07.02.2013

Abstract

This work presents the fabrication of novel solar cell devices as well as a power loss analysis by free energy loss analysis based on recombination and transport losses determined in this work. Using the porous silicon (PSI) process we fabricate $30\,\mu$m to $45\,\mu$m thin monocrystalline silicon layers. The PSI process avoids high energetic process steps and reduces the material loss per layer to a $2\,\mu$m thin separation layer. In contrast, by conventional sawing $120\,\mu$m silicon per wafer are lost. Within this work we fabricate back-contact back-junction solar cells from these layers, where the whole metallization is on the cell rear side. Thus shading losses by front side metallization are avoided and the cell interconnection is simplified.

The conversion efficiency of a monocrystalline silicon solar cell is determined by generation, recombination and transport losses. The determination of these losses and the impact on the conversion efficiency allows for increasing the conversion efficiency. For the first time these losses are analyzed for thin epitaxial layer cells. The generation in the solar cells is determined by simulations which uses measured layer properties as input parameters. Measured and simulated reflection are in agreement. The recombination in the volume and at the passivated and metalized surfaces of the epitaxial layers are determined by lifetime measurements on test samples processed in parallel to the solar cells. The recombination parameters are the boundary conditions of the simulation of a two-dimensional unit cell of the solar cell. Afterwards a network simulation combines several two-dimensional unit cells to consider resistances at the contacts and in the metal. A free energy loss analysis is capable for comparing all recombination and transport power losses. The analysis shows the main loss mechanisms of the different thin-film back-contact back-junction solar cells: base contact recombination, base recombination and transport losses in the base and at the contacts at a low base doping concentration. A low diffusion length of $84\,\mu$m in silicon combined with $250\,\mu$m wide base fingers lead to a power loss by Shockley-Read-Hall recombination of 5.3 % absolute. A low base doping of $1.5 \times 10^{15}\,\mathrm{cm}^{-3}$ causes a power loss by transport losses in the base of up to 2.2 % absolute. A base doping of $3 \times 10^{16}\,\mathrm{cm}^{-3}$ in combination with a saturation current density of $50000\,\mathrm{fA\,cm}^{-2}$ at the base contacts causes an efficiency loss of 1.9 % absolute.

The first cells fabricated in this work are supported mechanically and have a conversion efficiency of 13.5 %. An increase in free energy density of generation from $189\,\mathrm{Wm}^{-2}$ to $232\,\mathrm{Wm}^{-2}$ by the implementation of a texture, a decrease of the free energy density of recombination at the base contact recombination from $25\,\mathrm{Wm}^{-2}$ to $5\,\mathrm{Wm}^{-2}$ by the implementation a back surface field and a decrease of the free energy density of recombination in the bulk from $53\,\mathrm{Wm}^{-2}$ to $8\,\mathrm{Wm}^{-2}$ by an enhancement in epitaxial layer quality leads to an increase of the conversion efficiency of the cell of 18.8 %.

Furthermore this work introduces layer-selective laser ablation (LASA) that allows for a damage free contact formation and has the potential to reduce base contact recombination even further.

Keywords: thin-film monocrystalline back-contact back-junction silicon solar cell, free energy loss analysis, layer selective laser ablation

Kurzzusammenfassung

Diese Arbeit stellt sowohl die Herstellung neuartiger Solarzellen vor als auch erstmals eine Leistungsanalyse mittels freier Energie Verlustanalyse auf Basis in dieser Arbeit bestimmter Transport- und Rekombinationsparameter. Mit Hilfe des porösen Silicium (PSI) Prozesses können 30 μm bis 45 μm dünne monokristalline Siliciumschichten hergestellt werden. Der PSI Prozess vermeidet hochenergetische Prozessschritte und reduziert den Materialverlust pro Schicht auf eine 2 μm dünne Trennschicht. Beim konventionellen Sägen gehen dagegen 120 μm Silicium pro Wafer verloren. Aus diesen Schichten stellen wir im Rahmen dieser Arbeit Rückkontaktsolarzellen her, bei denen sich die gesamte Metallisierung auf der Rückseite befindet. Dadurch entfallen die Abschattungsverluste einer Vorderseitenmetallisierung und die Verschaltung im Modul vereinfacht sich.

Der Wirkungsgrad einer monokristallinen Siliciumsolarzelle wird durch die Generation, die Rekombination und die Transportverluste bestimmt. Die Bestimmung dieser Verluste und des Einflusses auf den Wirkungsgrad ermöglicht die Erhöhung des Wirkungsgrads. Diese Verluste werden in dieser Arbeit erstmals für Zellen aus dünnen Epitaxieschichten analysiert. Die Generation in den Solarzellen wird durch eine Simulation bestimmt, die gemessene Schichteigenschaften als Eingangsparameter verwendet. Gemessene und simulierte Reflexion stimmen dabei überein. Die Rekombination im Volumen der Epitaxieschicht und an den passivierten und metallisierten Oberflächen wird mit Hilfe von Lebensdauermessungen an Teststrukturen ermittelt welche parallel zu den Zellen gefertigt werden. Die so bestimmten Rekombinationsgrößen werden in einer Simulation einer zweidimensionalen Einheitszelle der Solarzelle als Randbedingungen verwendet. Durch eine Netzwerksimulation werden anschließend mehrere zweidimensionale Einheitszellen miteinander verbunden, um Widerstände an den Kontakten und im Metall zu berücksichtigen. Eine freie Energie Verlustanalyse ermöglicht den Vergleich aller Rekombinations- und Transportverluste. Die Ergebnisse dieser Verlustanalyse zeigen die Hauptverlustfaktoren für die unterschiedlichen Dünnschicht-Rückkontaktsolarzellen: Basiskontaktrekombination, Rekombination in der Basis und Transportverluste in der Basis und an den Kontakten bei niedrigen Basisdotierungen. Niedrige Diffusionslängen der Elektronen von 84 μm im Silizium und 250 μm breite Basisfinger führen zu einem Leistungsverlust durch Shockley-Read-Hall Rekombination von 5.3 % absolut. Eine geringe Basisdotierung der Solarzelle von 1.5×10^{15} cm^{-3} verursacht einen Leistungsverlust durch Transportverluste in der Basis von bis zu 2.2 % absolut. Eine Basisdotierung von 3×10^{16} cm^{-3} in Kombination mit einer Sperrsättigungsstromdichte von 50000 fA cm^{-2} führt zu einem Leistungsverlust durch Basiskontaktrekombination von bis zu 1.9 % absolut.

Die erste in dieser Arbeit hergestellte Rückkontaktzelle ist mechanisch unterstützt und hat einen Wirkungsgrad von 13.5 %. Eine Erhöhung der freien Energiedichte der Generation von 189 Wm^{-2} auf 232 Wm^{-2} mit der Einführung einer Textur, der Reduzierung der freien Energiedichte der Basiskontaktrekombination von 25 Wm^{-2} auf 5 Wm^{-2} mit der Einführung eines Rückseitenfeldes und einer Reduzierung der freien Energiedichte der Basisrekombination von 53 Wm^{-2} to 8 Wm^{-2} mit der Erhöhung der Epitaxieschichtqualität führen zu einer Erhöhung des Wirkungsgrads der Zelle auf 18.8 %.

Außerdem führt diese Arbeit eine Layer-selective Laser Ablation (LASA) ein, die eine schadensfreie Kontaktbildung ermöglicht und so potentiell die Basiskontaktrekombination noch weiter reduziert.

Schlagwörter: Monokristalline Dünnschicht-Silicium-Rückkontaktsolarzelle, Freie Energie Verlustanalyse, Schichtselektive Laser Ablation

Contents

1 Introduction

The current trend in crystalline silicon solar cell production is towards thinner silicon wafers to save material and energy consumption [1,2]. The saved material and energy consumption should lead to reduced economic and energetic payback periods. The production of the material requires many energy consuming steps. First quartz sand is reduced with carbon at 1800°C to metallurgical silicon. To clean the silicon, it is converted to trichlorosilane by using hydrochloric acid, and is then distilled at 300°C before it is reduced back to silicon by hydrogen at 1100°C. The produced polycrystalline silicon has many crystallographic defects and cannot be used for silicon wafer and solar cell production. Instead, the silicon is molten in a crucible, after which a monocrystalline seed crystal is dipped into the melt and raised slowly, so that a monocrystalline silicon ingot will grow from the seed crystal. The ingot is commonly cut into wafers by a wire saw. The silicon loss during wafering is technologically limited to 120 μm. Thus, at a wafer thickness of 180 μm 40 % of the material is lost due to sawing [3].

To avoid this material loss the <u>p</u>orous <u>si</u>licon (PSI) process [4] has been introduced. This process allows for a much lower material consumption than standard crystalline silicon solar cell processes. A thin monocrystalline layer is grown on a thick substrate wafer by an epitaxial chemical vapor deposition, which has a thickness of $10 - 50\,\mu$m. The epitaxial layer grown on a thick substrate wafer is lifted off the substrate wafer by using a separation layer which was etched into the substrate wafer before epitaxy. After lift-off the epitaxial layer can be processed further to a solar cell whereas the substrate wafer can be re-used for many more PSI processes [5]. An epitaxial cell with a thickness of 30 μm consumes roughly 32 μm silicon including 2 μm which are used for forming the porous layers whereas a wafer cell with a thickness of 180 μm consumes 300 μm silicon including 120 μm which are lost due to sawing the wafers. Therefore the PSI process saves 89 % silicon per cell but still keeps a high efficiency potential.

The focus of this work is the development and loss analysis of high efficiency back-contact back-junction (BC BJ) thin-film monocrystalline silicon solar cells fabricated by the PSI process. For this analysis the BC BJ PSI cells are measured with different cell characterization techniques such as current-voltage characteristics, electroluminescence [6], photoluminescence [7], and quantum efficiency, allowing the determination of the power output, recombination parameters, and series resistance losses. However a full interpretation of these measurements is only possible with analytical models, which are not available for a BC BJ cell. Instead, for the first time the complete BC BJ PSI cell is simulated by combining optical ray-tracing simulations with finite element simulations of a unit cell and network simulations. Figure 1.1 shows the analysis sequence that we used for the BC BJ solar cell characterization.

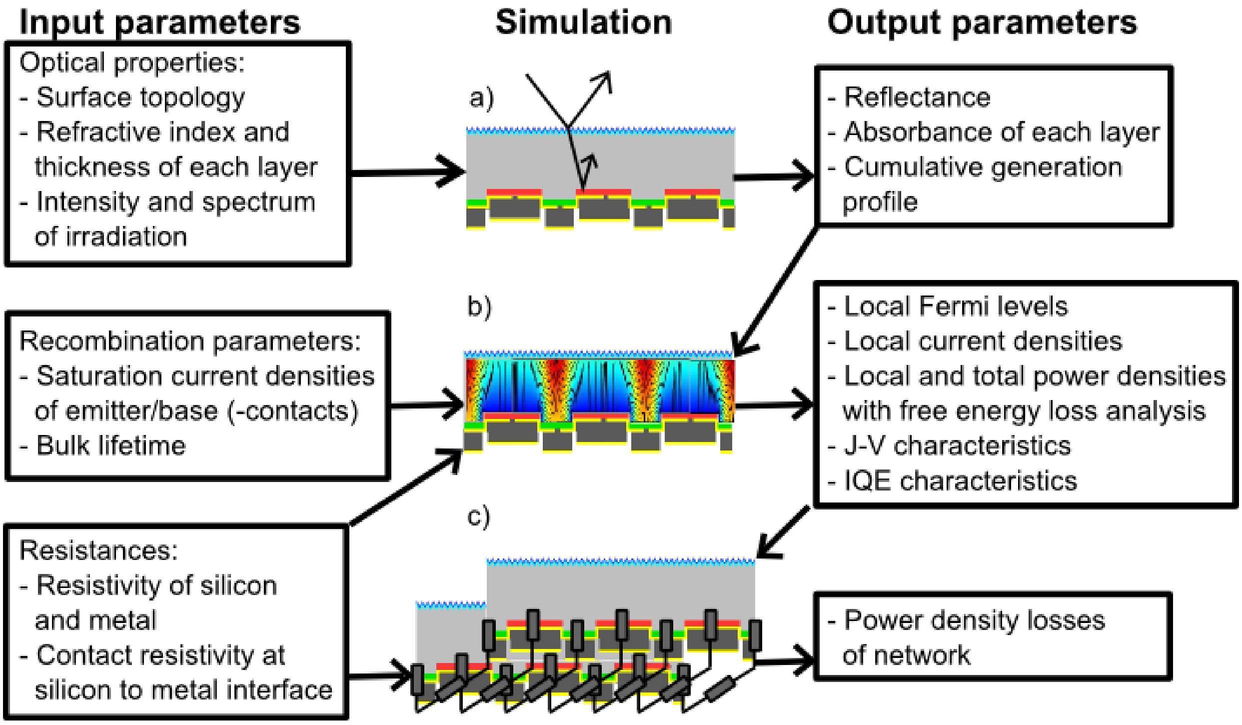

Figure 1.1: *Analysis sequence for BC BJ solar cell characterization. The left column shows the input parameters for the simulations shown in the center whereas the right column shows the output parameters of these simulations. The output parameters of the ray tracing simulation (a) are applicable for an optical loss analysis. The unit cell simulation (b) in combination with the free energy loss analysis allows for the recombination as well as resistance power density loss analysis. The network simulation (c) yields the resistance network power density losses. These three simulations consider all relevant losses in the BC BJ PSI solar cell.*

We first perform a optical simulation (Figure1.1a), which yields the optical losses and a generation profile. This generation profile and measured recombination and resistance parameters are input parameters for the unit cell simulation (Figure1.1b). Using the unit cell simulation we determine the power losses by mechanism and a current-voltage curve. Finally, a network simulation accounts for series resistance losses between the unit cells (Figure1.1c). We determine all recombination and resistance input parameters by analysis of measurements yielding reliable values for reasonable simulation results. The saturation current densities and bulk lifetimes are determined by lifetime measurements on test samples processed in parallel to the cells, as shown in Section 4.3 on page 40. We determine the series resistances on test samples by four point probe measurements [8] and the transfer length method (TLM) [9], as described in Section 5 on page 53. Free energy loss analysis (FELA) [10] uses the results of the unit cell simulation to determine power losses of the unit cell, as shown in Section 6.2 on page 60. After the investigations on the loss mechanisms of the cell, the efficiency potential of this technology can be calculated accurately. The potential efficiency of a 45 μm thick BC BJ PSI cell is calculated to be more than 21 %.

This efficiency is close to the 22 % possible on a 290 μm-thick wafer using the same process sequence which is used for the development of the BC BJ PSI cells. The main loss of this cell concept is the recombination at the base finger and the base contacts.

To reduce the recombination at the base contact this work introduces a process which allows for contact formation without causing damage. For the low recombination of the rear side of the cell the whole area is passivated by a dielectric layer stack. For contact formation the upper insulating layer has to be removed locally. In this work the layer selective laser ablation process (LASA) is developed, which removes only the insulating layer selectively from the amorphous silicon passivation layer. No defects are introduced in the cell base or in the passivation layer by the LASA process. Compared to other techniques this method is faster and requires no additional masking steps such as ink-jet printing. Low resistive contacts form after metal deposition by the COSIMA process [11]. This process is especially useful for contacting thin emitters avoiding shunting.

Chapter 2 describes the porous silicon process and the fabrication of PSI cells and modules. It provides a short overview of the front junction cells processed prior to this work. Afterwards it focuses on the different process sequences and results of BC BJ cells which are developed in this work. It also shows for the first time a new concept for the all in one cell metallization and cell interconnection for BC BJ PSI cells.

Chapter 3 analyzes the current-voltage characteristics and quantum efficiency measurements of the BC BJ cells investigated in this work. The recombination and series resistance is quantified by applying a two diode model to the current voltage characteristics.

Chapter 4 deals with the determination of the saturation current densities of the cell surfaces and the bulk lifetime of the epitaxial layers on test samples. It reviews recombination mechanisms in silicon solar cells which are necessary for this determination. Furthermore it describes the different techniques for the measurement of the carrier lifetime of the test samples. These measurements are required for the determination of saturation current densities and bulk lifetimes which are input parameters in the cell simulation. We describe the sample preparation and the procedure of evaluation of the determination of the saturation current densities and discuss the results which are input parameters for the cell simulations.

Chapter 5 reflects the methods for the determination of the resistances of all the materials and interfaces used in this work. It describes the four point probe measurement used for the determination of the silicon and metal resistivity and it introduces the transfer length method (TLM) [9] for the determination of the silicon to metal interface. The results are also input parameters for the cell simulations.

Chapter 6 shows the simulation procedure performed on the base of the analyzed saturation current densities, bulk lifetimes and resistances. A raytracing simulation yields a generation profile for the subsequent unit cell simulation as well as the optical losses. A finite element unit cell simulation is combined with a network simulation of the complete cell. The conductive boundary model [12], which is used for the unit cell simulation, and the equivalent circuit for the resistance network simulation are shortly described. The power density losses of each cell part are calculated with the free energy loss analysis [10]. Finally we compare the measured with the simulated current-voltage characteristics and the measured with the simulated quantum efficiencies.

Chapter 7 compares the analyzed power density losses with a loss analysis based on luminescence measurements of the fabricated solar cells. We use electroluminescence measurements for the determination of the diffusion length as well as for qualitative series resistance effects. The series resistance is quantified by the interpretation of photoluminescence measuremets.

Chapter 8 shows the solar cell conversion efficiency in dependence on various limiting loss mechanisms. The analysis is a simulation study which is based on measured parameters which are varied in a physically and technically reasonable range. In addition, we extend the analysis to even thicker, high lifetime wafer based solar cells. We compare measured with simulated extracted power densities in dependence on the limiting loss mechanisms in the cells and analyze how much the power density changes by varying the parameters.

2 Producing cells from the porous silicon process

In the porous silicon process (PSI), an epitaxial layer is the active light absorbing region in the cell and grows on a layer of porous silicon. This porous layer is electrochemically etched into a monocrytalline substrate wafer and later serves as predetermined breaking point during the separation of the epitaxial layer from the substrate. The epitaxial layer is monocrystalline with some crystal defects. Cell concepts which exist for silicon wafers are also applicable to epitaxial layers. Nevertheless, there are some limitations due to the thickness of the epitaxial layer. The risk of breakage of a $40\,\mu$m thin monocrystalline layer is higher than for a $150\,\mu$m thick wafer, especially on large areas. Therefore the layer size is limited to $4\,\mathrm{cm}^2$ during laboratory handling steps or the layer has to be supported mechanically.

The epitaxial layer can be processed into a solar cell by either of two approaches: free standing or mechanically supported. If the layer is free-standing after the lift-off, both sides are open for processing, as would be the case for a wafer. This can be advantageous for process sequences where the upper accessible surface of the epitaxial layer, later the rear side of the solar cell, is processed first. In this process sequence the front surface can be passivated after lift-off but before metallization of the rear side without any additional limitations to temperatures, chemicals or plasmas, as could be the case when using a supporting material in the process sequence. However, a free-standing layer is restricted to small cell areas due to the risk of breaking. This in turn requires a cheap and reliable interconnection technique.

The second approach is to support the epitaxial layer mechanically. Before lift-off the epitaxial layer is mechanically supported by the substrate wafer. After lift-off, the layer can be supported by an evaporated or screen printed metal, a glass pane or an electrostatic chuck. Depending on the technology which is used for supporting the epitaxial layers, limitations to the subsequent process steps occur. These limitations are limitations concerning wet chemical cleaning or etching sequences or the maximum process temperatures during passivation. The protection of one side of the layer can be advantageous for single side processes like texture, diffusions or emitter patterning, however it introduces limitations to the solar cell process sequence since all processes of one side of the cell have to be finished first before the other side can be processed to the end. This limitation in process sequence is especially important for the cell interconnection step. A standard interconnection process connects the contact on the front side of the cell with the contact on the rear side of the next cell. This is obviously not possible for this process sequence where only one side is accessible during interconnection.

2.1 The porous silicon process

The porous silicon process is an approach aiming at a reduced energy and material consumption compared to wafer based approaches. To reach this goal a recycle process of the starting wafer is one of the key features of the porous silicon process. This cycle was already presented by Taynaka [13] and Brendel in 1997 [4] where he showed a lift off of a $2 \times 2\,\mathrm{cm}^2$ and $5.8\,\mu\mathrm{m}$ thick epitaxial layer. The whole process cycle is schematically shown in Figure 2.1.

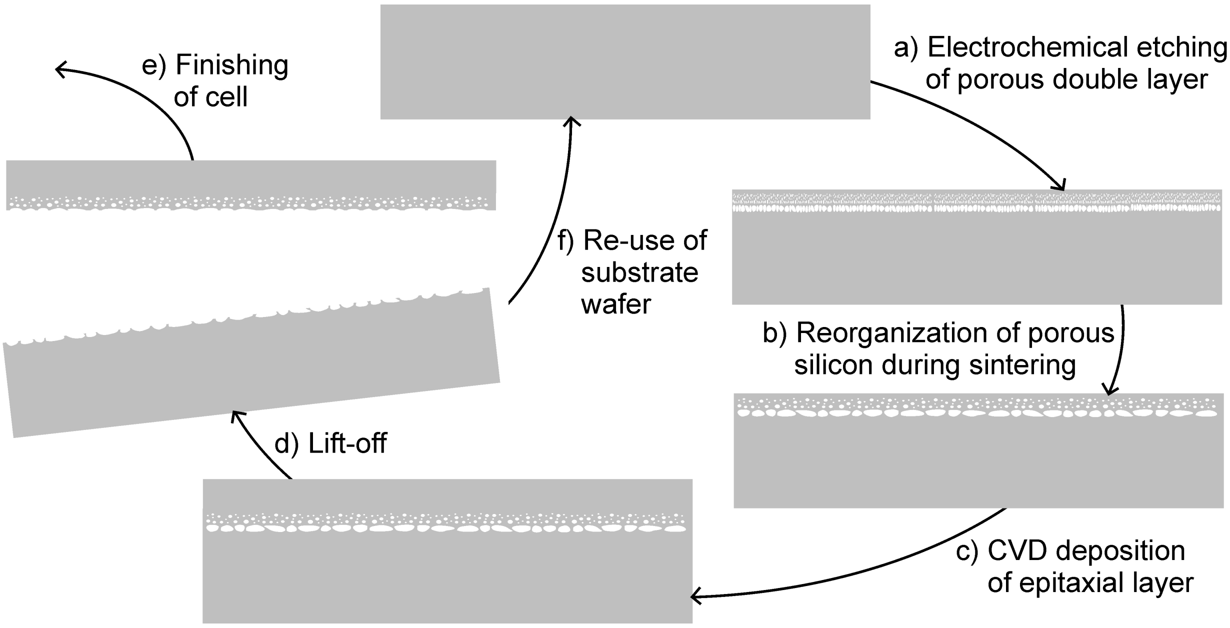

Figure 2.1: *Schematic of the porous silicon process. (a) A porous double layer is electrochemically etched in a substrate wafer. The bottom layer has a high porosity whereas the upper layer has a low porosity. (b) The porous double layer reorganizes during a sintering step in hydrogen at* 1100 °C *(c) An epitaxial Si layer grows in a chemical vapor deposition at* 1100 °C. *(d) The epitaxial layer is lifted-off. The high porosity layer serves as breaking point. (e) The epitaxial solar cell can be finished. (f) The substrate wafer can be reused for the next PSI cycle.*

The upper part of Figure 2.1 shows that the process starts with a thick monocrystalline substrate wafer with a boron doping density of $6 \times 10^{18}\,\mathrm{cm}^{-3}$. A porous double layer is etched electrochemically into the surface of the wafer as described in Figure 2.1a. The bottom layer has a high porosity and serves as a predetermined breaking point for the lift-off process. The upper layer has a low porosity and serves as a seed layer for the subsequent epitaxy of silicon.

Figure 2.1b shows the reorganization of the porous double layer in hydrogen at 1100 °C. The surface of the upper layer closes during this process allowing for a high quality epitaxial layer. A monocrystalline epitaxial layer grows on the closed surface by chemical vapor deposition at 1100 °C as illustrated in Figure 2.1c. This epitaxial layer is the base of the

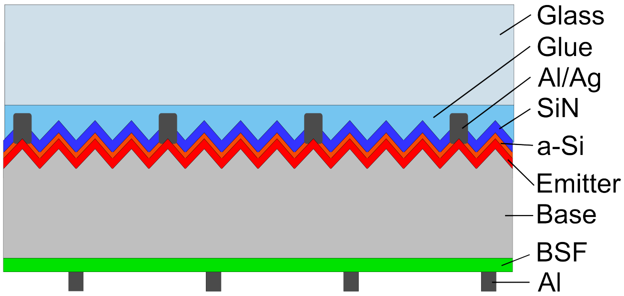

Figure 2.2: *Schematic of the supported large area PSI solar cell with an a-Si/SiN*$_x$ *passivated front side.*

solar cell. The open side is processed as the rear side of the BC BJ cell process while the cell is supported by the substrate wafer.

Figure 2.1d shows the lift-off of the epitaxial layer. A glass is glued to the epitaxial layer for the mechanically supported cell process. The free-standing approach uses a vacuum chuck attached to the epitaxial layer. The epitaxial layer is separated from the substrate wafer by mechanical force. The porous layer with the high porosity serves as breaking point.

Finally the solar cell can be finished by processing the other side of the cell as shown in Figure 2.1e. Figure 2.1f shows the reuse of the substrate wafer for the next PSI cycles. Up to now a ten times reuse of the substrate wafer was demonstrated [5]. Each cycle leads to a silicon loss of approximately 2 μm from the porous layer compared to 120 μm loss by sawing.

2.2 Two sides contacted cells

The first PSI solar cells were processed with the mechanical support of a carrier by Tayanaka et al. [13] demonstrating an efficiency of 12.5 % on a 13 μm thick epitaxial layer on a cell area of 4 cm^2.

On a large area of 95.5 cm^2 Terheiden et al. developed a process which also was supported by a glass carrier [14]. Figure 2.2 shows a schematic cross section of the final cell of Ref. [14]. The textured front surface featured a 70 $\Omega/\square$ phosphorous emitter passivated by amorphous silicon (a-Si) and was additionally coated by silicon nitride (SiN$_x$) for antireflection. The recombination on the rear side was reduced by a 2 μm-thick boron doped back surface field (BSF). The front side was contacted by an Al/Ag front grid evaporated through a metal mask, whereas the rear side was contacted by an Al grid also evaporated through a mask. The cell thickness was 30 μm. The open-circuit voltage was 616 mV whereas the short-circuit current density was 29.0 mA cm^{-2}. The fill factor was 78.8 % resulting in an energy conversion efficiency of 14.1 %. However, the interconnection of such two cells is complicated since the front side is not accessible. A cell which is processed free-standing on the other hand has both sides open for cell interconnection.

The free-standing process was described by Solanki et al. [15]. They produced a free standing 18 μm thick cell with a conversion efficiency of 12 %. Reuter et al. [16] increased

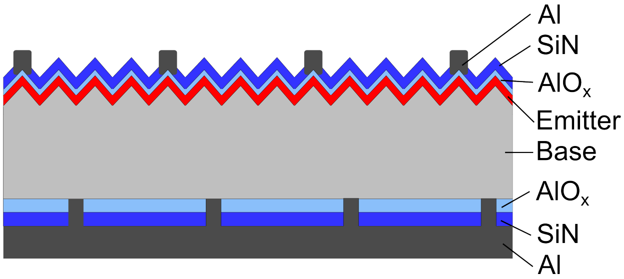

Figure 2.3: *Schematic of the free standing PERC PSI solar cell with* AlO_x *passivation.*

the efficiency of a free standing epitaxial cell to 17 % with a cell area of 1 cm^2 and a thickness of 50 μm. Recently, Petermann et al. further increased the efficiency to 19.1% [17]. Figure 2.3 shows a schematic cross section of the finished cell. The textured front side featured a 100 $\Omega/\square$ phosphorous emitter passivated with a layer stack of AlO_x/SiN_x, which was also serving as antireflection coating. The front side was contacted by an aluminum grid evaporated through a metal mask. An AlO_x tunneling layer on the emitter surface prevents a diffusion of the front contact aluminum through the emitter, which would result in shunting, and also acts as contact passivation. The rear side was also passivated by an AlO_x/SiN_x stack and locally contacted by a full area evaporated aluminum layer serving as rear reflector. The cell has an efficiency of 19.1% independently confirmed by Fraunhofer ISE CalLab, which is the highest efficiency ever reported for any Si layer transfer cell [18]. The open circuit voltage is (650 ± 2) mV and the short circuit current density is (37.8 ± 0.7) mA cm^{-2}. This large short circuit current is possible because the free-standing epitaxial layer avoids optical losses, which would be caused by a glued glass as in the supported case. The fill factor is (77.6 ± 0.5) %.

This cell has both sides accessible for cell interconnection in a module. Common industrial cell interconnection is realized by soldering a connector to the metal contacts on the front and rear side of the cell. For this, common industrial wafer cells have a screen printed silver front grid and screen printed aluminum with silver pads on the rear side [19]. Thin PSI cells, however, have a high risk for breaking due to the mechanical load during screen printing. An alternative is the local evaporation of a solderable metal like silver. Local evaporation requires masking by a metal mask in direct contact to the cell which is probably not industrially feasible. Furthermore the common soldering technique also puts mechanical stress on the thin PSI cell, increasing the risk of breaking. Therefore a back-contact back-junction PSI solar cell is introduced in this work, which can be integrated in a module without screen printing and common soldering technique.

2.3 Back-contact back-junction cells

Back-contact back-junction (BC BJ) silicon solar cells have a higher efficiency potential than both sides contacted cells. Both sides contacted cells have a metal grid on the front side which reflects part of the incident light and reduces the generation in the cell. A BC BJ cell has no metal grid on the front side since it has both contacts on the rear side. This concept increases the generation in the cell but also the number of process steps. A BC BJ cell also shows electrical shading due to recombination at the base contacts [20] which is discussed in this work, too. In the end it is an economical trade-off between costs and power output of the cell and the module. To realize and analyze these concepts is the focus of this work. This work describes for the first time a loss analysis of a PSI-based thin monocrystalline BC BJ cell and the combination of a BC BJ cell process with a cell interconnection technique on porous silicon. In the following we discuss a mechanically supported as well as a free-standing process sequence of a BC BJ cell. We first follow the supported process since these cells can be lifted off with the mechanical support of the glass carrier. The analysis leads to the conclusion that the process limitations of the supported process also limits the efficiency.

2.3.1 Cell interconnection

Both polarities are located at the rear side of the BC BJ cell in contrast to both side contacted cells. This allows for smaller gaps between the cells and a single side connecting process. Nevertheless a common soldering technique requires solderable pads [19] and exposes the cells to mechanical load. An alternative process avoiding solderable pads and reducing the mechanical load for two side contacted cells is shown in [21] whereas Figure 2.4 shows an alternative process for BC BJ cells.

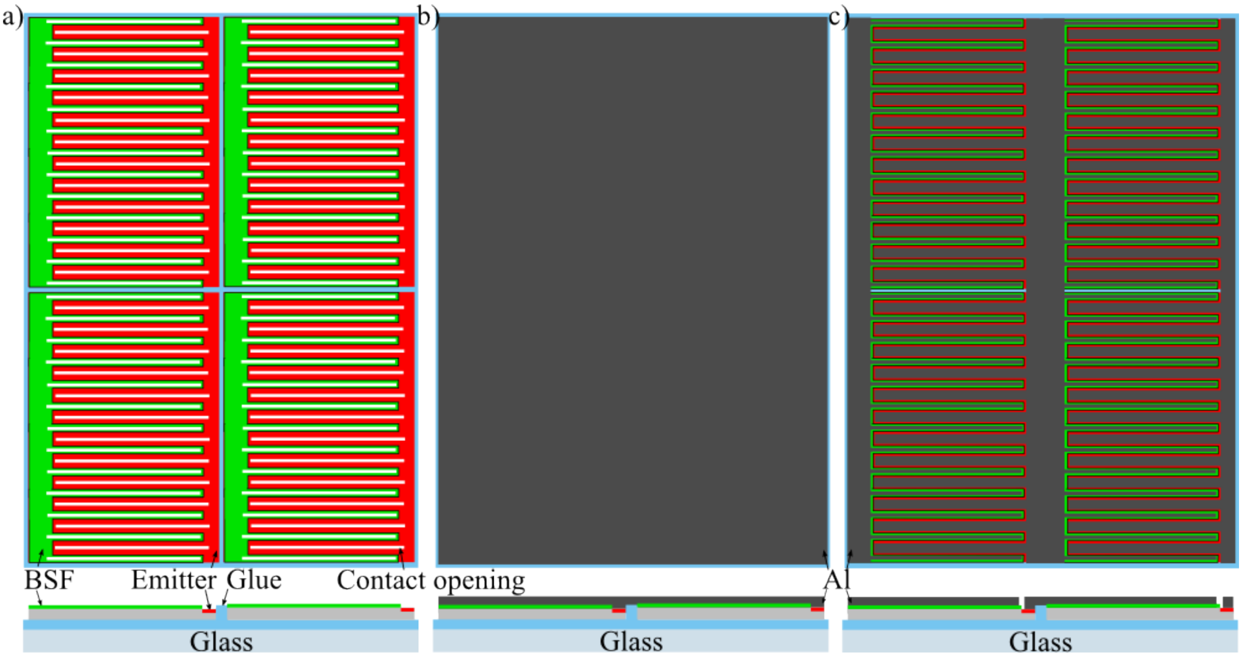

Figure 2.4: *Schematic drawing of the top and the cross section of the BC-BJ PSI module fabrication. This process combines the metallization and cell interconnection in one step. (a) shows the lay-up of the cells on a glue coated module glass. The glue enters the gap between the cells and isolates the pn-junction. (b) shows the full area metallization step and (c) the contact separation.*

Figure 2.4a shows how the semi-finished cells with an interdigitated finger structure of emitter and base region are glued on a module glass. The glue also enters the gap between the cells and isolates the *pn*-junction. The cells have no metallization at this stage of the process sequence. The metallization and the interconnection of the cells are done in a single evaporation step as described in Figure 2.4b. The last step is the contact separation in an aluminum etch. Compared to a standard connection process, this technique avoids the printing of solderable pads and any other soldering steps which could decrease the yield. Compared to a two side contacted cell it additionally saves one complete metallization step. The BC BJ cell combines high cell efficiencies with an all in one metallization and cell interconnection step.

2.3.2 Cell processes

Supported cell process

We first describe BC BJ cells supported by a glass carrier. The supported cell process starts with a $30\,\mu$m thick $3 \times 10^{16}\,\mathrm{cm}^{-3}$ boron doped epitaxial layer still attached to the substrate wafer. The accessible (upper) side becomes the rear side of the cell. An interdigitated grid is formed on the accessible (upper) side of the cell after epitaxy of the absorber layer, as shown in Figure 2.5a. To this end a full area $100\,\Omega/\square$ emitter forms during phosphorous diffusion which is structured afterwards. Figure 2.5b demonstrates how a $\mathrm{Nd:YVO_4}$ laser with a wavelength of $\lambda = 355\,\mathrm{nm}$ and a pulse length of 8 to 9 ps ablates a $\mathrm{SiN_x}$ layer on top of the emitter in the area of the base region. A potassium hydroxide (KOH) solution etches the emitter and the laser damage within the opened base region. Afterwards we remove the $\mathrm{SiN_x}$ etching barrier in hydrofluoric acid (HF) and the cell is cleaned in a RCA cleaning step as demonstrated in Figure 2.5c.

Figure 2.5d shows the passivation of the whole surface with an a-Si/$\mathrm{SiN_x}$ double layer. The same laser as used for the base definition process locally removes this double layer in the center of the emitter and base finger to permit a silicon to metal contact [22].

An electron beam evaporation of an aluminum layer forms the contacts which are then covered by a silicon dioxide ($\mathrm{SiO_2}$) film, illustrated in Figure 2.5e. We realize the separation of the contacts by opening the $\mathrm{SiO_2}$ layer with a $\mathrm{Nd:YVO_4}$ laser with a wavelength of $\lambda = 355\,\mathrm{nm}$ and a pulse length of 20 ns followed by immersing the cell in a $\mathrm{H_2O/HNO_3/H_3PO_4/CH_3COOH}$ etching bath. The $\mathrm{SiO_2}$ film is an etching barrier for the etching solution, which finally separates the individual aluminum fingers.

Figure 2.5f shows the gluing of a glass substrate which supports the $30\,\mu$m thin and $79.2\,\mathrm{cm}^2$-large cell mechanically during lift-off. The high porosity layer serves as pre-defined breaking point allowing for the separation of the cell from the substrate. Afterwards we etch the remaining porous silicon on the substrate side of the cell (later the cell front side) in a KOH solution as shown in Figure 2.5g . This side of the cell is now accessible for a stack of a-Si passivation and a $\mathrm{SiN_x}$ antireflection coating after a RCA cleaning step. In order to contact the busbars, which are covered by the glass carrier on the rear side, we remove the silicon above the busbars by plasma etching [14]. By this, the busbars can be contacted from the front side of the solar cell. Note that this approach is only a laboratory remedy.

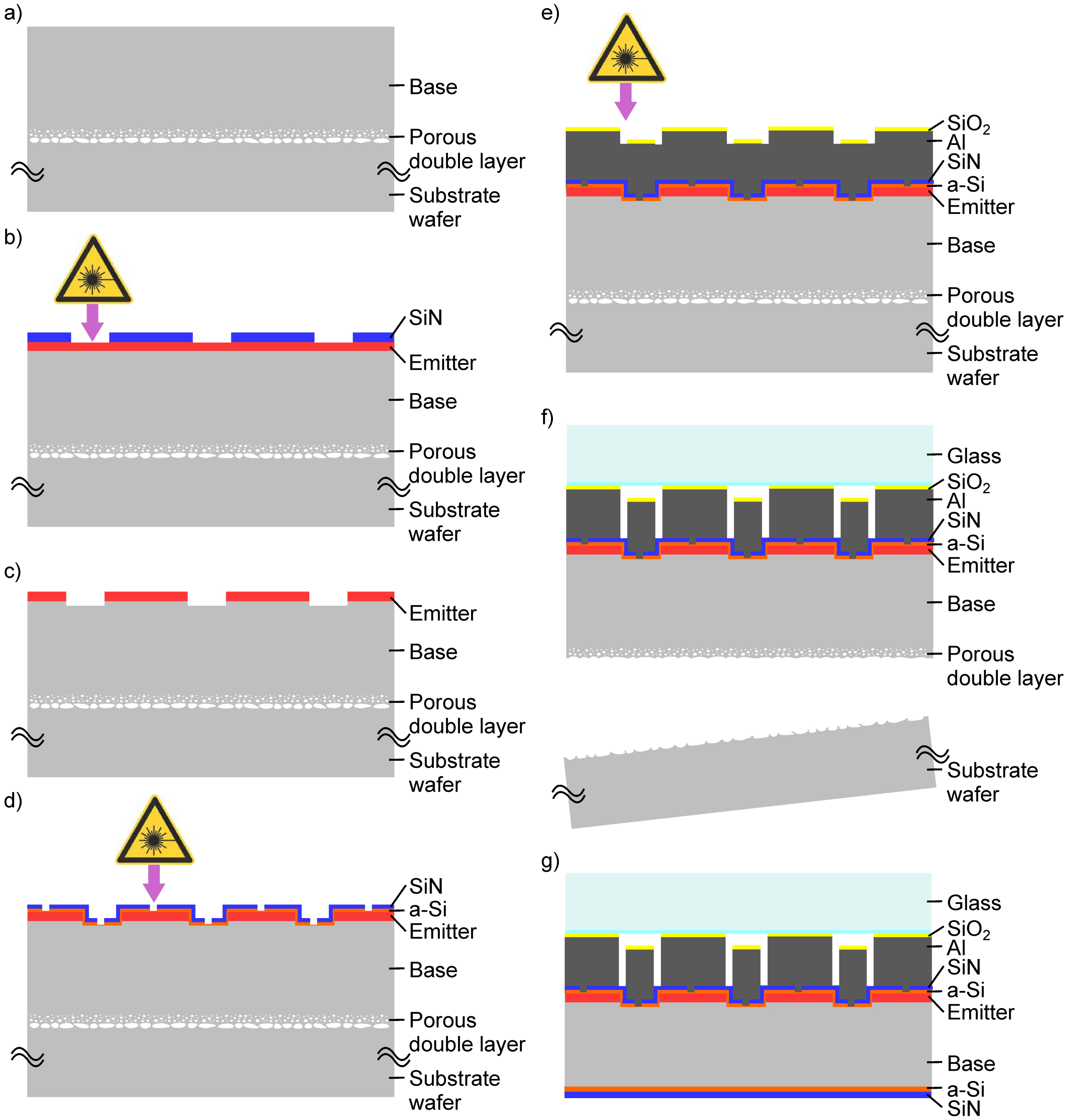

Figure 2.5: *Device fabrication of the supported large area back-contact back-junction PSI cell with a a-Si/SiN*$_\mathrm{x}$ *passivation.*

The best cell efficiency based on this concept is 13.5 %. We achieve a short-circuit current density of 28.7 mA cm^{-2} without applying a front texture. The open-circuit voltage is 633 mV and the fill factor is 74.0 %.

Free-standing cell process

The free-standing approach allows for higher degrees of freedom regarding both surface passivation and solar cell process sequence of the interdigitated BC BJ solar cell. Since the free-standing cell has a higher risk of breakage, the cell area is reduced to 3.96 cm^2. The free-standing cell process starts with a 3×10^{16} cm^{-3} boron doped epitaxial layer still attached to the substrate wafer. We start with an epitaxial layer thickness of 55 μm since it is reduced during a front surface texture later on. A boron diffusion forms a 25 $\Omega/\Box$ BSF, as shown in Figure 2.6a.

Figure 2.6b shows a 100 nm thick $\mathrm{SiN_x}$ layer which is deposited on top of the BSF and is ablated afterwards by a $\mathrm{Nd:YVO_4}$ laser with a wavelength of $\lambda = 532$ nm and a pulse length of 8 to 9 ps defining the area of the emitter region. The remaining $\mathrm{SiN_x}$ layer serves as etching barrier in the subsequent KOH etch which removes the laser damage and the BSF in the emitter region to a depth of 10 μm, as demonstrated in Figure 2.6c.

After the formation of a 70 $\Omega/\Box$ emitter in a phosphorous diffusion, we remove the $\mathrm{SiN_x}$ layer and the phosphorous glass in a HF etch and a thermal oxidation forms a 150 nm thick $\mathrm{SiO_2}$ passivation layer as shown in Figure 2.6d. The epitaxial layer is lifted off the substrate wafer by a vacuum chuck and is processed free-standingly from now on.

A wet chemical process in a KOH containing solution forms a textured front surface while the $\mathrm{SiO_2}$ layer protects the rear side, as demonstrated in Figure 2.6e. Figure 2.6f shows the laser ablation of the $\mathrm{SiO_2}$ layer for the contact openings on the emitter and base region by the same laser as previously used.

A stack of a 10 nm thick aluminum oxide ($\mathrm{AlO_x}$) layer for passivation and a $\mathrm{SiN_x}$ layer for antireflection coating is deposited on the front side of the cell as illustrated in Figure 2.6g.

Figure 2.6h shows the evaporation of a 10 μm thick aluminum layer and a 400 nm thick $\mathrm{SiO_2}$ layer on the rear side of the cell, which serves as an etching barrier against an etching solution containing $\mathrm{H_2O/HNO_3/H_3PO_4/CH_3COOH}$. This etch separates the contacts using a self aligned etching process [23] as shown in Figure 2.6i.

Our best cell efficiency using this concept is 18.8 % (18.9 % independently confirmed by Fraunhofer ISE CalLab; $J-V$ curves not available at date of submisson). We achieve a short-circuit current density of 35.7 mA cm^{-2} by applying a front texture. The open-circuit voltage is 654 mV and the fill factor is 80.4 %. This BC BJ PSI cell record energy conversion efficiency is the result of the analysis of all recombination parameters in combination with cell simulations and cell characterization methods. In the following Chapter 3 we present the current voltage analysis of different BC BJ PSI cells investigated in this work.

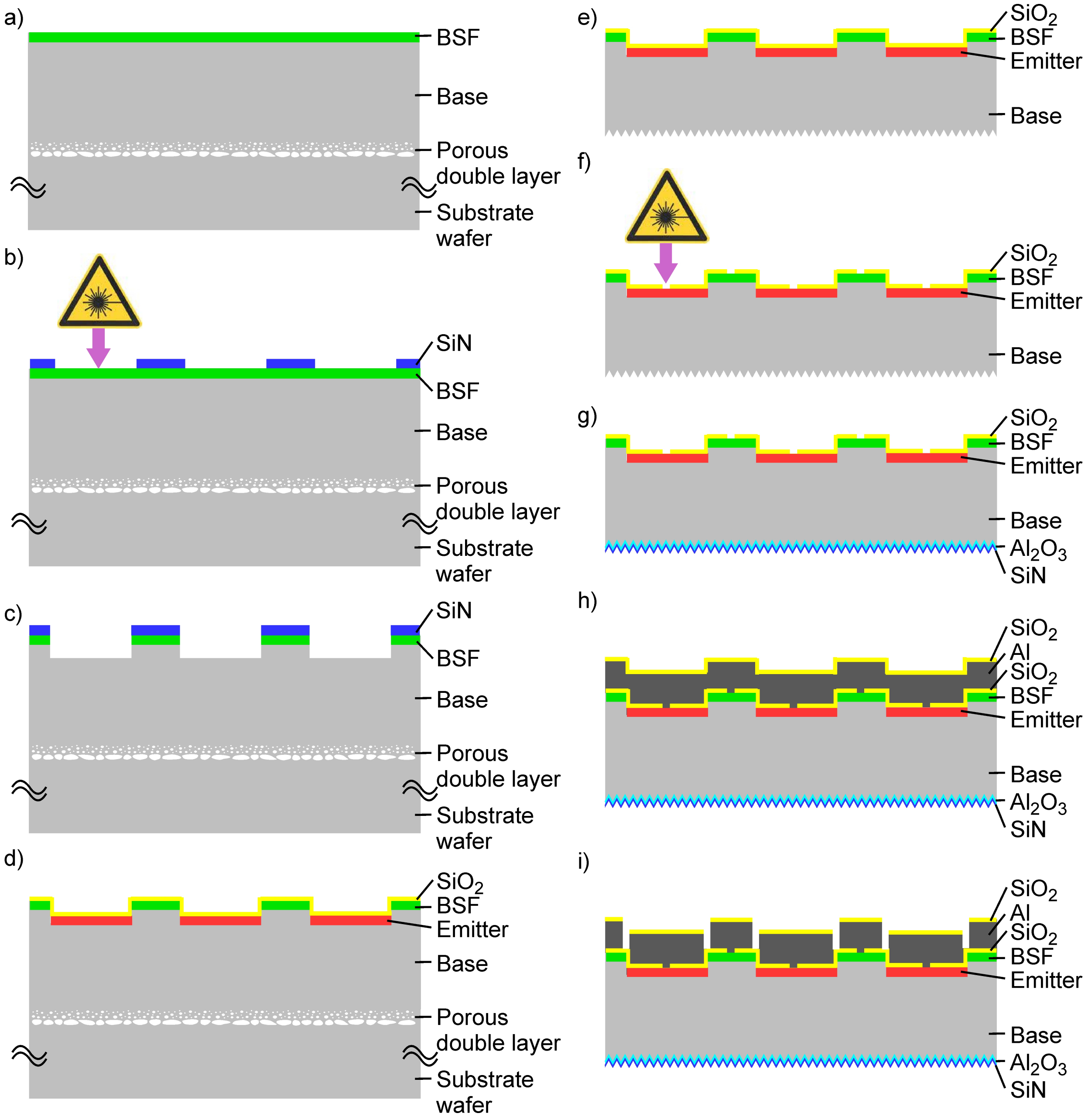

Figure 2.6: *Device fabrication of the free-standing back-contact back-junction PSI cell.*

3 Current-voltage characteristics and quantum efficiency

In Section 2.3 we demonstrate the process sequence of a supported and a free-standing BC BJ PSI cell. Aiming for an increase in the energy conversion efficiency it is essential to understand all generation and loss mechanisms in the cell. Therefore this work analyzes the generation and loss mechanisms in thin monocrystalline BC BJ PSI cells.

Figure 3.1 schematically shows a three-dimensional side/bottom view of our investigated cells. Six different groups of solar cells and corresponding test samples are analyzed in this work. The group names result from the main differences of the six groups which are shown in Table 3.1 on page 17. The groups have a 'High' or 'Low' base doping and 'Full' or 'Broken' line contacts, as shown in Figure 3.1. Group High-Full-Small has a 'Small' base finger width and group High-Full-BSF-Texture has a BSF and a textured front surface. The first five groups are supported by a glass carrier, whereas group High-Full-BSF-Texture is processed free-standing. The five supported groups differ in base doping, contact layout and emitter fraction.

We investigate the impact of the different base doping concentrations on the open-circuit voltage and the internal series resistances by the comparison of groups with 'High' and 'Low' base doping. We analyze the impact of the different contact layouts 'Full' and 'Broken' line in combination with the different doping concentrations 'High' and 'Low' on the series resistances in the solar cell. The contact geometries are schematically shown in Figure 3.1 whereas a detailed view is shown in Section 6.3 in Figure 6.7 on page 70. 'Broken' compared to 'Full' line contacts increase the distance which the majority carriers have to diffuse to reach the base contact. This increased distance in combination with an increased resistance in the base by changing from 'High' to 'Low' doping concentration increases the resistance. Due to low diffusion lengths in the epitaxial layers only a part of the minority carriers which are generated in the base region reach the emitter. To analyze this effect we change the base finger width. Emitter and base fingers have the same width in group High-Full-Small and thus an emitter fraction of 0.5 whereas the other groups have wider emitter fingers and thus an emitter fraction of 0.8. All of the supported groups have no textured front surface and no back surface field (BSF). The free-standing approach has a high base doping, full line contacts, a textured front surface and a BSF combining low series resistances with high generation and low recombination. In the following we characterize the cells in detail.

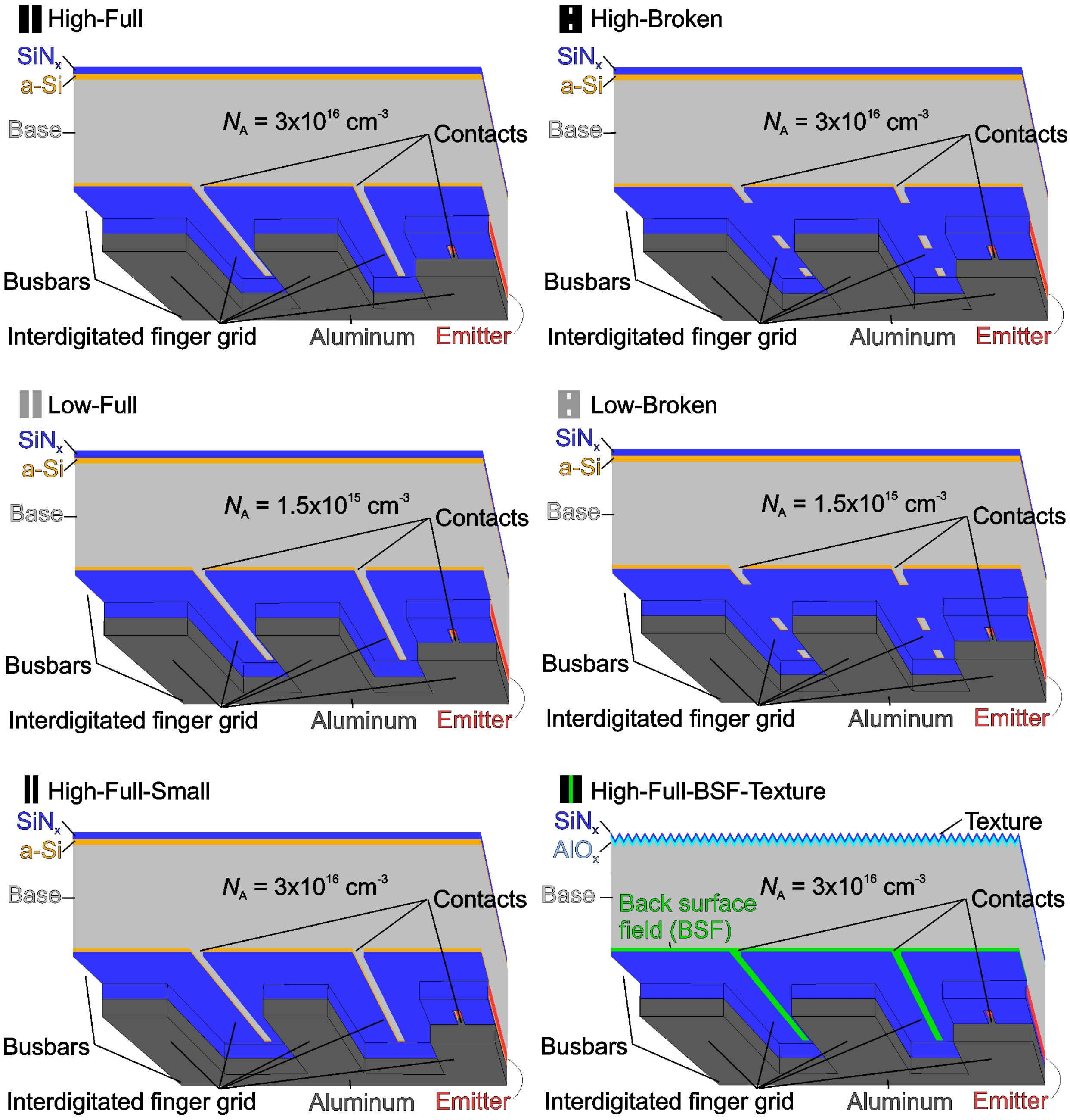

High-Full

High-Broken

Low-Full

Low-Broken

High-Full-Small

High-Full-BSF-Texture

Figure 3.1: *Schematic three-dimensional side/bottom view of our six investigated cell groups. The metallization on the base region is not shown in this case for visualization of the contact layout.*

Table 3.1: *Main differences of the six cell groups characterized in this work. The groups have a 'High' or 'Low' base doping and 'Full' or 'Broken' line contacts. Group High-Full-Small has a 'Small' base finger width and group High-Full-BSF-Texture has a BSF and a textured front surface.*

	High-Full (■)	High-Broken (■)	Low-Full (▨)	Low-Broken (▨)	High-Full-Small (■)	High-Full-BSF-Texture (🟩)
Doping density [$\mathrm{cm^{-3}}$]	3×10^{16}	3×10^{16}	1.5×10^{15}	1.5×10^{15}	3×10^{16}	3×10^{16}
Contact layout	Full line	Broken line	Full line	Broken line	Full line	Full line
Supported	Yes	Yes	Yes	Yes	Yes	No
Emitter fraction	0.8	0.8	0.8	0.8	0.5	0.84
BSF and Texture	No	No	No	No	No	Yes
Measured J-V parameters of the six cell groups investigated						
J_{SC} [$\mathrm{mA\,cm^{-2}}$]	28.7	28.6	29.0	29.4	18.8	35.7
V_{OC} [mV]	633	644	557	566	621	654
FF [%]	74.0	67.2	67.3	45.9	67.7	80.4
η [%]	13.5	12.4	10.8	7.6	7.9	18.8
pFF [%]	79.5	74.9	76.6	78.5	72.3	82.9
$p\eta$ [%]	14.5	13.8	12.3	13.0	8.4	19.4
Parameters of the two-diode model for the six cell groups investigated						
J_{SC} [$\mathrm{mA\,cm^{-2}}$]	28.7	28.6	29.0	29.5	18.8	35.7
V_{OC} [mV]	630	644	555	567	609	655
FF [%]	76.0	74.0	72.1	64.4	70.3	80.5
η [%]	13.7	13.7	11.6	10.8	8.1	18.8
$J_{0,1}$ [$\mathrm{fA\,cm^{-2}}$]	530	280	8300	5400	300	270
$J_{0,2}$ [$\mathrm{nA\,cm^{-2}}$]	25	25	190	140	90	10
R_{S} [$\Omega\,\mathrm{cm^2}$]	1.2	1.7	1.2	3.2	1.5	0.4
R_{Shunt} [$\mathrm{k\Omega\,cm^2}$]	10	68	78	20	5	17

3.1 Current-voltage characteristics

3.1.1 Theory of current-voltage curves and two diode model

Our starting point after solar cell production is to determine the power output by measuring the current-voltage characteristics. The first conclusions about the generation and loss mechanisms can be made based on these measurements. Three types of J-V measurements are investigated in this work: the light J-V measurement, the dark J-V measurement and the J_{SC}-V_{OC} measurement. Figure 3.2a exemplarily shows the results of the J-V measurements of the group High-Full-BSF-Texture.

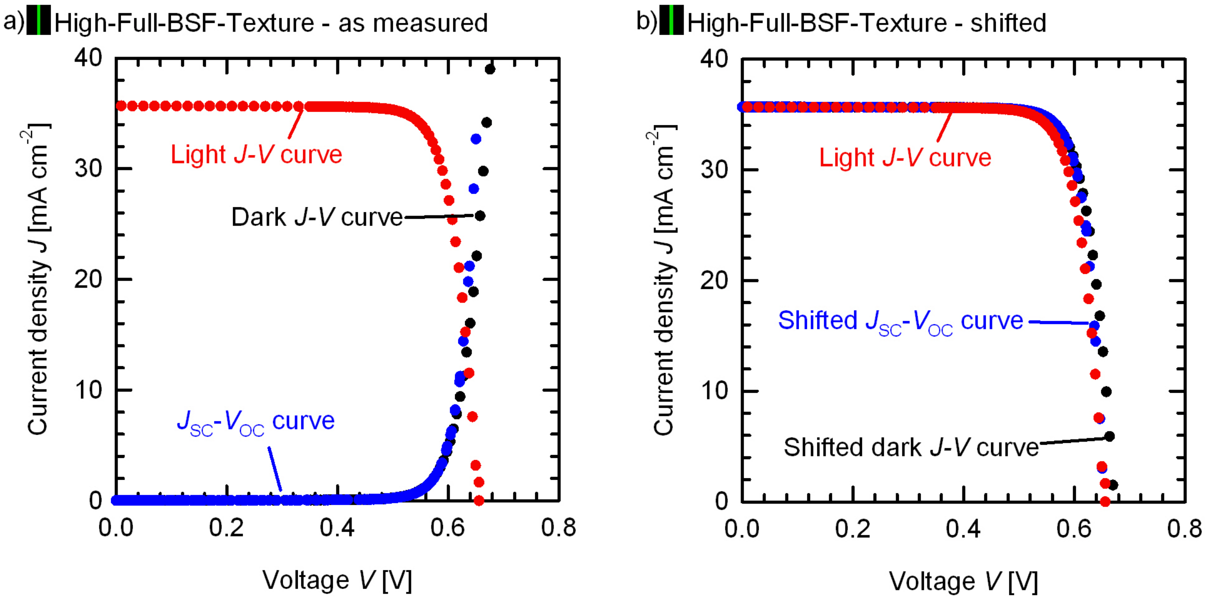

Figure 3.2: *Exemplary J-V measurement results of group High-Full-BSF-Texture. a) shows the directly measured curves. b) shows the shifted curves.*

A class CAA sun simulator (C class spectrum, A class irradiance ±2 % uniformity and A class irradiance and temperature corrections according to IEC 60891) measures the light J-V characteristics at 25 °C. While at short-circuit conditions the terminal voltage is zero and the current density is $J = J_{\mathrm{SC}}$, at open-circuit conditions the terminal current is zero and the voltage is $V = V_{\mathrm{OC}}$. The maximum power point is the maximum of the product of voltage and current density. The voltage at this point is V_{MPP}, whereas the current density at this point is J_{MPP}. The fill factor (FF) is defined by

$$FF = \frac{V_{\mathrm{MPP}} \times J_{\mathrm{MPP}}}{V_{\mathrm{OC}} \times J_{\mathrm{SC}}}. \tag{3.1}$$

The most important characteristics of the solar cell is the efficiency defined as

$$\eta = \frac{V_{\mathrm{MPP}} \times J_{\mathrm{MPP}}}{I}, \tag{3.2}$$

where I is the wavelength integrated power density of the light which illuminates the solar cell.

During the measurement of the dark J-V curve the solar cell is kept in the dark and held at 25 °C. Figure 3.2b shows the shifted dark J-V curve. The current density of this curve is defined as

$$J_{\text{dark}-\text{shifted}} = J_{\text{SC}} - J_{\text{dark}}. \tag{3.3}$$

Comparing the shifted dark J-V curve with the light J-V curve one finds that the current density is higher for the dark J-V curve in the complete voltage range.

During the J_{SC}-V_{OC} measurement the temperature is again kept at 25 °C. Pairs of short-circuit current density and the open-circuit voltage are measured while the light intensity decreases. Figure 3.2b shows the shifted dark J_{SC}-V_{OC} curve. The current density of this curve is defined as

$$J_{J_{\text{SC}}-V_{\text{OC}-\text{shifted}}} = J_{\text{SC}} - J_{J_{\text{SC}}-V_{\text{OC}}}. \tag{3.4}$$

The shifted J_{SC}-V_{OC} curve shows an intersection with the light J-V curve at the open-circuit voltage. At this point the the J_{SC}-V_{OC} curve was measured at the same illumination intensity as the light J-V curve. The J_{SC}-V_{OC} measurement is free of series resistance since no current flows at open-circuit conditions and therefore the voltage drop is zero and the short-circuit current is also not influenced by the series resistance. The difference between the shifted J_{SC}-V_{OC} curve and the light J-V curve shows the impact of the series resistance on the light J-V curve. A pseudo-fill factor (pFF) is defined for the shifted J_{SC}-V_{OC} curve in analogy to the light J-V curve as following:

$$pFF = \frac{\max\left(J_{J_{\text{SC}}-V_{\text{OC}-\text{shifted}}} \times V_{J_{\text{SC}}-V_{\text{OC}-\text{shifted}}}\right)}{V_{\text{OC}} \times J_{\text{SC}}}. \tag{3.5}$$

The pseudo efficiency ($p\eta$) is the power output fraction of the cell, if the series resistance was zero. It is calculated according to:

$$p\eta = \frac{pFF}{FF} \times \eta = \frac{\max\left(J_{J_{\text{SC}}-V_{\text{OC}-\text{shifted}}} \times V_{J_{\text{SC}}-V_{\text{OC}-\text{shifted}}}\right)}{I}. \tag{3.6}$$

The diode saturation current density is a measure of the recombination in a solar cell. As will be shown in Section 4.1.1 and 4.1.2, various recombination paths contribute to the total recombination. Therefore the total recombination in the cell $J_{\text{rec}}(V)$ in dependence of the terminal voltage V can be written as:

$$J_{\text{rec}}(V) = \sum_i J_{0,i}\left[\exp\left(\frac{qV}{kTn_{\text{ideality},i}}\right) - 1\right], \tag{3.7}$$

where kT/q is the thermal voltage. Each recombination path i is characterized by a saturation current density $J_{0,i}$ and its ideality factor $n_{\text{ideality},i}$. Ideal recombination where $U \propto \Delta n^2$ has an ideality factor of $n_{\text{ideality}} = 1$. Surface and bulk recombination have an ideality factor close to 1. Other recombination mechanisms measured on the cells investigated in this work have ideality factors exceeding 6. The higher each $J_{0,i}$ the higher the total recombination in the cell. Equation 3.7 represents the current-voltage characteristics of the solar cell in the non-illuminated case. Under illumination the superposition principle allows to shift the characteristics by the generated current density J_{L} and multiply it with -1 to stay in the first quadrant. This results in the current-voltage characteristics in the illuminated case:

$$J\left(V\right) = J_{\mathrm{L}} - \sum_{i} J_{0,i}\left[\exp\left(\frac{qV}{kTn_{\mathrm{ideality},i}}\right) - 1\right] = J_{\mathrm{L}} - J_{\mathrm{rec}}, \tag{3.8}$$

where $J\left(V\right)$ is the current of the solar cell in dependence of the terminal voltage V. If every $n_{\mathrm{ideality},i} = 1$, Equation 3.7 simplifies to

$$J_{\mathrm{rec}}\left(V\right) = J_0\left[\exp\left(\frac{qV}{kT}\right) - 1\right] = J_0\frac{pn - n_{\mathrm{i}}^2}{n_{\mathrm{i}}^2}. \tag{3.9}$$

In an open circuit no current flows and the open-circuit voltage can be written by:

$$V_{\mathrm{oc}} = \frac{kT}{q}\ln\left(\frac{J_{\mathrm{L}}}{J_0} + 1\right). \tag{3.10}$$

The *J*-*V* curves of many solar cells can be modeled by Equation 3.8 with the inclusion of a shunt resistance and a lumped series resistance:

$$J\left(V\right) = J_{\mathrm{L}} - \sum_{i} J_{0,i}\left[\exp\left(\frac{q(V + R_{\mathrm{s}} \times J)}{kTn_{\mathrm{ideality},i}}\right) - 1\right] - \frac{V + R_{\mathrm{s}} \times J}{R_{\mathrm{Sh}}}, \tag{3.11}$$

where R_{Sh} is the shunt resistance and R_{s} is the lumped series resistance. The conversion efficiency is maximized by minimizing saturation current densities $J_{0,i}$, ideality factors $n_{\mathrm{ideality},i}$ and lumped series resistance R_{s} and by maximizing the shunt resistance R_{sh}. However, the correlation between the recombination in each part of the cell and the fitted single saturation current density $J_{0,i}$ in the model is not obvious. Often two diode saturation current densities are used in combination with the ideality factors 1 and 2 [24]. The saturation current density belonging to the ideality factor 2 describes the recombination in the space charge region, whereas the saturation current density belonging to the ideality factor 1 describes the recombination in the bulk, in the emitter and at the surface. This two-diode model is also applied to the *J*-*V* curves of the six cell groups investigated in this work. We first fit the two saturation current densities to the J_{SC}-V_{OC} curve. Keeping the saturation current densities constant, the shunt and lumped series resistance are fitted to model the dark *J*-*V* curve. Finally, we use the light *J*-*V* curve to fit the generated current density J_{L}.

3.1.2 Results of current-voltage analysis

Figure 3.3 shows the measured light *J*-*V*, dark *J*-*V* and J_{SC}-V_{OC} curves of the six groups investigated in this work. The figure also shows the modeled *J*-*V* curves of the two-diode model. The associated parameters of the two-diode model of the *J*-*V* curves are shown in Table 3.1 on page 17.

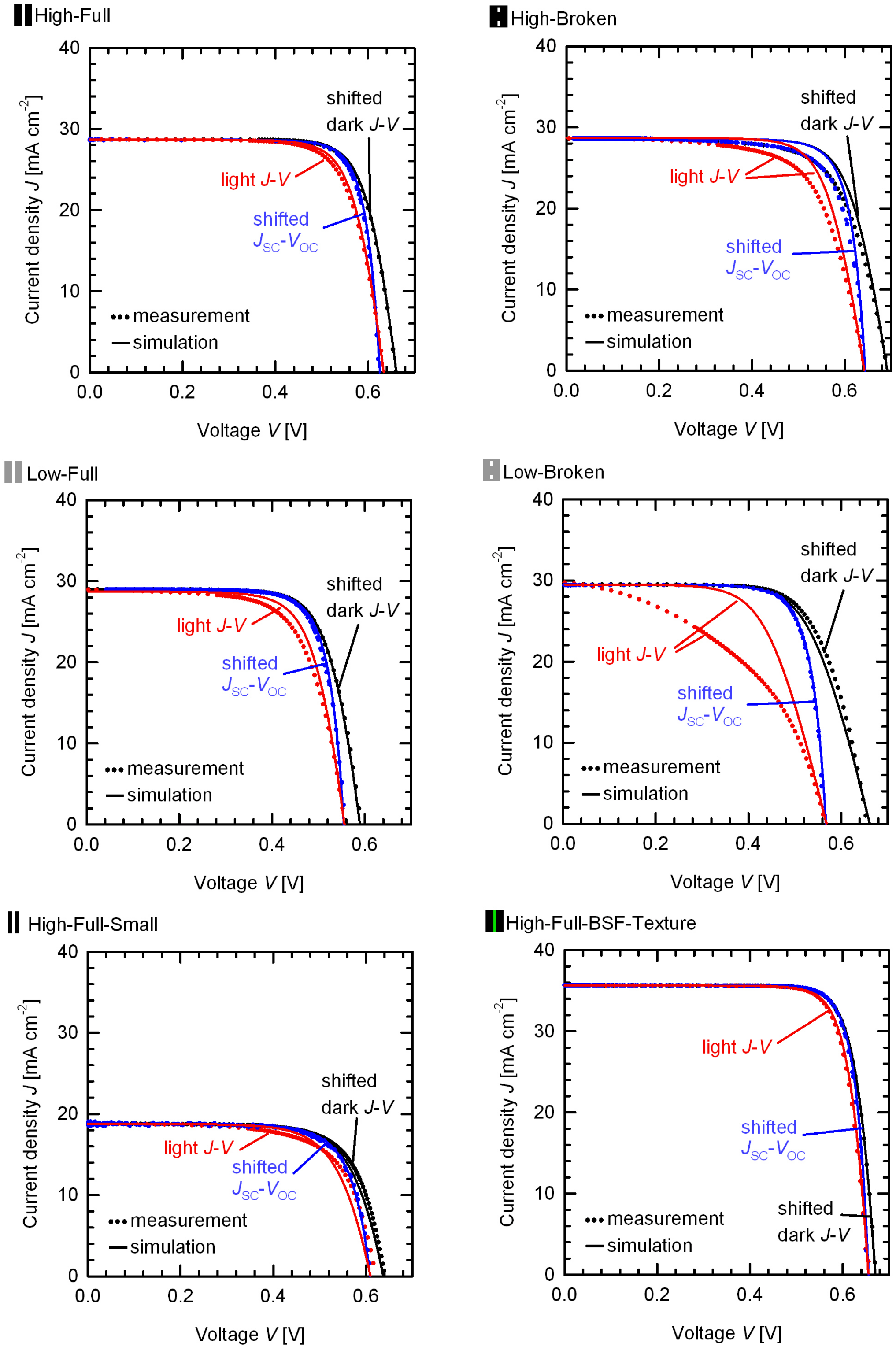

Figure 3.3: *Measured (dots) light J-V curves (red), dark J-V curves (black) and* J_{SC}-V_{OC} *curves (blue) of the six groups investigated. The resulting J-V curves of the two-diode model are also shown in this graph (lines).*

In all groups except in group High-Broken (▮) the differences between modeled and measured J_{SC}-V_{OC} curves as well as the dark J-V curves are negligible. All light J-V curves derived by using the two-diode model show a discrepancy to the measured light J-V curves except in group High-Full-BSF-Texture (▮). The discrepancy is the highest for groups Broken. This fact will be discussed in this section and in more detail by using the simulation results of network loss analysis in Section 6.3 on page 69 and by using photoluminescence in Section 7.2 on page 83.

Short-circuit current density

Table 3.1 shows that the first four groups with a planar front surface show short-circuit current densities from $J_{\mathrm{SC}} = 28.6\,\mathrm{mA\,cm^{-2}}$ to $J_{\mathrm{SC}} = 29.4\,\mathrm{mA\,cm^{-2}}$. Group High-Full-Small (▮) features a short-circuit current density of only $J_{\mathrm{SC}} = 18.8\,\mathrm{mA\,cm^{-2}}$. This fact is due to the low emitter fraction of 0.5 compared to the other groups. This effect is known as electrical shading [20] and is investigated by electroluminescence in Section 7.1 on page 77. The free-standing group High-Full-BSF-Texture (▮) has a texture on the front surface, which increases the short-circuit current density to $J_{\mathrm{SC}} = 35.7\,\mathrm{mA\,cm^{-2}}$.

Fill factor

The differences between the FFs and the pFFs shown in Table 3.1 on page 17 are due to different series resistances in the solar cell. The resistive losses are the highest for group Low-Broken (▮) and the lowest for group High-Full-BSF-Texture (▮). The resistive losses increase with decreasing doping density at the silicon to metal interface (which is the case for changing the groups from High-Full-BSF-Texture (▮) to High to Low) as well as with decreasing contact area (which is the case for changing the groups from Full to Broken). By decreasing the doping density of the silicon at the metal to silicon interface, the base contact resistance increases. By decreasing the contact area, the base resistance for the majority carriers increases due to an increased distance in the base from the location of carrier generation to the broken line contacts. These resistance losses are discussed in more detail in Section 6.3 on page 69. In addition electroluminescence (Section 7.1 on page 77) and photoluminescence (Section 7.2 on page 83) measurements are used to investigate the effect of the lateral series resistances in the base.

Open-circuit voltage

Table 3.1 on page 17 also shows that all groups have different open-circuit voltages. The open-circuit voltage depends on the short-circuit current density and the saturation current densities as shown in Equation 3.11. Groups Low show one order of magnitude higher $J_{0,2}$ values than the rest of the groups and even two orders of magnitude higher than group High-Full-BSF-Texture (▮). This saturation current density can be interpreted as the recombination current density in the space charge region. Since the base doping in groups Low is 20 times lower than in groups High, the junction differs significantly, which in turn results in a different recombination in the space charge region. The $J_{0,2}$ values in the groups with the same base doping do not differ significantly, with the exception of group High-Full-BSF-Texture (▮), which has a one to two orders of magnitude lower $J_{0,2}$ value due to a deeper emitter with a lower surface doping concentration compared to the other groups with the same base doping.

$J_{0,1}$ is mainly influenced by the recombination at the surface and in the base. The five supported groups differ in bulk quality as well as in surface quality. The $J_{0,1}$ value increases with increasing contact area (which is the case for changing the groups from Broken to Full) as well as with decreasing bulk lifetime, as shown in Table 7.1 on page 84 (which is the case for changing the groups from High-Full-BSF-Texture (▮) to others to High-Full-Small (‖)), decreasing emitter fraction (which is the case for changing the groups from High-Full-BSF-Texture (▮) to others to High-Full-Small (‖)) and decreasing doping concentration (which is the case for changing the groups from High to Low). The recombination at the surface increases with increasing contact area since the recombination at the contacts is much higher than at the passivated surface. The recombination at the surface also increases with increasing emitter fraction, since the recombination there is higher than in the passivated base region. Group High-Full-BSF-Texture (▮) has the lowest $J_{0,1}$ value due to a back surface field at the base contacts which reduces the recombination at this point. The recombination losses will be discussed in more detail in Section 6.2 on page 60.

Shunt resistance

Table 3.1 on page 17 also shows the shunt and series resistances of the six groups. The shunt resistances of all groups are higher than $4\,\mathrm{k\Omega\,cm^2}$, which means that only a negligible part of the current is bypassed in parallel to the junction. This shunt resistance induces less than 0.1 % absolute efficiency loss in all groups of solar cells. This loss is determined by the difference of the fitted shunt resistance to an infinite shunt resistance.

Series resistance

First the series resistance of group High-Full (▮) is investigated. Here the discrepancy of measured and fitted light J-V curves is small and the difference between the pFF and the FF is 2 % absolute. As already identified by the pFF the series resistance increases with decreasing doping density at the metal to silicon interface (which is the case for changing the groups from High to Low) due to the higher contact resistance. Groups Broken show a high discrepancy of the light J-V curves obtained from fitting the two-diode model and the measured light J-V curves. This discrepancy is also reflected by the differences between the measured and fitted fill factors, which are 2.8 % and 18.5 % absolute respectively. In the two-diode model the series resistance is a lumped series resistance which cannot explain the resistance losses in these groups. For further characterization of the series resistance losses, electroluminescence measurements in Section 7.1 on page 77 and photoluminescence measurements in Section 7.2 on page 83 are carried out in order to gain information of the lateral distribution of the resistances. PL-Rs [7] measurements are performed to determine absolute series resistance loss values. The impact of the series resistances to the light and dark J-V curves is also described by simulations in Section 6.3 on page 69.

Influence of non ideal recombination

To quantify the power loss by non ideal recombination we set the diode saturation current density with the ideality factor of 2 in the two diode model to 0. Table 3.2 shows the efficiency of all groups with this manipulated model without the influence of non ideal recombination.

The open-circuit voltage, fill factor, and efficiency increases after setting $J_{0,2} = 0$. The increase is the highest for group High-Full-Small (▮▮) due to a high quotient of $J_{0,2}/J_{0,1}$. The open-circuit voltage increases from 609 mV to 639 mV, the fill factor from 70.3 % to 79.1 % and the efficiency from 8.1 % to 9.5 %. Group High-Full-BSF-Texture (▮▮) shows the lowest increase in the parameters due to the relative low quotient of $J_{0,2}/J_{0,1}$. In conclusion, non ideal recombination is a limiting factor in all groups. Even in the optimized cell design the non ideal recombination causes an absolute efficiency drop of 0.4 %.

3.2 Quantum efficiency

3.2.1 Theory of quantum efficiency measurements

Quantum efficiency (QE) measurements determine the efficiency of the cell in dependence of the wavelength of the incident light. The external quantum efficiency (EQE) measures the ratio of the number of electrons which are collected under short-circuit conditions ($N_\mathrm{t}(\lambda)$) and the total number of photons which hit the front surface of the cell at one specific wavelength λ ($N_\mathrm{t,front}(\lambda)$):

$$\mathrm{EQE}(\lambda) = \frac{N_\mathrm{t}(\lambda)}{N_\mathrm{t,front}(\lambda)}. \tag{3.12}$$

The internal quantum efficiency (IQE) is calculated from the ratio of the number of electrons which are collected at the contacts under short-circuit conditions and the number of photons which are absorbed in the cell at one specific wavelength λ ($N_\mathrm{t,absorbed}(\lambda)$):

$$\mathrm{IQE}(\lambda) = \frac{N_\mathrm{t}(\lambda)}{N_\mathrm{t,absorbed}(\lambda)} = \frac{J_\mathrm{SC}(\lambda)}{J_\mathrm{SC,absorbed}(\lambda)} = \frac{\mathrm{EQE}(\lambda)}{1 - R(\lambda)}, \tag{3.13}$$

where $J_\mathrm{SC}(\lambda)$ is the short circuit current density, $J_\mathrm{SC,absorbed}(\lambda)$ is the equivalent photo-generated current density at λ. $R(\lambda)$ is the wavelength-dependent reflection and thus $N_\mathrm{t,absorbed}(\lambda) = (1 - R(\lambda)) \times N_\mathrm{t,front}(\lambda)$.

3.2.2 Results of quantum efficiency measurements

Figure 3.4 shows the reflection as well as the external and internal quantum efficiency of the cells of the six groups investigated in this work. The optical properties of the first five groups differ from those of the last group in many ways, therefore they are analyzed separately. The first five groups all have a planar front surface and an a-Si/SiN$_\mathrm{x}$ passivation and antireflection coating on front and rear surface. The reflection is zero at a wavelength of 550 to 600 nm due to the thickness of the antireflection coating in combination with its refractive index, but it increases at increasing wavelengths due to the planar front surface. At wavelengths above 850 nm the reflection is mainly influenced by the reflection of the rear

Table 3.2: *Parameters of the current-voltage curves of the fitted two diode models with and without the influence of non ideal recombination.*

	High-Full (■)		High-Broken (▣)		Low-Full (▨)		Low-Broken (▩)		High-Full-Small (▮)		High-Full-BSF-Texture (🟩)	
	non-i.	ideal	non-i.	ideal	non-i.	ideal	non-i.	ideal	non-i.	ideal	non-i.	ideal
J_{SC} [mA cm^{-2}]	28.7	28.7	28.6	28.6	29.0	29.0	29.5	29.5	18.8	18.8	35.7	35.7
V_{OC} [mV]	630	635	644	651	555	565	567	576	609	639	655	658
FF [%]	76.0	78.5	74.0	77.0	72.1	76.5	64.4	67.8	70.3	79.1	80.5	81.9
η [%]	13.7	14.3	13.7	14.3	11.6	12.5	10.8	11.5	8.1	9.5	18.8	19.2
$J_{0,1}$ [fA cm^{-2}]	530	530	280	280	8300	8300	5400	5400	300	300	270	270
$J_{0,2}$ [nA cm^{-2}]	25	0	25	0	190	0	140	0	90	0	10	0
R_{S} [Ω cm^2]	1.2	1.2	1.7	1.7	1.2	1.2	3.2	3.2	1.5	1.5	0.4	0.4
R_{Shunt} [kΩ cm^2]	10	10	68	68	78	78	20	20	5	5	17	17

side of the solar cell. It increases up to about 0.8 at a wavelength of about 1100 nm. This is due to the rear mirror consisting of a SiN_x/Al stack. The reflection only increases by about 0.05 from 1100 nm to 1200 nm.

The EQE and the IQE of the first four groups are similar whereas the EQE and the IQE of group High-Full-Small (▮▮) is different. The EQE of the first four groups is only about 0.2 at a wavelength of 300 nm and increases to about 0.9 at a wavelength of 600 nm. In this wavelength range the photons are lost due to reflection and the absorption in the a-Si front side passivation layer which will be investigated by simulations in Section 6.1 on page 57. The EQE at wavelengths of more than 600 nm decreases again due to reflection and absorption in the aluminum rear side layer. This will be discussed in more detail during the optical loss analysis in Section 6.1 on page 57. The EQE and IQE finally drop to 0 at a wavelength of 1200 nm due to the bandgap of silicon. At all wavelengths some of the generated electrons also recombine before they reach the contacts. This is the reason why the IQE is less than 1 at all wavelengths. The IQE shows a similar behavior as the EQE. It is calculated by Equation 3.13 using the measured EQE and reflection R. It does not take into account the absorption in the dielectric layers covering the base of the cell since this absorption cannot be measured directly. By considering this absorption the IQE would be much higher especially at low wavelength where the front a-Si absorbs a lot as will be shown in Section 6.1 on page 57.

The EQE as well as the IQE of group High-Full-Small (▮▮) is much lower at all wavelengths compared to the first four groups. The maximum IQE in this group is only 0.6 which is about 2/3 of the first four groups. This is caused by the small diffusion length of the electrons compared to the large width of the base fingers, which results in so-called electrical shading. This will be discussed in detail with the help of the results of the unit cell simulations in Section 6.2 on page 60 and in Section 7.1 on page 77.

Due to the textured front surface in group High-Full-BSF-Texture (█) the reflection is much lower at all wavelengths compared to the other groups. In the range of 400 to 900 nm the reflection is only 6 %. The reflection in the range from 1100 nm to 1200 nm is about 0.2 points lower in this group since the rear reflector is not as well designed as in the other groups due to a different layer stack at the rear side, which results in a lower absorption in the base at these wavelengths.

The EQE as well as the IQE is much higher at wavelengths from 300 to 600 nm in group High-Full-BSF-Texture (█) compared to the other five groups. This is due to the improved front side passivation layer (AlO_x) which is used in the free-standing process since there is no temperature limitation for the passivation step. The AlO_x is much less absorbing than the a-Si layer which passivates the other groups. In the wavelength range from 400 to 800 nm the EQE as well as the IQE are nearly constant at about 0.86. The losses in this region are due to recombination in the cell. The EQE and IQE finally drop to 0 at a wavelength of 1200 nm due to the bandgap of silicon.

In summary we analyze the optical losses qualitatively by quantum efficiency measurements. A quantitative analysis will follow in Sections 6.1 on page 57 and 6.2.3 on page 63. The low QE at short wavelengths of the first five groups is due to the strongly absorbing

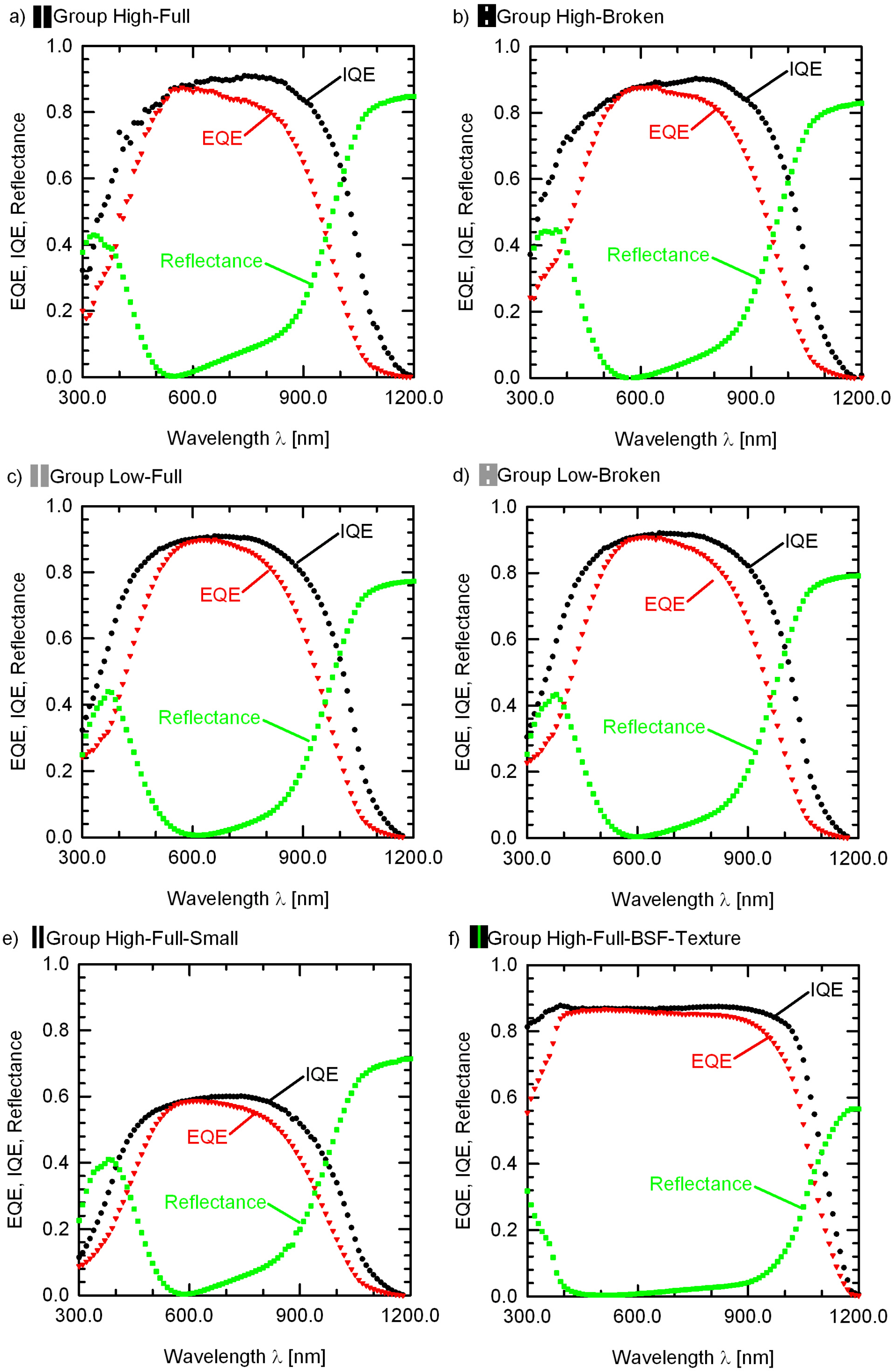

Figure 3.4: *Measured reflection (green), external (red) and internal (black) quantum efficiencies of the six groups investigated in this work.*

a-Si layer which will be confirmed by simulations in Section 6.1 on page 57 and the low IQE of group High-Full-Small (▮▮) is due to the low diffusion length of the minority carriers in combination with the large width of the base fingers. The improvements made in group High-Full-BSF-Texture (█) are also clearly visible in the QE measurements. Further quantitative analysis requires the comparison to quantum efficiencies resulting from finite element simulations. This will be shown in Section 6.4.

4 Determination of saturation current densities and bulk lifetime

4.1 Theory of recombination of charge carriers

This chapter describes the relevant recombination mechanisms in the PSI BC BJ solar cell. The knowledge of these recombination mechanisms is necessary for the determination of saturation current densities of the solar cell. The saturation current densities are measured with appropriate measurement techniques and are input parameters for solar cell device simulations. From these simulations the power density losses of each part of the cell are calculated.

The generated electron-hole pairs recombine in the silicon bulk and at the interfaces to the dielectrics and the metal contacts. Therefore we differentiate between bulk recombination and surface recombination. For a high conversion efficiency all recombination paths should be kept as small as possible in the solar cell. Therefore it is essential to understand the recombination mechanisms in detail.

For the description of the recombination paths the correlations between electron and hole concentrations have to be known. In a non illuminated silicon wafer in thermal equilibrium the concentration of electrons is $n = n_0$ and the concentration of holes is $p = p_0$. The balance of generation and recombination is described by the law of mass action $n_0\, p_0 = n_{\mathrm{i,eff}}^2$, where $n_{\mathrm{i,eff}} = 9.65 \times 10^9\,\mathrm{cm}^{-3} \times \exp\left(\Delta E_{\mathrm{gap}}/kT\right)$ is the effective intrinsic carrier concentration, ΔE_{gap} is the doping dependent bandgap narrowing and kT is the thermal energy [25]. At standard conditions of $25\,^{\circ}\mathrm{C}$ and a doping concentration of $N_{\mathrm{A}} = 3 \times 10^{16}\,\mathrm{cm}^{-3}$, which is mostly used in the investigations of cells and other samples in this work, the effective intrinsic carrier concentration is $n_{\mathrm{i,eff}} = 1.03 \times 10^{10}\,\mathrm{cm}^{-3}$. Assuming complete ionization of the doping atoms, which is a good approximation for standard conditions, the following relations are valid:

$$\begin{aligned} n_0 = N_{\mathrm{D}}, \quad p_0 = \tfrac{n_{\mathrm{i,eff}}^2}{N_{\mathrm{D}}} \quad & \text{for } n\text{-type silicon} \\ p_0 = N_{\mathrm{A}}, \quad n_0 = \tfrac{n_{\mathrm{i,eff}}^2}{N_{\mathrm{A}}} \quad & \text{for } p\text{-type silicon.} \end{aligned} \tag{4.1}$$

Under illumination excess carriers $\Delta n = \Delta p$ are generated. The concentration of electrons becomes $n = n_0 + \Delta n$ and the concentration of holes $p = p_0 + \Delta p$. After the illumination is turned off, the excess carriers recombine with the net recombination rate

$$U\left(\Delta n(t), n_0, p_0\right) = \frac{\partial \Delta n}{\partial t}. \tag{4.2}$$

The concentration of excess electrons and holes is proportional to the recombination rate ($\Delta n \propto U$), since the recombination probability of a carrier is independent of the total carrier concentration. Therefore Δn decreases exponentially, $\Delta n(t) = \Delta n(0) \times \exp(-\frac{t}{\tau})$, where τ is the carrier lifetime. Different independent recombination paths are described by different lifetimes τ_i. The total excess carrier concentration is

$$\begin{aligned}\Delta n(t) &= \Delta n(0) \times \exp\left(-\frac{t}{\tau_1}\right) \times \exp\left(-\frac{t}{\tau_2}\right) \times \exp\left(-\frac{t}{\tau_3}\right) ... \\ &= \Delta n(0) \times \exp\left(-\left(\frac{t}{\tau_1} + \frac{t}{\tau_2} + \frac{t}{\tau_3} + ...\right)\right) = \Delta n(0) \times \exp\left(-\frac{t}{\tau_{\text{eff}}}\right) \qquad (4.3)\end{aligned}$$

where τ_{eff} is the effective lifetime. In the following we discuss the different recombination mechanisms.

4.1.1 Bulk recombination

Bulk recombination is divided into intrinsic and extrinsic recombination. Intrinsic recombination consists of radiative band-to-band recombination and non radiative Auger recombination. Extrinsic recombination is recombination via defect levels in the bandgap which can be described by the Shockley-Read-Hall (SRH) formalism.

Radiative recombination occurs when an electron in the conduction band directly recombines with a hole in the valance band thereby emitting a photon with an energy which is at least as high as the bandgap energy. It is the reverse process of the generation of the electron-hole pair by photon absorption. As silicon is an indirect semiconductor, the process requires a phonon for conservation of the momentum. The recombination rate is proportional to the product of electron and hole concentration since both species are involved in the process. For the calculation of the net recombination rate, the recombination rate of the non-illuminated process is subtracted from the total recombination rate

$$U_{\text{rad}} = B \times \left(n\,p - n_{\text{i}}^2\right), \qquad (4.4)$$

where B is a temperature dependent coefficient. In silicon at room temperature $B = 9.5 \times 10^{-15}\,\text{cm}^3\,\text{s}^{-1}$ [26]. By inserting Equation 4.4 in 4.2 the corresponding radiative lifetime is

$$\tau_{\text{rad}} = \frac{1}{B\ (n_0 + p_0 + \Delta n)} \qquad (4.5)$$

Auger recombination is a three quasi-particle process where an electron drops to the valence band and transfers its energy to another electron or hole instead of a photon. The recombination rate is proportional to the product of carriers which are involved. Coulomb attraction between electrons and holes as well as phonon-assisted Auger recombination makes it difficult to describe the Auger recombination in a parametrization, where the single parameters can be attributed to physical constants. Therefore an empirical parametrization of Kerr and Cuevas is used in the following analysis and in the finite element simulations for the recombination rate [27]

$$U_{\text{Auger}} = np\left(1.8 \times 10^{-24} n_0^{0.65} + 6.0 \times 10^{-25} p_0^{0.65} + 3.0 \times 10^{-27} \Delta n^{0.8}\right) \qquad (4.6)$$

and the lifetime

$$\tau_{\mathrm{Auger}} = \frac{\Delta n}{U_{\mathrm{Auger}}}. \tag{4.7}$$

The total intrinsic recombination is the sum of radiative recombination in Equation 4.4 and Auger recombination in Equation 4.6 and is the limit for a defect free silicon wafer. The resulting intrinsic lifetime is then:

$$\tau_{\mathrm{intr}} = \frac{\Delta n}{np\left(1.8 \times 10^{-24} n_0^{0.65} + 6.0 \times 10^{-25} p_0^{0.65} + 3.0 \times 10^{-27} \Delta n^{0.8} + 9.5 \times 10^{-15}\right)}. \tag{4.8}$$

The extrinsic recombination is recombination via energy levels in the bandgap caused by dislocations or impurities in the semiconductor. The recombination activity of the energy levels in the bandgap depends on their capture cross sections for electrons σ_{n} and for holes σ_{p}. The recombination rate is well described in the case of a fixed defect energy level E_{t} and a fixed defect density of N_{t} by the Shockley-Read-Hall (SRH) formalism [28, 29]:

$$U_{\mathrm{SRH}} = \frac{\left(np - n_{\mathrm{i}}^2\right)}{\tau_{\mathrm{n0}}\left(p + p_1\right) + \tau_{\mathrm{p0}}\left(n + n_1\right)}, \tag{4.9}$$

where

$$\begin{aligned} \tau_{\mathrm{n0}} &= \frac{1}{N_{\mathrm{t}} \sigma_{\mathrm{n}} v_{\mathrm{th,n}}} \\ \tau_{\mathrm{p0}} &= \frac{1}{N_{\mathrm{t}} \sigma_{\mathrm{p}} v_{\mathrm{th,p}}} \end{aligned} \tag{4.10}$$

are the electron and hole capture times of the defect level, where $v_{\mathrm{th,n}} = 2.0 \times 10^7\,\mathrm{cm/s}$ and $v_{\mathrm{th,p}} = 1.7 \times 10^7\,\mathrm{cm/s}$ are the thermal velocities for electrons and holes at 300 K, respectively [30], and

$$\begin{aligned} n_1 &= n_{\mathrm{i}} \exp\left(\frac{E_{\mathrm{t}} - E_{\mathrm{i}}}{kT}\right) \\ p_1 &= n_{\mathrm{i}} \exp\left(\frac{E_{\mathrm{i}} - E_{\mathrm{t}}}{kT}\right) \end{aligned} \tag{4.11}$$

are the densities of occupied states for electrons and holes. E_{i} is the intrinsic Fermi level. The resulting SRH carrier lifetime is

$$\tau_{\mathrm{SRH}} = \frac{\tau_{\mathrm{p0}}\left(n_0 + n_1 + \Delta n\right) + \tau_{\mathrm{n0}}\left(p_0 + p_1 + \Delta n\right)}{p_0 + n_0 + \Delta n}. \tag{4.12}$$

Under consideration of all recombination paths the bulk lifetime is

$$\frac{1}{\tau_{\mathrm{b}}} = \frac{1}{\tau_{\mathrm{rad}}} + \frac{1}{\tau_{\mathrm{Auger}}} + \frac{1}{\tau_{\mathrm{SRH}}}. \tag{4.13}$$

Figure 4.1 shows a notional injection dependent bulk lifetime of a monocrystalline silicon wafer with a doping density of $N_{\mathrm{A}} = 3 \times 10^{16}\,\mathrm{cm}^{-3}$. The electron capture time is $\tau_{\mathrm{n0}} = 20\,\mu\mathrm{s}$ and the hole capture time is $\tau_{\mathrm{p0}} = 40\,\mu\mathrm{s}$ with a trap energy level of $E_{\mathrm{c}} - E_{\mathrm{t}} = 0.56\,\mathrm{eV}$.

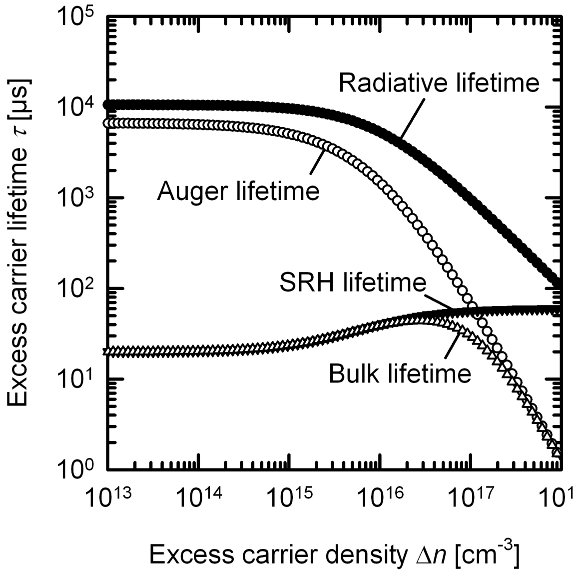

Figure 4.1: *Carrier lifetimes τ of p-type silicon with $N_\mathrm{A} = 3\times10^{16}\,\mathrm{cm}^{-3}$ ($0.5\,\Omega\mathrm{cm}$) as a function of excess carrier density Δn. In low level injection ($\Delta n < 2\times10^{14}\,\mathrm{cm}^{-3}$) the bulk lifetime is independent of Δn and limited by SRH recombination. In this example the electron capture time is $\tau_\mathrm{n0} = 20\,\mu\mathrm{s}$ and the hole capture time is $\tau_\mathrm{p0} = 40\,\mu\mathrm{s}$ with a trap energy level of $E_\mathrm{c} - E_\mathrm{t} = 0.56\,\mathrm{eV}$. In high injection ($\Delta n > 10^{17}\,\mathrm{cm}^{-3}$) the bulk lifetime is decreasing with increasing Δn and limited by Auger recombination.*

4.1.2 Surface recombination

Additional to the silicon bulk the surface also contributes to the recombination. Refering to our cell concepts described in Section 2.3 on page 8, the surface regions like the non diffused passivated front surface as well as passivated and contacted emitter and back surface field regions all contribute individually to the total recombination. In bulk silicon the valence electrons of the silicon are bonded in the silicon lattice. At the silicon surface the discontinuity in the lattice leads to non-bonded electrons which are named dangling bonds. These dangling bonds have various bonding angles due to varying distances from one surface atom to the other. Therefore the energy levels of these dangling bonds are distributed over the complete bandgap [31–33]. The recombination rate can be calculated by an extended SRH formalism by integrating the defect density over the bandgap energy:

$$U_\mathrm{it} = \left(n_\mathrm{s}p_\mathrm{s} - n_\mathrm{i}^2\right)\int_{E_\mathrm{V}}^{E_\mathrm{C}} \frac{v_\mathrm{th}D_\mathrm{it}\left(E\right)dE}{\sigma_\mathrm{p}^{-1}\left(E\right)\left(n_\mathrm{s} + n_1\left(E\right)\right) + \sigma_\mathrm{n}^{-1}\left(E\right)\left(p_\mathrm{s} + p_1\left(E\right)\right)}, \tag{4.14}$$

where n_s and p_s are the concentrations of electrons and holes at the surface, respectively, and $D_\mathrm{it}(E)$ is the density of states per energy interval. Since the recombination is per area and not per volume, no lifetime can directly be defined from this recombination. Instead, a surface recombination velocity (SRV) is defined:

$$S = \frac{U_{\mathrm{it}}}{\Delta n_{\mathrm{s}}} \tag{4.15}$$

The recombination decreases with decreasing energy densities, decreasing concentration of carriers at the surface, and decreasing capture cross sections. The decrease of carrier concentrations can be achieved by an electric field, which can, for example, be caused by fixed charges in a dielectric layer like silicon nitride ($\mathrm{SiN_x}$), silicon oxide ($\mathrm{SiO_2}$), or aluminum oxide ($\mathrm{AlO_x}$) deposited on the surface. Highly doped regions at the surface also reduce the carrier concentration of the opposite charge type. By the law of mass action in Equation 4.1 the concentration of one carrier species is reduced by increasing the concentration of the other. Energy densities are decreased by saturation of the dangling bonds, for example with oxygen or hydrogen. The latter is incorporated in dielectric layers like $\mathrm{SiN_x}$, $\mathrm{SiO_2}$, $\mathrm{AlO_x}$, or hydrogenerated amorphous silicon (a-Si). The capture cross sections are also influenced by the dielectric layers.

Besides the recombination directly at the surface of the silicon additional recombination takes place below the surface. Space charge regions caused by field effect passivation, highly doped regions like emitters or back surface fields, or surface damaged regions are the origin of this recombination. An effective surface recombination at a virtual surface at the interface from bulk silicon to the region of this recombination takes all these effects into account:

$$S_{eff} = \frac{U_{\mathrm{s,eff}}}{\Delta n_{\mathrm{s}}} = \frac{U_{\mathrm{it}} + U_{\mathrm{scr}} + U_{\mathrm{sl}} + U_{\mathrm{dam}}}{\Delta n_{\mathrm{s}}}, \tag{4.16}$$

with Δn_{s} being the excess carrier density at the virtual surface.

In this work, highly doped surface regions are treated as one dimensional boundaries [12]. An effective surface is introduced at the emitter to base interface. This means that recombination in the bulk of the emitter and at its surfaces is included in an effective SRV S_{eff}, which corresponds to an effective saturation current density of:

$$J_{\mathrm{rec,eff}} = q \times S_{\mathrm{eff}} \times \Delta n. \tag{4.17}$$

4.2 Carrier lifetime measurement techniques

In the previous Chapter 4.1 we discussed the various recombination paths in silicon. In order to analyze our solar cells we have to access the recombination properties experimentally. A bulk lifetime τ_{bulk} was introduced as the time difference between generation and recombination of an electron-hole pair in the bulk. Since there is no experimental access to this bulk lifetime an effective lifetime τ_{eff}, which includes bulk and surface recombination, is measured. For the determination of the saturation current densities, which impact the cell conversion efficiency, the effective lifetime of test samples is measured. Therefore it is essential to understand the dependence of the effective lifetime on bulk and surface recombination. The effective lifetime can be written as

$$\frac{1}{\tau_{\mathrm{eff}}} = \frac{1}{\tau_{\mathrm{b}}} + \frac{1}{\tau_{\mathrm{s}}}, \tag{4.18}$$

where τ_s is the surface lifetime. Solving the semiconductor transport equations [34] the surface lifetime is given by

$$\frac{1}{\tau_\mathrm{s}} = \frac{\Delta n_\mathrm{f}}{\Delta n_\mathrm{av}} \times \frac{S_\mathrm{f}}{W} + \frac{\Delta n_\mathrm{r}}{\Delta n_\mathrm{av}} \times \frac{S_\mathrm{r}}{W}, \tag{4.19}$$

where W is the wafer thickness, Δn_av is the average excess carrier density in the wafer, Δn_f and Δn_r are the excess carrier densities at the front and rear (effective) surface, and S_f and S_r are the front and rear effective surface recombination velocities, respectively. With the assumption that the carriers are distributed homogeneously in the wafer ($\Delta n_\mathrm{av} = \Delta n_\mathrm{f} = \Delta n_\mathrm{r}$), which is a good approximation for a well passivated wafer surface at steady state conditions, Equation 4.19 simplifies to

$$\frac{1}{\tau_\mathrm{s}} = \frac{S_\mathrm{f} + S_\mathrm{r}}{W}. \tag{4.20}$$

If additionally the front and the rear surface recombination velocities are equal $S = S_\mathrm{f} = S_\mathrm{r}$, Equation 4.20 further simplifies to:

$$\frac{1}{\tau_\mathrm{s}} = \frac{2S_\mathrm{f}}{W}. \tag{4.21}$$

Quantitatively, Equation 4.21 is accurate to a change in S of ±10 % as long as $S < W/D_a$ and $\tau_\mathrm{b} > W^2/D_a$, with D_a being the ambipolar diffusion coefficient [34]. The ambipolar diffusion coefficient is $D_a = (n+p) / (n/D_p + p/D_n)$, where D_n is the diffusion coefficient of the electrons and D_p is the diffusion coefficient of the holes. In low injection the ambipolar diffusion coefficient simplifies to the minority carrier diffusion coefficient. In p-type material it is $D_a = D_n$ whereas in n-type material it is $D_a = D_p$. Some of the test samples in this work can be analyzed with these equations.

We also analyze non-symmetric test samples with one passivated surface and one metalized surface, where the recombination is high. The carrier concentration at the metalized surface is thus much lower than the carrier concentration at the well passivated surface. However, if the carriers are not distributed homogeneously in the wafer, Equation 4.21 is no longer accurate. Instead, the second order differential transport equation have to be solved. Taking into account the boundary condition at the surface, that the product of minority carrier concentration and Diffusion constant D_a equals the product of surface recombination velocity (S_f or S_r) and minority carrier concentration, one arrives at following Equation 4.22, as done by Oredian [35]:

$$\frac{1}{\tau_\mathrm{s}} = \alpha_0^2 \times D_a. \tag{4.22}$$

α_0 is the solution of

$$\tan(\alpha_0\ W) = \frac{\alpha_0 \times D_a \times (S_\mathrm{f} + S_\mathrm{r})}{{\alpha_0}^2 \times {D_a}^2 - S_\mathrm{f} \times S_\mathrm{r}}. \tag{4.23}$$

Our test samples for the determination of the surface recombination show a strong increase of the effective carrier lifetime with decreasing injection levels. Such an injection dependence of the lifetime at lower injection densities cannot be described by any type of recombination mechanism. Instead this observation is caused by a measurement artefact. An increase of the lifetime with decreasing injection densities is known from trapping [36] or depletion region modulation (DRM) effects [37,38]. Trapping depends on the defect levels in the silicon bulk and is independent on the wafer thickness, whereas DRM depends on a depletion region of the surface, which depends on the sample thickness. The thinner the wafer the higher the injection density where the lifetime is significantly influenced by DRM.

The effective lifetime has to be measured for the determination of the surface recombination and the bulk recombination, which is essential for solar cell characterization and for obtaining input parameters for solar cell simulations. There are different measurement techniques to do this. Each has advantages and disadvantages and is suitable for different circumstances. In this work, inductive-coil photoconductance decay is used for the measurement of the average effective lifetime in dependence of a wide range of injection levels of non-metalized test samples. Infrared lifetime mapping is necessary for the determination of the spatially resolved effective lifetime of metalized test samples. In contrast to these two lifetime measurement techniques the microwave-detected photoconductance decay technique is capable of measuring effective carrier lifetimes of less than 3 μs, which occur in test samples with a full area metallization or a bare i.e. unpassivated surface. All three measurement techniques are described in the following.

4.2.1 Inductive-coil photoconductance

The inductive-coil photoconductance decay technique is used for measuring the effective carrier lifetime in dependence of a wide range of injection levels of test samples for the determination of saturation current densities. Figure 4.2 shows a schematic setup of the inductive-coil photoconductance decay measurement tool. Inductive photoconductance-coil measures the conductivity of the wafer by inductive coupling to a coil. The wafer is illuminated by a flash. The illumination changes the excess carrier density Δn_{av} of the wafer and therefore the conductivity of the wafer. The excess carrier density can be calculated from the excess conductivity $\Delta\sigma$ according to

$$\Delta\sigma = q \times W \times (\mu_n + \mu_p) \times \Delta n_{\mathrm{av}}, \tag{4.24}$$

where μ_n and μ_p are the electron and hole mobilities which are well known for p-type and n-type silicon and are independent of the electron and hole concentration in low level injection [39]. The time dependence of the excess carrier concentration is given by the continuity equation

$$\frac{\partial \Delta n}{\partial t} = G(t) - U(t) + \frac{1}{q}\vec{\nabla}\vec{J}. \tag{4.25}$$

where G is the generation rate of excess carriers, U is the recombination rate of excess carriers and J is the current density. As long as the current perpendicular to the wafer is zero, Equation 4.25 simplifies to

$$\frac{\partial \Delta n_{\mathrm{av}}}{\partial t} = G_{\mathrm{av}}(t) - U_{\mathrm{av}}(t), \tag{4.26}$$

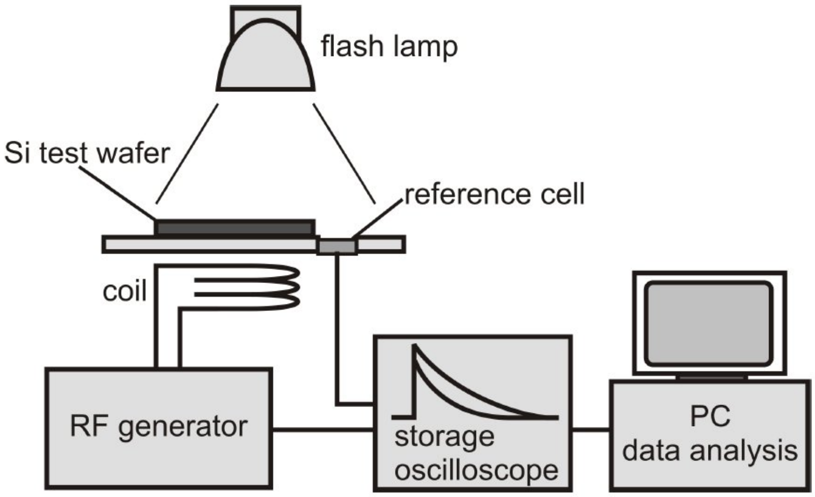

Figure 4.2: *Schematic of the inductive-coil photoconductance tool. The wafer is placed on top of a coil which measures the conductance using a rf-generator. The flash lamp illuminates the wafer to generate excess carriers and the reference cell determines the light intensity.*

where G_{av} is the average generation rate of excess carriers and U_{av} is the average recombination rate of excess carriers. In combination with Equation 4.3 the effective lifetime is [40]

$$\tau_{\mathrm{eff}} = \frac{\Delta n_{\mathrm{av}}}{G_{\mathrm{av}}(t) - \partial \Delta n_{\mathrm{av}}/\partial t}. \tag{4.27}$$

There are three measurement conditions: transient, quasi-steady-state and steady-state. In the transient case a short flash of about 30 μs is used to generate excess carriers. The evaluation begins after the flash is turned off, when no carriers are generated but only recombine. In this case Equation 4.27 simplifies to

$$\tau_{\mathrm{eff}} = -\frac{\Delta n_{\mathrm{av}}}{\partial \Delta n_{\mathrm{av}}/\partial t}. \tag{4.28}$$

During the decay of the flash intensity the conductivity is measured continuously. Each measured conductivity value corresponds to a pair of excess carrier density and effective lifetime. The measurement time of an injection-dependent lifetime measurement is a few times of the effective lifetime. The advantage of the transient measurement is the independence of the excess carrier density of the generation rate. The independence of the generation is especially useful for test samples which are very thin or laterally inhomogeneously coated, so that the optical properties are not exactly known. However, only lifetimes which are much longer than the flash decay time can be evaluated.

Shorter lifetimes can be measured under quasi-steady-state or steady-state conditions. In the quasi-steady-state mode a flash with a longer decay time of about 2 ms is used. In a time interval t_{ss} when the intensity of the flash I and therefore the generation rate in the wafer G_{av} is close to steady-state $\left(t_{\mathrm{ss}} << \frac{\partial I/\partial t}{I}\right)$, the effective lifetime can be calculated by Equation 4.27. The light intensity is measured by a reference solar cell, where the short-circuit current density in dependence of the light intensity is known. The generation rate in the wafer can be calculated under consideration of the optical properties of the test sample and the measured light intensity.

In steady-state conditions an infrared diode array operating at a wavelength of 950 nm is used as illumination source. It generates a time independent and homogeneous excess carrier density in the wafer. Therefore Equation 4.27 simplifies to

$$\tau_{\mathrm{eff}} = \frac{\Delta n}{G_{\mathrm{av}}}. \tag{4.29}$$

4.2.2 Infrared lifetime mapping

Infrared lifetime mapping (ILM) is used for measuring the spatially resolved effective carrier lifetime of metalized test samples for the determination of saturation current densities at the contacts. Figure 4.3 shows the principle of the ILM technique [41, 42]. The camera based method provides a spatially resolved image of the lifetime compared to an average lifetime evaluated by the inductive-coil photoconductance method. We use the dynamic ILM technique with the lock-in approach for the evaluation of the effective carrier lifetime. The sample is heated to a temperature of 70 °C to generate free carrier emission. A modulated lamp illuminates the wafer at a wavelength of 950 nm to generate excess carriers. An infrared camera measures the infrared free carrier emission of the test sample, which is proportional to the free carrier concentration.

Figure 4.4 shows that four images are taken during one lock-in period. The first image is recorded after turning on the infrared light source, the second image is taken after steady-state conditions of the carrier concentration under illumination are reached. The third image is recorded directly after turning off the light source and the fourth image after steady-state conditions of the carrier concentrations are reached without illumination. Each image contains information of the carrier density in the sample. Additionally, a constant signal due to thermal radiation of the majority carriers and the surroundings is included in the signal. The four images recorded during one lock-in period are multiplied with coefficients of a sin- and a cos- function which are in phase with the modulated excitation. Sin- and cos- related images are generated by summing up the four images. The difference between image 4 and image 2 is the sin-relation S_{sin} and the difference between image 3 and image 1 is the cos-relation S_{cos}. Both relations are free of background signal by using this method. Equation 4.30 and 4.31 show the sin- and cos-relations by inserting Equation 4.3

$$\begin{aligned} S_{\mathrm{cos}} &= \int_0^{t_{\mathrm{int}}} \Delta n(t)dt - \int_{\frac{t_{\mathrm{p}}}{2}}^{\frac{t_{\mathrm{p}}}{2}+t_{\mathrm{int}}} \Delta n(t)dt \\ &= S_{\mathrm{st-st}} \times \left(t_{\mathrm{int}} - 2 \times \tau_{\mathrm{eff}}\left(1 - \exp\left(-\frac{t_{\mathrm{int}}}{\tau_{\mathrm{eff}}}\right)\right)\right) \end{aligned} \tag{4.30}$$

$$S_{\mathrm{sin}} = \int_{\frac{t_{\mathrm{p}}}{4}}^{\frac{t_{\mathrm{p}}}{4}+t_{\mathrm{int}}} \Delta n(t)dt - \int_{\frac{3t_{\mathrm{p}}}{4}}^{\frac{3t_{\mathrm{p}}}{4}+t_{\mathrm{int}}} \Delta n(t)dt$$

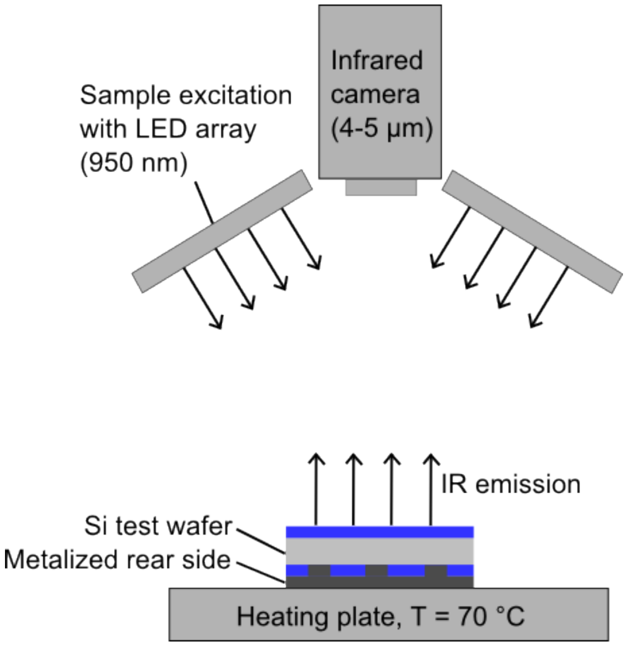

Figure 4.3: *Principle of infrared lifetime mapping. The sample is heated to a temperature of* 70 °C *to generate free carrier emission. A modulated lamp illuminates the wafer sample at a wavelength of* 950 nm *to generate excess carriers. An infrared camera measures the infrared free carrier emission of the test sample, which is proportional to the free carrier concentration.*

$$= S_{\mathrm{st-st}} \times \left(t_{\mathrm{int}} - 2 \times \tau_{\mathrm{eff}} \left(\exp\left(-\frac{t_{\mathrm{p}}}{4\,\tau_{\mathrm{eff}}} \right) - \exp\left(-\frac{t_{\mathrm{p}} + 4\,t_{\mathrm{int}}}{4\,\tau_{\mathrm{eff}}} \right) \right) \right) \qquad (4.31)$$

where $S_{\mathrm{st-st}}$ is the steady state signal with illumination but without the influence of the background and t_{p} is the time of one lock-in period. Using the definition of the phase of the lock-in method $\Phi = \arctan(S_{\cos}/S_{\sin})$ and inserting Equations 4.30 and 4.31 eliminates $S_{\mathrm{st-st}}$ and results in

$$\Phi = \arctan\left(\frac{\left(t_{\mathrm{int}} - 2 \times \tau_{\mathrm{eff}} \left(1 - \exp\left(-\frac{t_{\mathrm{int}}}{\tau_{\mathrm{eff}}} \right) \right) \right)}{\left(t_{\mathrm{int}} - 2 \times \tau_{\mathrm{eff}} \left(\exp\left(-\frac{t_{\mathrm{p}}}{4\,\tau_{\mathrm{eff}}} \right) - \exp\left(-\frac{t_{\mathrm{p}}+4\,t_{\mathrm{int}}}{4\,\tau_{\mathrm{eff}}} \right) \right) \right)} \right) \qquad (4.32)$$

All parameters are known except Φ and τ_{eff}. A look-up table is generated using the relation between Φ and τ_{eff}. The phase of each pixel in the image is correlated with the lifetime, thus a lifetime image is generated. The generation of a look-up table is necessary, as Equation 4.32 solves for Φ if τ_{eff} is known, but the equation is not invertible.

Some test structures investigated in this work have different ratios of metalized to passivated area on the rear side. Test samples with a high ratio of metalized to passivated area show low lifetimes. These low lifetimes correspond to a low phase value. Since the phase value is calculated by dividing a low cos-signal by a low sin-signal, the noise ratio increases and the lifetime cannot be evaluated any more. These samples can be evaluated

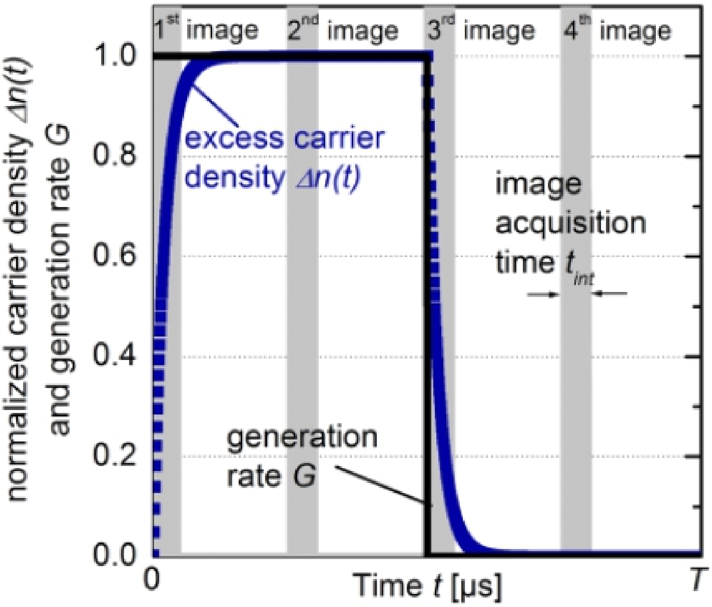

Figure 4.4: *Time dependence of the generation rate and the excess carrier density. Images at different conditions are taken for the evaluation of the excess carrier density and lifetime.*

by a dynamically calibrated steady state ILM. Using this technique, samples with the same emissivity but a high lifetime can be evaluated by the known dynamic ILM which is used for calibrating the steady-state lifetime measurements. This calibration can be applied on the steady-state ILM for samples with the same emissivity but low lifetimes. The staedy-state lifetime is determined by subtracting the fourth from the second image and is calibrated afterwards.

The excess carrier density can be calculated by Equation 4.29 using the known generation rate. The measurement time depends on the lifetime of the wafer. With adequate lifetimes of a few 100 μs it takes less than a minute to take a spatially resolved lifetime image. An injection dependent lifetime can be measured by taking images with different steady-state illumination intensities.

4.2.3 Microwave-detected photoconductance decay

The microwave-detected photoconductance decay (MW-PCD) measurement setup is capable of measuring very low effective carrier lifetimes spatially resolved. This is used for measuring laterally inhomogeneous and very low effective carrier lifetimes of the test samples of the selective laser ablation process. A schematic setup is shown in Figure 4.5. Excess carriers are generated with a short laser pulse with a wavelength of 908 nm and a pulse length of 200 ns. The measurement begins directly after the laser pulse and measures the decay of the excess carrier concentration. The carrier concentration is measured by the reflected intensity of microwaves. The reflected intensity depends nonlinearly on the concentration of carriers. Only in the small signal case the change in the reflected intensity is proportional to the change in excess carrier densities. A white bias light generates additional excess carriers so that the absolute excess carrier concentration is in the range of interest even though it is not exactly known. The measured lifetimes are therefore differential values which are not necessarily the same as in a solar cell in thermal equilibrium [43, 44]. However, the effective lifetime can now be extracted from the decay of the reflected microwave intensity.

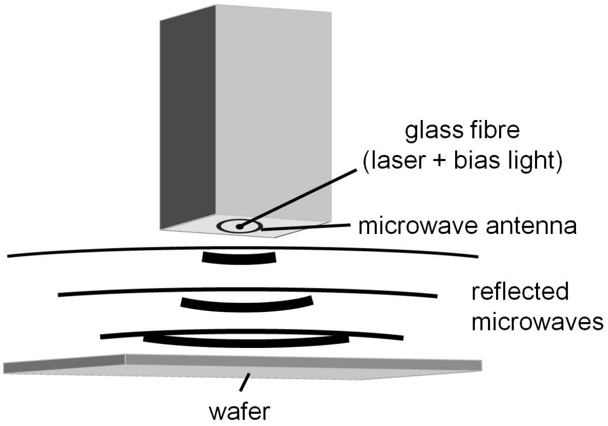

Figure 4.5: *Schematic setup of the MW-PCD tool. The effective lifetime is extracted from the decay of the reflected microwave intensity. Excess carriers are generated by a laser and a bias light.*

The measurement time for one single point is in the range of the carrier lifetime. For a spatially resolved lifetime image, the wafer has to be scanned with the tool. Therefore the measurement time multiplies by the number of measurement points. For a large wafer the MW-PCD technique takes much longer than the infrared lifetime technique. The MW-PCD allows for measuring very short carrier lifetimes since it is a differential technique whereas the infrared lifetime technique measures the absolute signal where the signal to noise ratio is very small at low carrier lifetimes.

4.3 Results and discussion of the saturation current densities and bulk lifetime determination

The understanding of the recombination properties of the different parts of a solar cell is essential in order to reduce those factors limiting the solar cell energy conversion efficiency. A cross section of the back-contact back-junction cell which is manufactured and characterized in this work is shown in Figure 4.6. The recombination is quantified by determination of the saturation current densities associated with all surfaces, interfaces and bulk recombination. These saturation current densities are direct input parameters for our finite element solar cell simulation using the conductive boundary model (CoBo) [12]. Literature values are often not helpful to simulate experimental cells since the respective saturation current densities had often been measured for samples processed with other tools or with other process parameters. Therefore, the saturation current densities for the present analysis are extracted from measurements using test samples that are processed with the same tools and the same parameters as our solar cells. In the following we exemplarily show the analysis for the groups High which have a base doping of $N_\mathrm{A} = 3 \times 10^{16}\,\mathrm{cm}^{-3}$ and are passivated with an a-Si/SiN$_\mathrm{x}$ double layer. The analysis of the other groups is done in the same way and the results for all groups are shown in the tables. The bulk lifetime of the epitaxial layer is also determined by passivating the epitaxial layer and measure the effective lifetime.

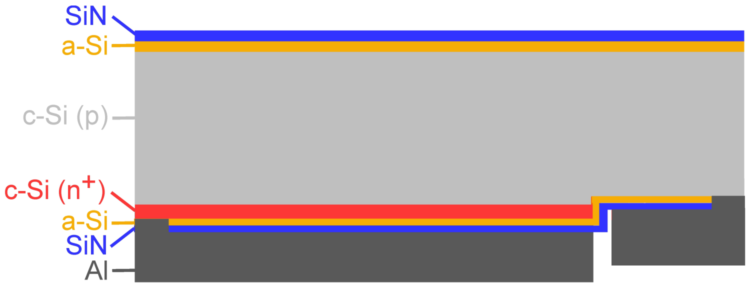

Figure 4.6: *Schematic cross section of the unit cell of the back-contact back-junction solar cell. The front surface shows a constant saturation current density due to the homogeneous passivation by a stack of a-Si/SiN$_\mathrm{x}$. The rear surface shows various saturation current densities due to the interdigitated finger structure and the partly metalized base and emitter fingers. The left side shows, that the emitter region is comprised of three different regions: a silicon to metal interface, an aluminum capped a-Si/SiN$_\mathrm{x}$ passivated surface and an a-Si/SiN$_\mathrm{x}$ passivated surface. The base region also has these three regions. The drawing is not to scale.*

4.3.1 Saturation current densities of the emitter regions

Figure 4.6 shows that the (n^+)-emitter has three different regions: The right part is passivated with an a-Si/SiN$_\mathrm{x}$ stack, the center part is also passivated with an a-Si/SiN$_\mathrm{x}$ stack and has an aluminum capping layer, whereas the left part is directly contacted by aluminum. Figure 4.7 shows schematic cross sections of the test structures. The three regions of the emitter are represented in these test structures. The $W = 300\,\mu m$-thick monocrystalline p-type wafer is lowly doped ($N_A = 7 \times 10^{13}\,\mathrm{cm}^{-3}$) which simplifies the evaluation of the saturation current density of the effective diffused surface. The diffusion, the passivation stack, and the aluminum deposition are prepared with the same process sequence as used for the solar cell.

Afterwards, the effective lifetime τ_eff of the test samples is measured by infrared lifetime mapping as described in Section 4.2.2. Infrared lifetime mapping allows for measuring the injection dependent carrier lifetime of metalized as well as non metalized samples, as long as the optical properties of the sample are known. The base is in high injection since the samples are measured at injection densities of $\Delta n = 10^{15}$ to $10^{16}\,\mathrm{cm}^{-3}$. Thus, the Shockley-Read-Hall lifetime SRH may be assumed to be independent of the injection density as

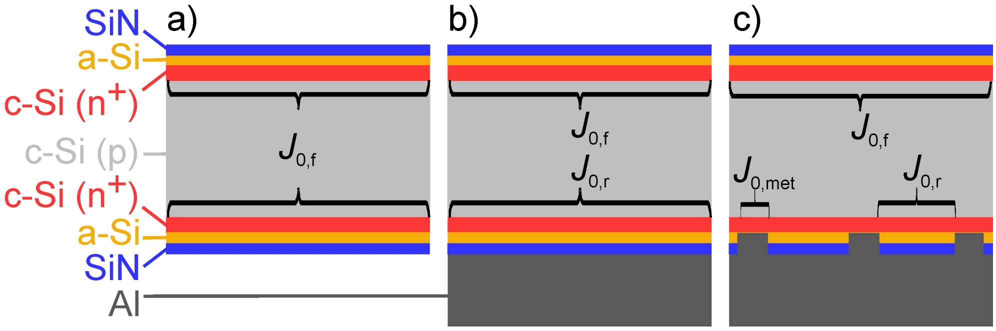

Figure 4.7: *Schematic cross section of the test structures for the determination of the emitter saturation current densities. The drawing is not to scale.*

shown in Figure 4.1. The emitter is always in low injection ($N_D = 10^{19}\text{cm}^{-3}$) and hence allows for calculating the saturation current density of the surfaces with the Kane-Swanson method [45]. In the case of a p-type base where $n_0 << p_0$ the combination of Equation 4.17 and Equation 3.9 simplifies to

$$S_{\text{eff}} = \frac{J_0}{qn_i^2} \times (N_A + \Delta n). \tag{4.33}$$

Since the electron concentration in the wafer in between the effective surfaces is homogeneous Equation 4.20 and Equation 4.13 can be applied to Equation 4.18. This results in the following effective lifetime:

$$\frac{1}{\tau_{\text{eff}}} = \frac{1}{\tau_{\text{rad}}} + \frac{1}{\tau_{\text{Auger}}} + \frac{1}{\tau_{\text{SRH}}} + \frac{S_f + S_r}{W}. \tag{4.34}$$

Combining Equation 4.33 and 4.34 and neglecting the non-limiting radiative recombination leads to the Kane-Swanson equation:

$$\frac{1}{\tau_{\text{eff}}} - \frac{1}{\tau_{\text{Auger}}} = \frac{1}{\tau_{\text{SRH}}} + \frac{J_{0,f} + J_{0,r}}{qn_i^2 W} \times (N_A + \Delta n) \tag{4.35}$$

In a first step the saturation current density $J_{0,f}$ which corresponds to the right emitter part in Figure 4.6 is determined using a symmetric structure as is shown in Figure 4.7a. In this case Equation 4.35 simplifies to

$$\frac{1}{\tau_{\text{eff}}} - \frac{1}{\tau_{\text{Auger}}} = \frac{1}{\tau_{\text{SRH}}} + \frac{2 \times J_{0,f}}{qn_i^2 W} \times (N_A + \Delta n). \tag{4.36}$$

In a second step the non-symmetric but laterally homogeneous structure of Figure 4.7b is analyzed using $J_{0,f}$ determined in the first step. $J_{0,r}$, which corresponds to the center part of the emitter region in Figure 4.6, directly follows from Equation 4.35. Geometry (c) of Figure 4.7 shows an additional lateral inhomogeneity. The saturation current densities of the different areas can be added by area weighting, since the electron density in the emitter does not change laterally. This is due to the high doping concentrations in the emitter compared to the carrier concentrations in the base. Equation 4.35 changes to

$$\frac{1}{\tau_{\text{eff}}} - \frac{1}{\tau_{\text{Auger}}} = \frac{1}{\tau_{\text{SRH}}} + \frac{J_{0,\text{f}} + r \times J_{0,\text{met}} + (1-r) \times J_{0,\text{r}}}{q n_{\text{i}}^{2} W} \times (N_{\text{A}} + \Delta n), \tag{4.37}$$

where the variable r denotes the ratio of metalized to total area. The saturation current density $J_{0,\text{met}}$ of the metalized part of the emitter, which corresponds to the emitter contact in the solar cell, can now be calculated with the known saturation current densities $J_{0,\text{f}}$ and $J_{0,\text{r}}$.

Now the results of these measurements and of the evaluations are presented. Figure 4.8 shows the injection dependent inverse lifetimes of the test samples shown in Figure 4.7. The curves shown in Figure 4.8 are measurements of test samples which are processed in the same way as the emitters in all investigated BC BJ cell groups, with the exception of group High-Full-BSF-Texture (▮). The five measurements show the lifetimes of the samples shown in Figure 4.7a and b and the lifetimes of three samples shown in Figure 4.7c with different ratios of metalized to total area. For the evaluation only one ratio of metalized to total area is needed, but it is helpful to test the consistence of this evaluation technique with the comparison of the results from different ratios of metallization.

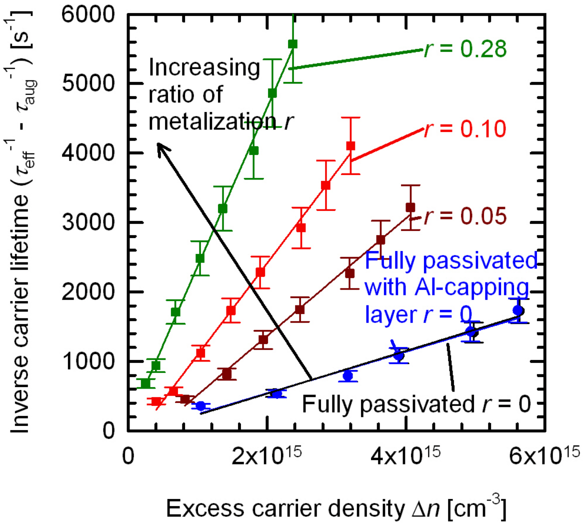

Figure 4.8: *Injection dependence of the inverse lifetime of the test samples for the determination of the saturation current densities of the emitter region measured with ILM [41,42]. The five measurements show the lifetimes of the samples shown in Figure 4.7a and b and the lifetimes of three samples shown in Figure 4.7c with different ratios of metalized to total area.*

Table 4.1 lists the saturation current densities with their uncertainties. The evaluation of all three ratios of metalized to total area show the same saturation current densities

Table 4.1: *Saturation current densities in* [fA cm^{-2}] *of the emitter regions of all groups*

	ratio of metalized to total area r	Groups High J_0 [fA cm^{-2}]	Groups Low J_0 [fA cm^{-2}]	High-Full-BSF-Texture (■) J_0 [fA cm^{-2}]
Fully passivated	0	110 ± 30	90 ± 28	80 ± 25
Fully passivated with Al-capping layer	0	110 ± 30	90 ± 28	80 ± 25
Partly metalized	0.05	5300 ± 1500	4300 ± 1200	-
	0.10	5400 ± 1350	4400 ± 1100	-
	0.28	4100 ± 900	3400 ± 750	-
	0.18	-	-	900 ± 300

for the metalized areas with a low uncertainty, proving the consistence of this evaluation technique. The values of the samples shown in Figure 4.7a and b are the same. This means that the aluminum evaporation does not degrade the passivation of the sample surface. The saturation current density is independent of the injection density but depends on the base doping concentration due to the different intrinsic carrier concentrations at different base doping concentrations. Table 4.1 lists the emitter saturation current densities, which consider the dependence on the base doping concentration, of passivated surfaces as well as metalized surfaces for all groups. These experimental values are input parameters for the later unit cell simulation.

4.3.2 Saturation current densities of the base region

We also determine the saturation current densities of the base surfaces. Figure 4.6 shows that three different types of base surface regions exist. The first type is the passivated front surface which is equal to the left part of the passivated base finger at the rear side. The second type is located at the rear. It is passivated and covered with aluminum. The third region is the metal contact. Figure 4.9a through c shows the schematic cross sections of the test structures used to measure the losses at the three types of base surfaces. The three regions of the base are represented in these test structures.

For the test structures we use a monocrystalline p-type wafer that has the same doping concentration as the solar cell base. The acceptor concentration is $N_{\mathrm{A}} = 3 \times 10^{16}\,\mathrm{cm}^{-3}$. Each of the three test structures is prepared on wafers with thicknesses of $W = 100\,\mu$m, $130\,\mu$m, $170\,\mu$m, and $300\,\mu$m. This allows for the separation of surface and bulk recombination [46]. The same process parameters as in the cell processes are used in these experiments. Again, we measure the carrier lifetimes of the test samples by infrared lifetime mapping technique [41, 42]. The analysis of the base surface recombination velocities is done in four steps. First the SRV S_{f} of the symmetric sample in Figure 4.9a, which corresponds to

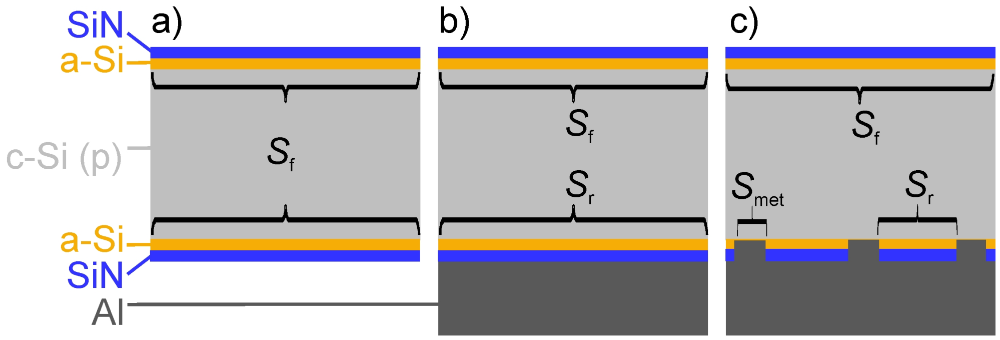

Figure 4.9: *Schematic cross section of the test structures for the determination of the base saturation current densities. The drawing is not to scale.*

the cell front surface and passivated rear base finger, is calculated with the combination of Equations 4.18 and 4.20:

$$\frac{1}{\tau_{\mathrm{eff},i}} - \frac{1}{\tau_{\mathrm{b}}} = \frac{S_{\mathrm{f}} + S_{\mathrm{r}}}{W_i}; i = [1 - 4], \tag{4.38}$$

assuming $S_{\mathrm{f}} = S_{\mathrm{r}}$ and using the results of the four samples with different thickness values which have the same bulk lifetime. In parallel the bulk lifetime τ_{b} is extracted by applying Equation 4.38 to the four different samples and assuming the same SRV for all samples. In a second step the non-symmetric but laterally homogeneous structure in Figure 4.9b is analyzed using S_{f} determined in the first step. The rear SRV S_{r}, which corresponds to the SRV of the passivated base finger covered by an aluminum layer in the solar cell, follows from Equation 4.38. The third step determines the SRV of the metalized area S_{met} which corresponds to the base contact in the cell. This determination is based on lifetime measurements of the samples shown in Figure 4.9c. This analysis is not straight forward and requires separate analysis [47]. Equation 4.38 would only be valid if the injection density is homogeneous in the whole sample. However, this is not the case in Figure 4.9c. Here, the injection density strongly decreases towards the metalized surfaces due to the high recombination at the metal/Si interfaces. In this case, the effective rear SRV can be calculated by combining Equation 4.22 and 4.23 and changing the definition of S_r to $S_{\mathrm{r,eff}}$:

$$S_{\mathrm{r,eff}} = \frac{\left(\sqrt{\left(\frac{1}{\tau_{\mathrm{eff}}} - \frac{1}{\tau_{\mathrm{bulk}}}\right) D_a} \times \tan\left(\sqrt{\left(\frac{1}{\tau_{\mathrm{eff}}} - \frac{1}{\tau_{\mathrm{bulk}}}\right) D_a}\right)\right) - S_f}{1 + \left(S_f \times \tan\left(\sqrt{\left(\frac{1}{\tau_{\mathrm{eff}}} - \frac{1}{\tau_{\mathrm{bulk}}}\right) D_a}\right) / \left(\sqrt{\left(\frac{1}{\tau_{\mathrm{eff}}} - \frac{1}{\tau_{\mathrm{bulk}}}\right) D_a}\right)\right)} \tag{4.39}$$

S_{f} and τ_{bulk} are determined in the first two steps. However, the injection density is not only inhomogeneous in the perpendicular direction, but also in the lateral direction on the contacted side, since the recombination is much higher at the contacts. Fischer [48] derived a closed analytical expression which takes the perpendicular and the lateral inhomogeneities in the sample into account:

$$S_{\mathrm{r,eff}} = \frac{D_a}{W}\left(\frac{L_{\mathrm{sp}}}{2W\sqrt{\pi r}} \times \arctan\left(\frac{2W}{L_{\mathrm{sp}}} \times \sqrt{\frac{\pi}{r}}\right) - \exp\left(-\frac{W}{L_{\mathrm{sp}}}\right) + \frac{D_a}{rWS_{\mathrm{met}}}\right)^{-1} + \frac{S_{\mathrm{r}}}{1-r} \tag{4.40}$$

where S_{met} is the SRV at the contacts and L_{sp} is the distance of two neighboring contact spots in each direction. S_{met} can be calculated by Equation 4.40 since all other values are known and $S_{\mathrm{r,eff}}$ is calculated by Equation 4.39. Saturation current densities are calculated from the SRVs to compare the emitter with the base surface recombination. The injection density of the solar cell at the maximum power point is in the range of 10^{13} to $10^{14}\,\mathrm{cm}^{-3}$. Since it is in low injection ($p_0 = N_{\mathrm{A}} >> \Delta n$), Equation 4.33 simplifies to:

$$J_0 = S_{\mathrm{eff}} \times q \times \frac{n_{\mathrm{i}}^2}{N_{\mathrm{A}}}. \tag{4.41}$$

The measurements were performed for four different thicknesses. In the following the results of these measurements and of the evaluations of the 100 μm-thick samples and the 300 μm-thick samples are presented. Figure 4.10 shows the injection dependent lifetime of the test samples shown in Figure 4.9. Figure 4.10a shows the 100 μm-thick samples and Figure 4.10b shows the 300 μm-thick samples. Each thickness is used for fabricating fully passivated samples and samples which are partly metalized. The lifetime decreases with increasing metallization ratio due to the increased area of metal to silicon contacts, which feature high recombination. The partly metalized samples are also measured after laser ablation of the dielectric before metallization. Figure 4.10 shows that the lifetime is the same before and after metallization. Therefore the recombination rate is the same for bare silicon surfaces and for metal/silicon interfaces.

The lifetimes increase at injection densities below $3 \times 10^{14}\,\mathrm{cm}^{-3}$ in the 100 μm-thick samples and below $1 \times 10^{14}\,\mathrm{cm}^{-3}$ in the 300 μm-thick samples. Since the increase in lifetime starts at different injection levels for differently thick samples, the passivation stack seems to induce a depletion region, as described in Chapter 4.2. A simulation with a surface charge density of $6 \times 10^{11}\,\mathrm{cm}^{-2}$, which is reasonable for dielectric layers, is shown in Figure 4.10 and confirms this assumption. To evaluate the samples without the influence of the DRM all lifetimes are taken at $\Delta n_{\mathrm{av}} = 3 \times 10^{14}\,\mathrm{cm}^{-3}$ injection density.

The surface recombination velocities of the fully passivated samples shown in Figure 4.9a and Figure 4.9b can be calculated as previously described. The laterally inhomogeneous samples require separate analysis as explained above.

The effective rear surface recombination velocities are calculated from the lifetime shown in Figure 4.10 by using Equation 4.39. Figure 4.11 shows the injection dependent effective rear surface recombination velocities of the 100 μm and 300 μm-thick samples, respectively. The effective surface recombination velocity increases with increasing metallization ratio due to the increased area of the metal/silicon interface, which features high recombination. The effective rear SRV is not strongly dependent on the injection level at $\Delta n = 3 \times 10^{14}\,\mathrm{cm}^{-3}$ where the measurements are evaluated.

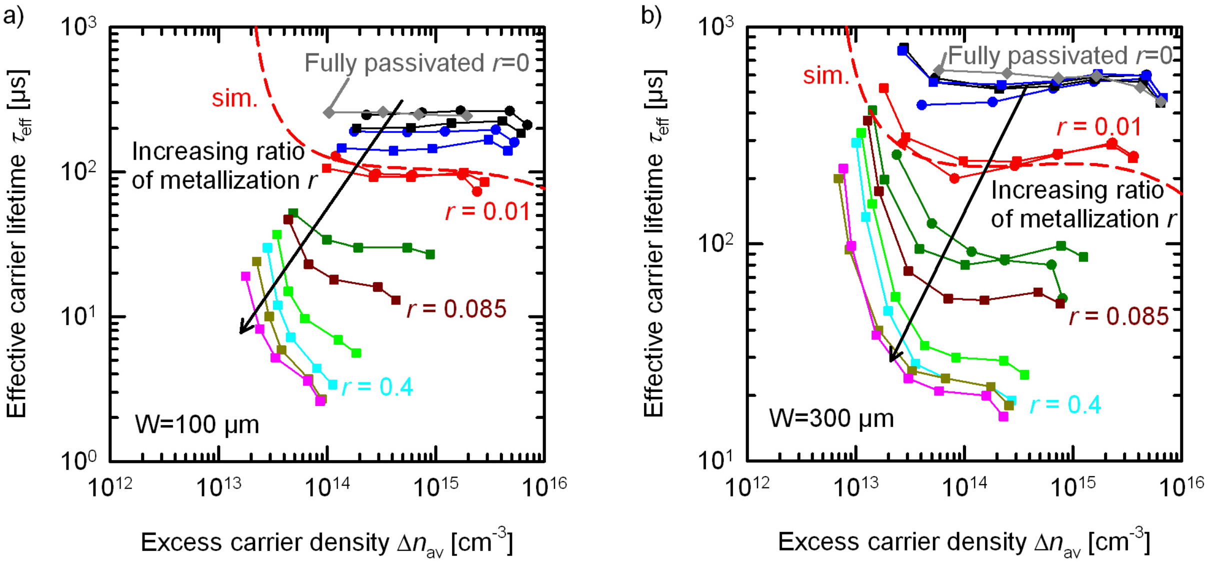

Figure 4.10: *Injection dependence of the lifetime of the test samples for the determination of the saturation current densities of the base region measured with ILM [41, 42]. Figure 4.10a shows the* 100 μm*-thick samples and Figure 4.10b shows the* 300 μm*-thick samples. Round symbols indicate the lifetime after metallization of fully passivated and partly passivated samples. Squared symbols indicate the lifetime after laser ablation of the dielectric layer but before metallization of partly metalized samples. Squared and round symbols show very similar values. Therefore the recombination, respectively the defect density, at the surface before and after metallization is the same. The dashed line is a simulation with a surface charge density of* $6 \times 10^{11}\,\mathrm{cm}^{-2}$.

Figure 4.12 shows the effective rear SRV in dependence of the spot distance. A decreasing spot distance is realized by an increasing ratio of metalized to total area. The measured effective rear SRVs before as well as after metallization are illustrated as data points. In addition, the effective rear SRVs calculated by using Equation 4.40 assuming different metalized SRVs S_{met} are plotted in the same graph (illustrated by lines). Both thicknesses show that the measured SRVs fit best if $S_{\mathrm{met}} > 10^5\,\mathrm{cm\,s^{-1}}$. $S_{\mathrm{r,eff}}$ does not depend on S_{met} if $S_{\mathrm{met}} > 10^5\,\mathrm{cm\,s^{-1}}$. The recombination current at the surface is not only proportional to the recombination velocity but also to the carrier density. This carrier density also depends on the generation and diffusion of the carriers to the surface.

As an example Figure 4.13 shows the depth dependent carrier profile of a 300 μm-thick sample. The front SRV is kept constant at $10\,\mathrm{cm\,s^{-1}}$ for all cases, which is a good approximation of the SRVs of the investigated samples. The carrier density decreases with increasing effective rear SRV. If the effective rear SRV exceeds $10^4\,\mathrm{cm\,s^{-1}}$ the carrier density profile does not change any more. This is due to the diffusion limited recombination at the rear surface, as previously described by Altermatt [49]. The diffusion of the carriers depends on the mobility of the carriers and thus on the doping concentration. Samples with

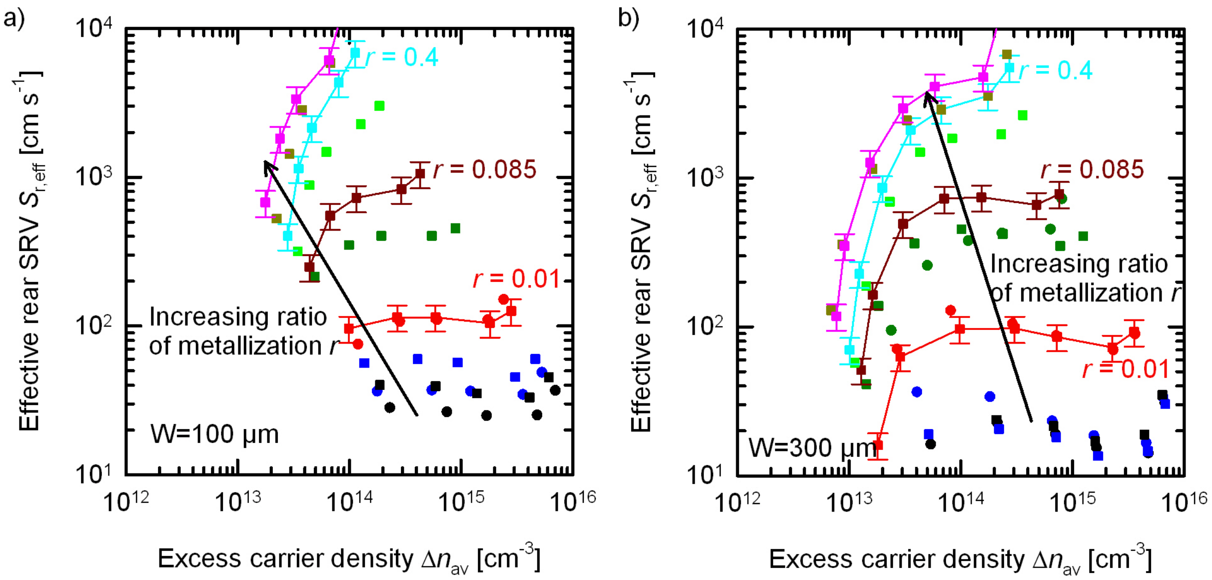

Figure 4.11: *Injection dependence of the effective rear surface recombination velocity of the test samples for the determination of the saturation current densities of the base region. Figure 4.11a shows the* 100 µm*-thick samples and Figure 4.11b shows the* 300 µm*-thick samples. Round symbols indicate the lifetime after metallization of fully passivated and partly metalized samples. Squared symbols indicate the lifetime after laser ablation of the dielectric layer but before metallization of partly metalized samples. Squared and round symbols show very similar values. Therefore the recombination, respectively the defect density, at the surface before and after metallization is the same.*

a doping concentration of $1.5 \times 10^{15}\,\mathrm{cm}^{-3}$, which is the concentration of the investigated cells of groups Low, show no significant change in the carrier distribution if the effective rear SRV exceeds $10^4\,\mathrm{cm\,s}^{-1}$.

The evaluation is done at an injection density of $3 \times 10^{14}\,\mathrm{cm}^{-3}$ whereas the base doping is $3 \times 10^{16}\,\mathrm{cm}^{-3}$ and $1.5 \times 10^{15}\,\mathrm{cm}^{-3}$, respectively. Therefore the base is in low-level injection and the saturation current densities can be calculated by using Equation 4.41 with the determined SRVs. Table 4.2 lists the saturation current densities of the passivated as well as metalized surfaces for all groups. These values are later used as input parameters for the unit cell simulation. Since the SRVs are injection independent, the saturation current densities are also injection independent in low-level injection. If the doping concentration decreases by a factor of 20, the SRVs of the passivated surfaces decrease by a factor of 4, whereas the saturation current densities increase by a factor of 2 due to the dependence on the doping concentration and the doping concentration dependent intrinsic carrier concentration. The recombination at the metalized surfaces are limited by carrier diffusion in the bulk. Therefore the SRV is nearly independent on the doping concentration. The saturation current density on the other hand increases with decreasing doping concentration due to the

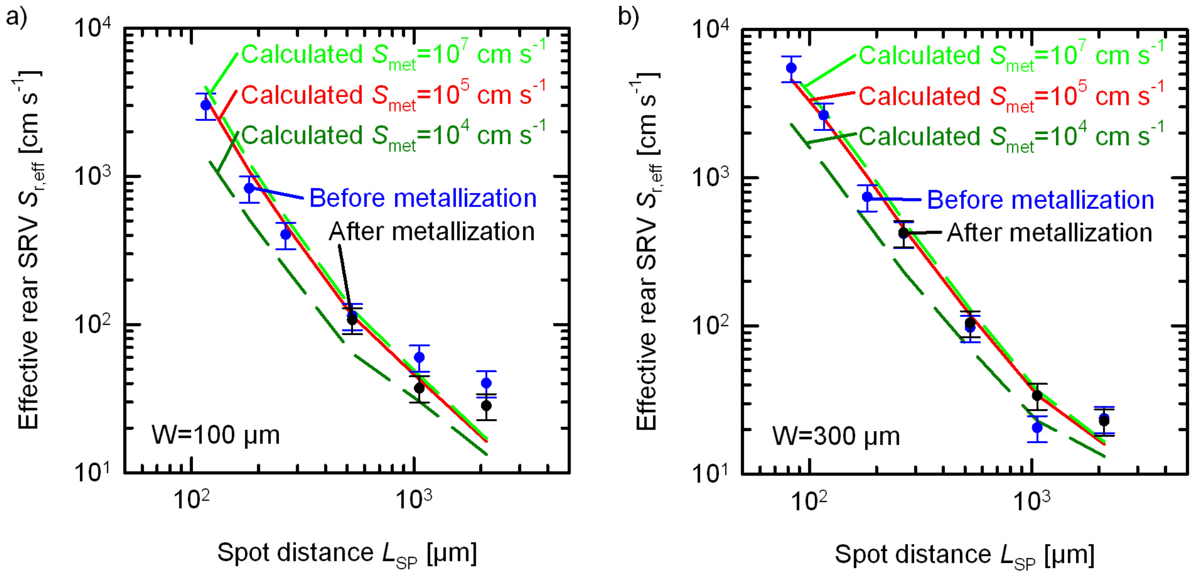

Figure 4.12: *Measured and calculated effective rear surface recombination velocities in dependence of the spot distance. Figure 4.12a shows the* 100 µm*-thick samples and Figure 4.12b shows the* 300 µm*-thick samples. The effective rear SRV increases with decreasing spot distance and increasing metallization ratio.*

inverse dependence on the doping concentration and the doping concentration dependent intrinsic carrier concentration.

In conclusion, a lower limit of the metalized surface recombination velocity is determined to be $10^5\,\mathrm{cm\,s^{-1}}$, which is also used for the finite element simulations. Higher SRVs do not change the recombination due to the diffusion limit of the carriers to the surface. Therefore the recombination at the metalized surface is determined precisely.

4.3.3 Bulk lifetime

The bulk material in our solar cells is an epitaxial layer. For the determination of the bulk lifetime of the epitaxial layer it is passivated with a stack of a 10 nm thick AlO_x layer for passivation and a SiN_x layer. This stack is similar to that used on the front surface of group High-Full-BSF-Texture (■). The effective lifetime of this sample is measured by quasi-steady-state photoconductance decay since the low lifetime and the low sample thickness leads to a too low signal-to-noise ratio in the infrared lifetime mapping approach. The SRV on the passivated epitaxial layer is assumed to be the same as on the wafer test samples for the determination of the SRV in Section 4.3.2 since the epitaxial layer has the same resistivity as the test samples. Now the bulk lifetime of the epitaxial layer can be calculated using Equation 4.38.

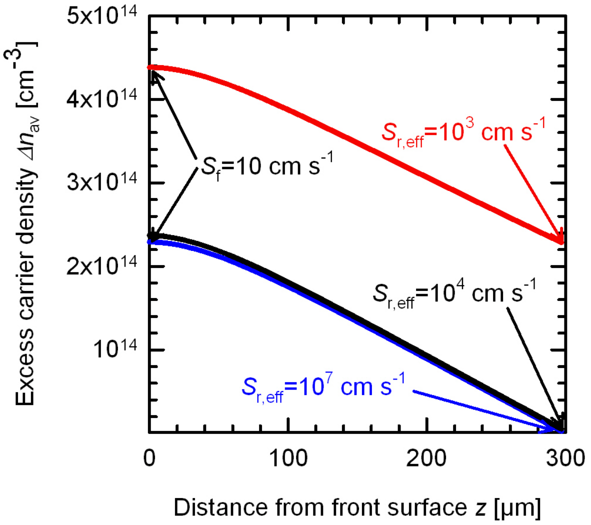

Figure 4.13: *Simulated excess carrier density in dependence of the distance to the front surface of the sample. The front SRV is kept constant at* $10\,\mathrm{cm\,s^{-1}}$*. The effective rear SRV is varied from* $10^3\,\mathrm{cm\,s^{-1}}$ *to* $10^7\,\mathrm{cm\,s^{-1}}$*. The carrier density is diffusion limited if the effective rear SRV is larger than* $10^4\,\mathrm{cm\,s^{-1}}$*.*

Figure 4.14 shows the injection dependent effective lifetime of the group High-Full-BSF-Texture (■). The low-level injection bulk lifetime is $20\,\mu$s in this group. Since the bulk lifetime varies from one epitaxy to another, we have to determine the bulk lifetime for every group individually. For the other five groups the low-level injection bulk lifetime cannot be determined with the same method due to depletion region modulation. The low-level injection lifetimes of the other groups are determined by electroluminescence imaging, as will be described in Section 7.1 on page 77 together with the other results of the electroluminescence analysis.

Table 4.2: *SRVs in* [$\mathrm{cm\,s^{-1}}$] *for the non-diffused samples and saturation current densities in* [$\mathrm{fA\,cm^{-2}}$] *of the base regions of all groups of investigated solar cells.*

	Groups High		Groups Low		High-Full-BSF-Texture (■)	
	J_0 [$\mathrm{fA\,cm^{-2}}$]	SRV [$\mathrm{cm\,s^{-1}}$]	J_0 [$\mathrm{fA\,cm^{-2}}$]	SRV [$\mathrm{cm\,s^{-1}}$]	J_0 [$\mathrm{fA\,cm^{-2}}$]	SRV [$\mathrm{cm\,s^{-1}}$]
Fully passivated	6 ± 3	12 ± 6	12 ± 5	1.5 ± 0.6	7 ± 3	14 ± 6
Fully pass. with Al-capping layer	6 ± 3	12 ± 6	12 ± 5	1.5 ± 0.6	260 ± 70	-
Metalized	> 50000	> 100000	> 800000	> 100000	850 ± 300	-

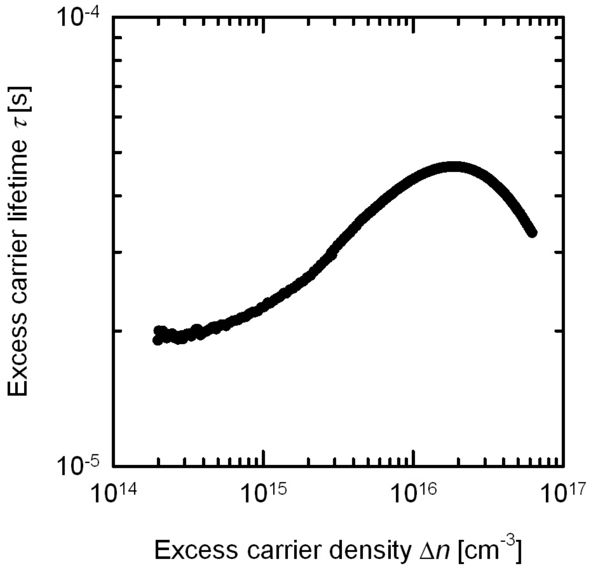

Figure 4.14: *Measurement of the injection dependent effective lifetime of an epitaxial layer of group High-Full-BSF-Texture. The sample is passivated by a stack of a* 10 nm *thick* $\mathrm{AlO_x}$ *layer for passivation and a* $\mathrm{SiN_x}$ *layer on both surfaces after porous silicon removal.*

5 Determination of resistances

Besides recombination, resistive losses are of major importance. We distinguish between the resistances in the silicon, at the silicon to metal interface, and in the metal. In order to obtain reliable values all resistances are measured on test samples processed in parallel to the solar cells.

5.1 Resistances measurements

5.1.1 Resistances in silicon

In the following the resistivity is measured under standard conditions, i.e. room temperature and no illumination. The four point probe method [8] is a commonly used method for measuring resistances of thin sheets. 4 contact points, which are rowed up in a line, are brought in contact with the silicon. The outer two contacts supply a current to the sample whereas the inner two contacts measure the voltage drop. The accuracy of the measurement is high due to the fact that only a very small current flows through the inner two probes, resulting in a small voltage drop in the inner probes themselves and at their contacts to the sample. From this voltage drop and the supplied current a sheet resistance R_{sheet} can be calculated by $R_{\text{sheet}} = k \times \frac{U}{I}$, where k is a geometric factor. For thin samples $k = \frac{\pi}{\ln 2}$. The specific resistivity ρ_{Si} can be calculated by multiplying the sheet resistance R_{sheet} by the thickness of the sheet d_{sheet}

$$\rho_{\text{Si}} = R_{\text{sheet}} \times d_{\text{sheet}}. \tag{5.1}$$

5.1.2 Resistances at the metal/silicon interface

The resistances at the metal/silicon interface are measured with the transfer-length-method (TLM) [9]. For this purpose test samples are processed in parallel to solar cells. The structure of the test samples is shown in Figure 5.1. Figure 5.1a shows the structure for the emitter contacts and Figure 5.1b shows the structure for the base contacts.

Two neighboring aluminum fingers are contacted and a current flows by an applied voltage. On its way from one finger to the other the current has to pass two times through the contact of the silicon/metal interface as well as through the silicon between the two fingers. The total measured resistance therefore is

$$R_{\text{measured}} = 2 \times R_{\text{C}} + R_{\text{Si}} = 2 \times R_{\text{C}} + \frac{R_{\text{sheet}}}{d_{\text{sheet}}} \times d_{\text{finger}}, \tag{5.2}$$

where d_{finger} is the distance between the edges of two neighboring fingers. The test structure has finger pairs with different distances between each other. The measurement is done

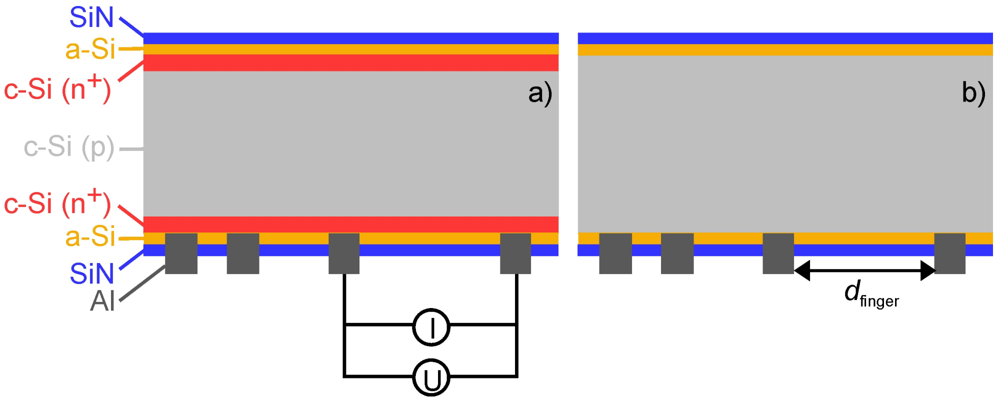

Figure 5.1: *Schematic cross section of the test samples for the TLM measurement. a) shows the emitter structure whereas b) shows the base structure. The voltage drop over every two neighboring fingers is measured by probes as shown in Figure a)*

between all neighboring fingers. Ideally, all data points lie on a straight line in accordance to Equation 5.2. The slope of this line yields the sheet resistance divided by the thickness of the sheet. By extrapolating this line to smaller distances the contact resistance R_C can be determined from the intersection with the y-axis.

Since the current flow through the contacts is not homogeneous, ρ_C cannot be calculated by dividing R_C by the contact area. A transfer length describing the current flow through the contact is introduced by the TLM method which cannot be determined analytical, but requires iteration using Newton's approximation procedure [9].

5.1.3 Resistances in metal

The resistivity in the metal is much lower than in the silicon. Nevertheless it is important to quantify it since the metal fingers have very small cross sections in our solar cells and therefore the resistance in the metal is not negligible. Test samples for the measurement of the aluminum resistivity are processed in parallel to the solar cells. An aluminum layer is evaporated on an insulating glass. Afterwards the sheet resistance is measured by the four point probe technique mentioned in Section 5.1.1. The resistivity is calculated by Equation 5.1.

5.2 Results of the resistances measurements

The measured resistivity of the evaporated aluminum of $2.65 \times 10^{-6}\,\Omega\,\mathrm{cm}$ is close to the literature value of bulk aluminum $2.82 \times 10^{-6}\,\Omega\,\mathrm{cm}$ [50].

The sheet resistances and the specific resistivities have been determined as described above. Since the emitter, contacts and aluminum fingers cover only a certain area fraction of the unit cell, as shown in Figure 4.6, each sheet resistance and specific resistivity is weighted with its surface coverage fraction $SCF = \frac{w_{\text{unit cell}}}{w_{\text{element}}}$ in the corresponding unit cell. This is also necessary for the later implementation in the network simulation since these are the actual resistances in the cell. Therefore, the resistances of each element (base, emitter, aluminum fingers and contacts) are divided by the surface coverage fraction

$$R_{\text{spice}} = \frac{R_{\text{measured}}}{SCF} = \frac{\rho_{\text{element}}}{d_{\text{element}}} \times \frac{w_{\text{unit cell}}}{w_{\text{element}}}, \tag{5.3}$$

where R_{measured} is the measured sheet or contact resistance, ρ_{element} is the specific resistivity of the element, d is the thickness (where $d = 1$ for contact resistivity) and w is the width. All area weighted results of the resistances R_{spice} are shown in Table 5.1.

If the base doping concentration decreases from $3 \times 10^{16}\,\text{cm}^{-3}$ in groups High to $1.5 \times 10^{15}\,\text{cm}^{-3}$ in groups Low, the base resistance decreases by a factor of about 18. Thus, the base sheet resistance increases by a factor of about 18. If the base doping concentration is high ($3 \times 10^{16}\,\text{cm}^{-3}$ for groups High), the base sheet resistances are in the same order as the emitter sheet resistances. If the base doping concentration at the silicon/metal interface decreases from $3 \times 10^{16}\,\text{cm}^{-3}$ in groups High to $1.5 \times 10^{15}\,\text{cm}^{-3}$ in groups Low, the base contact resistance increases by a factor of 10. The emitter contact resistances are about a factor of 10 (in groups High) and 100 (in groups Low) lower than the base contact resistances due to a highly doped surface. The resistances of the aluminum base fingers are higher than the resistances of the aluminum emitter fingers due to the lower width of the base finger as shown in Figure 4.6. Only group High-Full-Small (**II**) has the same resistances due to the same width of base and emitter finger. These resistances are input parameters for the unit cell simulations as well as for the network simulations as described in the following Chapter.

Table 5.1: *Resistances of all groups*

	High-Full (■)	High-Broken (▣)		Low-Full (▩)	Low-Broken (▣)		High-Full-Small (▮)	High-Full-BSF-Texture (■)
Unit cell	Contact	Contact	Passivated	Contact	Contact	Passivated	Contact	Contact
N_A [cm^{-3}]	3×10^{16}	3×10^{16}		1.5×10^{15}	1.5×10^{15}		3×10^{16}	3×10^{16}
$R_{\mathrm{Al\,base\,finger}}[\Omega/\Box]$	0.016	0.016		0.016	0.016		0.0063	0.016
$R_{\mathrm{base\,contacts}}[\Omega\,\mathrm{cm}^2]$	0.1	0.1	10^5	1	1	10^5	0.1	0.1
$R_{\mathrm{base}}[\Omega/\Box]$	170	170		3000	3000		170	70
$R_{\mathrm{emitter}}[\Omega/\Box]$	150	150		150	150		240	90
$R_{\mathrm{emitter\,contacts}}[\Omega\,\mathrm{cm}^2]$	0.01	0.01	10^5	0.01	0.01	10^5	0.01	0.1
$R_{\mathrm{Al\,emitter\,finger}}[\Omega/\Box]$	0.0025	0.0025		0.0025	0.0025		0.0063	0.0025

6 Device simulations

The characterization of the saturation current densities, as described in Chapter 4.3, and the resistances, as described in Chapter 5, yielding the input parameters for the simulation of the cells. In this work, a simulation of a two dimensional unit cell is combined with a series resistance network simulation in order to reproduce measured current voltage curves and quantum efficiencies. If simulations and measurements are in agreement, we considered all relevant impact factors on the solar cell power output. By this, we can analyze the impact of each loss mechanism by varying its magnitude in the simulation. We calculate the power density losses of the loss mechanism by free energy loss analysis. We use the results to realize an optimized solar cell process, which yields an increased conversion efficiency.

In the following sections we quantify the loss mechanisms. We first analyze the optical losses followed by the recombination and transport losses in the unit cell. Finally, the transport losses in the network are presented.

6.1 Optical simulations

The input parameters for the optical simulation in SUNRAYS [51] are the surface topologies (textured or planar) and the optical properties of the dielectric and metal layers covering them, which are taken from Palik [52] and Green [53]. The thickness of the layers is determined on test samples. Additionally, the AM1.5G spectrum is taken from Ref. [54], which is also implemented in the software. The output of the simulation is the reflection and absorption of each layer as well as the depth-dependent cumulative generation profile. Figure 6.1 shows the simulated reflection and absorption (a) of the first five groups and (b) of group High-Full-BSF-Texture (■). The absorption is divided in absorption in the monocrystalline bulk, in the passivation layer, and in the metal layer.

Figure 6.1a shows that in the first five groups the amorphous silicon passivation at the front side absorbs at wavelengths below 600 nm, whereas the metal at the rear side absorbs at wavelengths above 800 nm. Free carrier absorption can be neglected due to the low doping density of the emitter at the rear side. The absorption of the other layers is negligible and not shown in the figure. The measured reflection of a cell of group High-Full (■) is shown, which has the same layout and therefore the same reflection as the first five groups. It agrees well with the simulated reflection. Only at short wavelengths they show small deviations which leads to an equivalent photogenerated current density loss of less than $J_{\mathrm{SC,absorbed}} = 1\,\mathrm{mA\,cm^{-2}}$.

Figure 6.1b shows group High-Full-BSF-Texture (■) which has a $\mathrm{AlO_x}$ and $\mathrm{SiN_x}$ front side passivation with a negligible absorption, however, the metal at the rear also absorbs at long wavelengths. Free carrier absorption can also be neglected due to the low doping

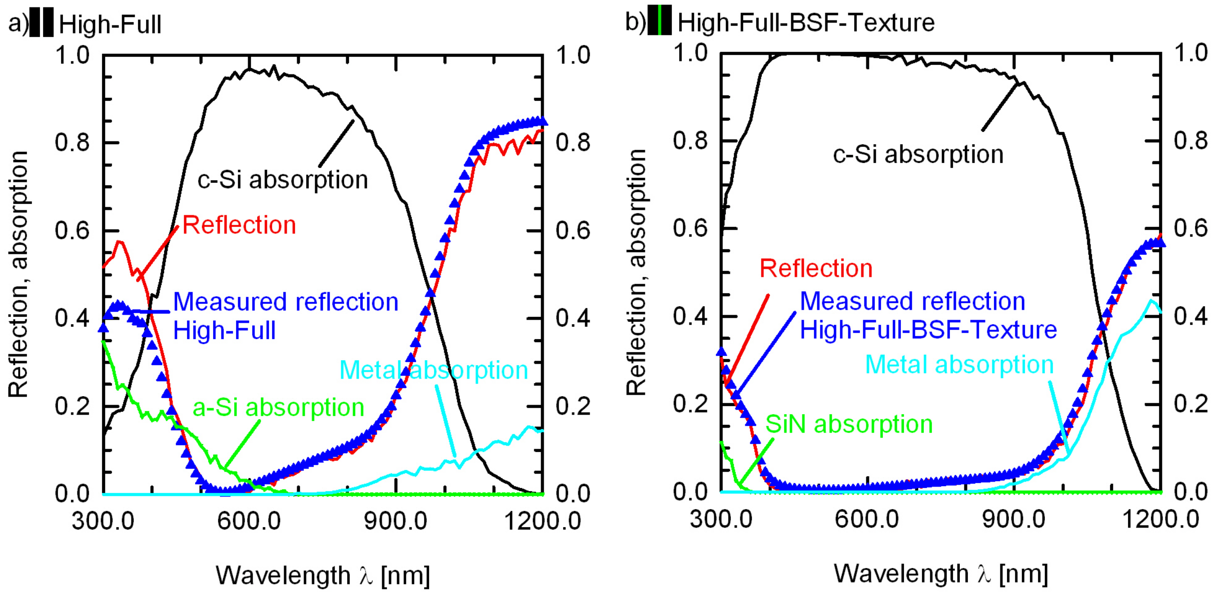

Figure 6.1: *The triangle symbols indicate the wavelength dependent measured reflection of the cells whereas the lines indicate the wavelength dependent simulated reflection of the cells and absorption of each layer covering the cells. (a) shows the data of group High-Full representing the first five groups whereas (b) shows the data of the group High-Full-BSF-Texture. The absorption in group High-Full is lower compared to group High-Full-BSF-Texture due to a highly absorbant a-Si front layer and to a high reflection due to the planar front surface.*

density of the emitter at the rear side. The absorption of the other layers is very low and not shown in the figure. The measured and the simulated reflection are in agreement. The reflection is much lower in this group compared to the first five groups due to the textured front surface.

Figure 6.2 shows the equivalent photogenerated current densities $J_{\mathrm{SC,absorbed}}(\lambda)$ of reflection and absorption of group High-Full (▮▮) representing the first five groups and the two regions of group High-Full-BSF-Texture (▮🟩). The incident light has an equivalent photogenerated current density of about $46\,\mathrm{mA\,cm^{-2}}$. In the first five groups the emitter region is only $2\,\mu$m thicker than the base region and thus the optical properties do not change significantly. Thus we only analyze the emitter region. A quarter of the total equivalent photogenerated current density is reflected due to the planar surface. The amorphous silicon layer at the front side and the metal absorb each 3 % of total equivalent photogenerated current density. The transmittance of the cell is zero, since a metal plate is placed behind the cell during the reflection measurement which is also present at the IQE and J-V measurements. $31.8\,\mathrm{mA\,cm^{-2}}$, which is 69 % of total equivalent photogenerated current density, is absorbed in the monocrystalline epitaxial layer creating free carriers.

The thickness of group High-Full-BSF-Texture (▮🟩) varies significantly from $36\,\mu$m to $45\,\mu$m in the base region. In both regions only 9 % to 8 % of the total equivalent photogenerated current density is reflected due to the textured front surface. The metal absorbs

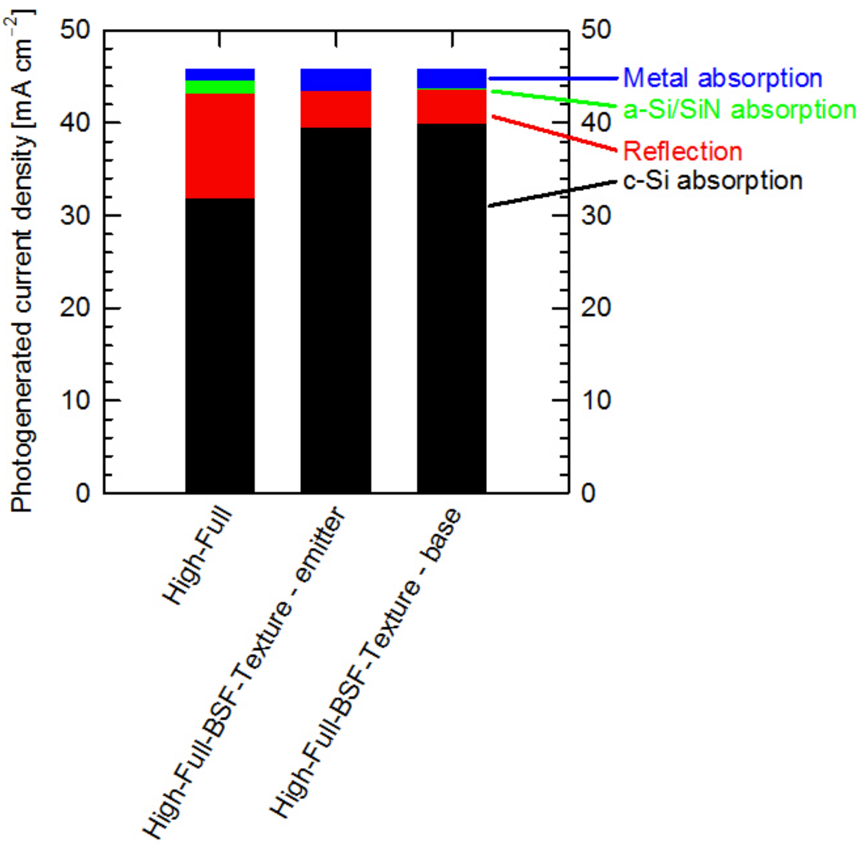

Figure 6.2: *Equivalent photogenerated current densities of reflection and absorption of group High-Full representing the first five groups and the two regions of the group High-Full-BSF-Texture. The transmittance of the cells is zero due to a metal plate behind the cells.*

5 % of the total equivalent photogenerated current density and the transmittance of the cell is also zero due to the metal plate behind the cell. In group High-Full-BSF-Texture (▮) 39 mA cm^{-2} (86 % of the total equivalent photogenerated current density) in the 36 μm thick region and 39.9 mA cm^{-2} (87 %) in the 45 μm thick region is absorbed in the monocrystalline epitaxial layer creating free carriers.

Figure 6.3 shows the cumulative generation profiles in the monocrystalline epitaxial layer in dependence of the distance to the front surface of the first five groups and of group High-Full-BSF-Texture (▮) in terms of an equivalent photogenerated current density. In the first five groups, shown in Figure 6.3a, the maximum generation rate is at the front surface and decreases with increasing distance to the front surface. 32 % of the total equivalent photogenerated current density of 31.5 mA cm^{-2} is already generated in the first 1 μm of the cell. In group High-Full-BSF-Texture (▮), shown in Figure 6.3b, the generation rate also decreases with increasing distance to the front surface. The total $J_{\mathrm{SC,absorbed}}$ increases to 39.4 mA cm^{-2} in the emitter region and to 39.9 mA cm^{-2} in the base region compared to the first five groups due to an enhanced light trapping by the textured front surface.

In summary, the total optical losses are 31 % in the first five groups whereas group High-Full-BSF-Texture (▮) shows only losses of 13 % of the total $J_{\mathrm{SC,absorbed}}$. The generation profiles are one input parameter in the unit cell simulation.

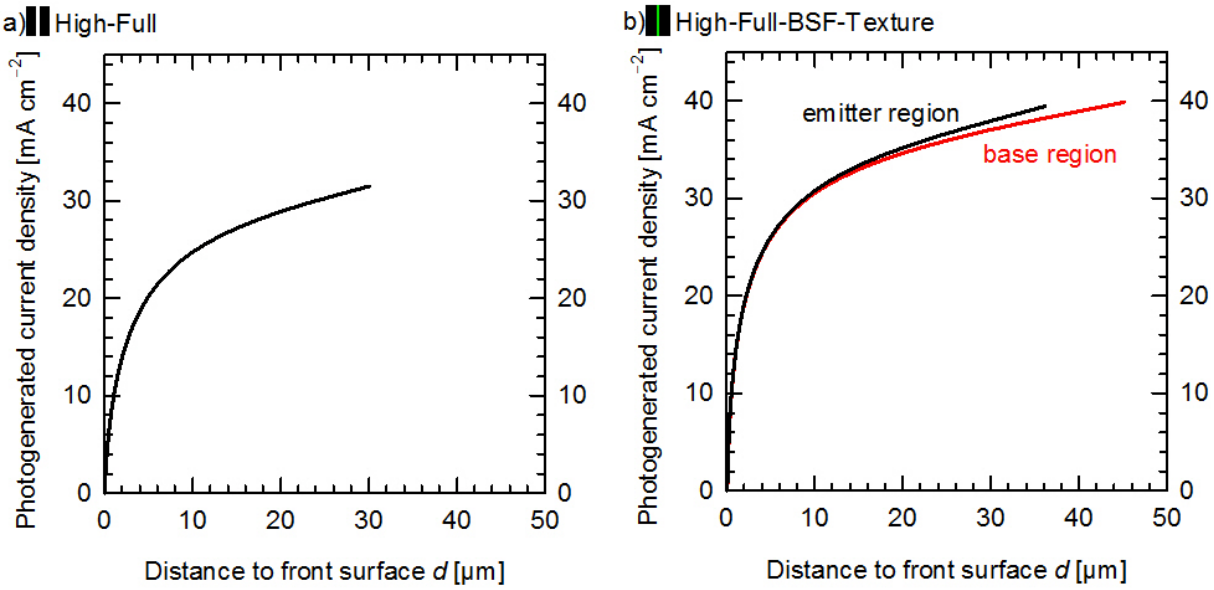

Figure 6.3: *Cumulative generation profiles in dependence of the distance to the front surface. The left graph shows the generation of group High-Full representing the first five groups whereas the right graph shows the data of the group High-Full-BSF-Texture. Due to the* 9 µm *difference of the emitter and the base thickness in the cell we use two different generation profiles.*

6.2 Unit cell simulation

6.2.1 Theory of used simulation models and methods

The unit cell shown in Figure 4.6 is simulated by a finite element simulation with the conductive boundary model (CoBo) [12] that is implemented by using COMSOL [55]. Highly-doped regions at the surface like emitters and back surface fields are treated as one-dimensional conductive boundaries. The conductivity and saturation current density characterize the boundaries. The CoBo model solves the fully coupled set of semiconductor equations for the quasi-Fermi potential of the holes E_{Fp}, the quasi-Fermi potential of the electrons E_{Fn}, and for the electrostatic potential φ in the volume of the cell. The Fermi potentials are treated in units of volts and are defined as

$$\begin{aligned} \varphi_{\mathrm{Fn}} &= q^{-1} \times E_{\mathrm{Fn}} \text{ for electrons and} \\ \varphi_{\mathrm{Fp}} &= q^{-1} \times E_{\mathrm{Fp}} \text{ for holes.} \end{aligned} \tag{6.1}$$

The gradients of the quasi-Fermi potentials drive the current densities

$$\begin{aligned}\vec{J}_{\mathrm{Qn}} &= \sigma_{\mathrm{n}} \times \vec{\nabla}\varphi_{\mathrm{Fn}} \text{ for electrons and}\\ \vec{J}_{\mathrm{Qp}} &= \sigma_{\mathrm{p}} \times \vec{\nabla}\varphi_{\mathrm{Fp}} \text{ for holes,}\end{aligned} \tag{6.2}$$

where σ_{n} is the electron conductivity and σ_{p} is the hole conductivity as shown in Equation 4.24. In steady state the continuity Equation 4.25 simplifies to

$$\begin{aligned}-\frac{1}{q}\vec{\nabla}\vec{J}_{\mathrm{n}} &= G(t) - U(t) \text{ for electrons and}\\ \frac{1}{q}\vec{\nabla}\vec{J}_{\mathrm{p}} &= G(t) - U(t) \text{ for holes.}\end{aligned} \tag{6.3}$$

By combining Equation 6.2 with Equation 6.3 the following two equations arise and have to be solved in the base:

$$\begin{aligned}-\frac{1}{q} \times \vec{\nabla}\left(\sigma_{\mathrm{n}} \times \vec{\nabla}\varphi_{\mathrm{Fn}}\right) &= G(t) - U(t) \text{ for electrons and}\\ \frac{1}{q} \times \vec{\nabla}\left(\sigma_{\mathrm{p}} \times \vec{\nabla}\varphi_{\mathrm{Fp}}\right) &= G(t) - U(t) \text{ for holes.}\end{aligned} \tag{6.4}$$

The left and right edges in Figure 4.6 on page 41 are symmetry planes. The boundary conditions of the other surfaces are described in more detail in [12]. For these surfaces the measured diode saturation current densities and measured sheet resistances are used. The generation profile is determined by the ray tracer SUNRAYS [51]. This profile is also an input parameter for the CoBo simulation. All the input parameters are handled by the user interface CoBoGUI [56] which communicates with the software COMSOL [55]. The CoBoGUI extracts a light current-voltage curve and local Fermi potentials and current densities. The free energy loss analysis is used to calculate the power loss per area of each recombination path and transport mechanism as described in the next Section 6.2.2. Since doped regions like emitters are not spatially resolved only a few mesh points are required, which keeps the duration of the simulation short.

However, this two dimensional unit cell simulation does not account for the contact resistances of the silicon/metal interface and for the series resistances perpendicular to the two-dimensional CoBo-simulated unit cells in parallel to the fingers.

6.2.2 Free energy loss analysis

Free energy loss analysis (FELA) [10] is used to calculate the power loss in the solar cell by using the results of the simulations. FELA is a way to calculate all losses of a solar cell in terms of power per area. It allows for calculating both recombination and transport losses in power per area. Therefore the losses can be compared directly with each other at any terminal voltage and especially at the maximum power point.

The FELA considers electrical power as a rate of free enthalpy $\dot{F}$ since it is free of entropy. The rate of free enthalpy is $\dot{F} = J_{\mathrm{Q}} \times U$, where J_{Q} is the terminal charge current and U the terminal voltage. To analyze the local free energy of the cell, we have to analyze the local charge current densities, but also the local voltage, which is equal to the splitting of the quasi-Fermi levels. The charge current densities of electrons and holes can be calculated as follows:

$$\vec{j}_{\mathrm{Q,e}} = q^{-1} \times \sigma_{\mathrm{e}} \times \nabla E_{\mathrm{FC}} \tag{6.5}$$

$$\vec{j}_{\mathrm{Q,h}} = q^{-1} \times \sigma_{\mathrm{h}} \times \nabla E_{\mathrm{FV}} \tag{6.6}$$

where σ_{e} and σ_{h} are the electron and hole conductivities. The free energy of the electrons equals the electron quasi-Fermi level E_{FC} in the conduction band whereas the free energy of holes equals the negative hole quasi-Fermi level $-E_{\mathrm{FV}}$ in the valence band.

The current density of free energy carried by the electrons through the electron contact is

$$\vec{j}_{\mathrm{F,e}} = E_{\mathrm{FC}} \times \left(\vec{j}_{\mathrm{Q,e}}/(-q) - \vec{j}_{\mathrm{Q,h}}/(+q)\right) = -E_{\mathrm{FC}} \times \left(\vec{j}_{\mathrm{Q,e}} + \vec{j}_{\mathrm{Q,h}}\right)/q \tag{6.7}$$

and the current density of free energy carried by the holes through the hole contact is

$$\vec{j}_{\mathrm{F,h}} = -E_{\mathrm{FV}} \times \left(\vec{j}_{\mathrm{Q,h}}/(+q) - \vec{j}_{\mathrm{Q,e}}/(-q)\right) = -E_{\mathrm{FV}} \times \left(\vec{j}_{\mathrm{Q,e}} + \vec{j}_{\mathrm{Q,h}}\right)/q \tag{6.8}$$

The current densities $\vec{j}_{\mathrm{F,e}}$ and $vecj_{\mathrm{F,h}}$ in Equations 6.7 and 6.8 account for the recombination at the contacts. The flux of free energy through the electron contact and through the hole contact is

$$\dot{F} = U \times J_{\mathrm{Q}} = \int_{\delta \mathrm{V_e}} d\vec{A}\, \vec{j}_{\mathrm{F,e}} + \int_{\delta \mathrm{V_h}} d\vec{A}\, \vec{j}_{\mathrm{F,h}}, \tag{6.9}$$

where $d\vec{A}$ is the differential area vector normal to the cell surface of the cell volume $\delta \mathrm{V_e}$. Inserting Equations 6.7 and 6.8 in Equation 6.9, extending the integrals to the whole surface and considering the fact, that the total current $\vec{j}_{\mathrm{Q,e}}+\vec{j}_{\mathrm{Q,h}}$ vanishes at non-contacted surfaces, we end up with the free energies of all losses in the cell. The free energy density rate by recombination in the base is

$$\dot{f}_{\mathrm{b}} = A^{-1} \int_V dV \left(E_{\mathrm{FC}} - E_{\mathrm{FV}}\right) r, \tag{6.10}$$

where A is the cell area and r is the local recombination rate. The free energy density rate by recombination at the surface is

$$\dot{f}_{\mathrm{s}} = A^{-1} \int_{\delta V} d\vec{A}\, \vec{j}_{\mathrm{Q}}/q \left(E_{\mathrm{FC}} - E_{\mathrm{FV}}\right). \tag{6.11}$$

The free energy density rate by transport of electrons is

$$\dot{f}_{\mathrm{te}} = A^{-1} \int_V dV |\vec{j}_{\mathrm{Q,e}}|^2/\sigma_{\mathrm{e}} \tag{6.12}$$

and the free energy density rate by transport of holes is

$$\dot{f}_{\mathrm{th}} = A^{-1} \int_V dV |\vec{j}_{\mathrm{Q,h}}|^2/\sigma_{\mathrm{h}}. \tag{6.13}$$

The output parameters of our unit cell simulation are local current flows, conductivities and Fermi-levels. With these parameters the free energy density loss rate $\dot{f}_i$ of every single part of the cell, such as recombination in the base ($i = \mathrm{v}$) and at the surfaces ($i = \mathrm{s}$) or transport of holes ($i = \mathrm{th}$) and electrons ($i = \mathrm{te}$) in the base and conductive sheets, can be calculated in power per area. Therefore all power losses at the maximum power point of the cell can be compared directly.

6.2.3 Results of unit cell simulations

Figure 6.4 shows the main power density losses of the passivated and contacted unit cells of all investigated cell groups. The simulation results are calculated without applying a network simulation.

The power density loss due to the transport of electrons depends only slightly on the group or on the unit cell. It decreases the generated power density of all unit cells by $6 - 10\,\mathrm{W\,m^{-2}}$. It is a relevant power loss in all unit cells of group High-Full (▮▮), High-Broken (◘) and High-Full-BSF-Texture (▮🟩). The free energy transport loss of electrons is a quadratic function of the electron quasi-Fermi level gradient. The difference between the electron quasi-Fermi level in the base and at the surfaces determines the gradient of the electron quasi-Fermi level. Both quasi-Fermi levels decrease with increased recombination. To reduce the gradient, the recombination in the region with the highest recombination has to be reduced.

Group High-Full (▮▮) and High-Broken (◘)

Now groups High-Full (▮▮) and High-Broken (◘) with a base doping density of $3 \times 10^{16}\,\mathrm{cm^{-3}}$ are considered. Group High-Full (▮▮) has only contacted unit cells whereas group High-Broken (◘) consists of both contacted as well as passivated unit cells. The contacted unit cells of group High-Full (▮▮) and group High-Broken (◘) are identical. In the passivated unit cells the current is extracted at the same position as in the contacted region but the saturation current density is the same as in the passivated unit cells. We call these contacts passivated contacts.

The major power density loss of the contacted unit cells is the contact recombination causing $19\,\mathrm{W\,m^{-2}}$ power density loss. The power density loss by SRH recombination is $7\,\mathrm{W\,m^{-2}}$. All other power losses in the contacted unit cells are less than 15 % of the sum of all unit cell power losses.

In the passivated group High-Broken (◘) the SRH recombination is the biggest power density loss of $12\,\mathrm{W\,m^{-2}}$. This is a slight increase of SRH recombination compared to the contacted unit cell, because in the contacted unit cell a part of the carriers diffuse to and recombine at the contact instead of recombining in the base. All other power losses in the passivated unit cell of group High-Broken (◘) are less than 25 % of the sum of all unit cell power losses.

Group Low-Full (▯▯) and Low-Broken (▯)

Groups Low-Full (▯▯) and Low-Broken (▯) have a lower base doping density of $1.5 \times 10^{15}\,\mathrm{cm^{-3}}$.

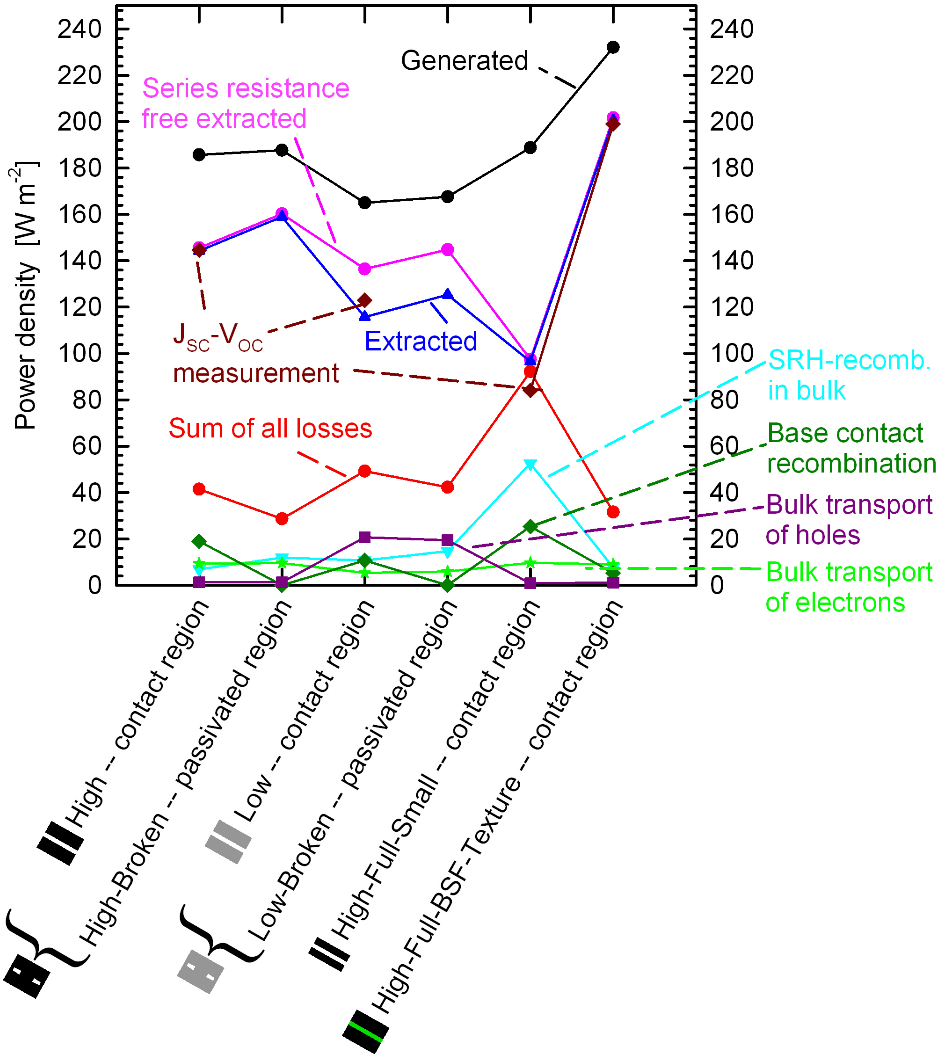

Figure 6.4: *Power densities of the unit cells of all cell groups. The generated power densities (black) as well as the extracted power densities (blue) are depicted. Additionally the main power density losses and the sum of all power density losses (red) of the unit cells are shown. The series resistance-free simulated (pink) and the series resistance-free measured power densities (dark red) are in agreement. The parameter variations of the groups are listed in Table 4.1 and Table 4.2*

Group Low-Full (▮▮) has only contacted unit cells whereas group Low-Broken (▣) has contacted and passivated unit cells. The contacted unit cells of group Low-Full (▮▮) and group Low-Broken (▣) are identical. The power density losses of groups Low-Full (▮▮) and Low-Broken (▣) are dominated by the transport loss of holes, representing 42 % and 46 % respectively of all unit cell losses. This loss is due to the low doping density and the resulting high base resistance for the majority carriers. SRH recombination in the bulk is the second highest power density loss of group Low-Full (▮▮) and group Low-Broken (▣). The SRH recombination causes a power density loss of 15 W m^{-2} in the passivated unit cell, which is 35 % of the total unit cell power density losses. In the contacted unit cell SRH recombination causes a power density loss of 11 W m^{-2}, which is 22 % of the total unit cell power density losses. The recombination at the base contact causes 11 W m^{-2}, which is 22 % of the total unit cell power density losses in group Low-Full (▮▮). All other losses in the unit cells of group Low-Full (▮▮) and Low-Broken (▣) are less than 5 % of the sum of all unit cell losses.

Group High-Full-Small (▮▮)

Group High-Full-Small (▮▮) has only contacted unit cells. The most limiting loss in this group is SRH recombination causing a power density loss of 53 W m^{-2}. This is due to a low bulk lifetime of 3 μs, which corresponds to a small diffusion length, as shown in Table 7.1, in combination with a wide base finger. The diffusion length of the minority carries is less than a third of the width of the unit cell base finger. This means that many minority carries recombine in the base before they are collected at the emitter finger. This fact is known as electrical shading and is clearly seen by the large decrease in the EL-signal in Section 7.1 and the low IQE in Section 3.2. A large part of the cell area does not contribute to the collection of the minority carriers. Therefore this loss has the highest impact on the short-circuit current density which is only $J_{\mathrm{SC}} = 18.8\,\mathrm{mA\,cm^{-2}}$. The second highest loss in this group is the recombination at the base contact causing a power density loss of 25 W m^{-2}. This loss is in the same order of magnitude as the loss at the base contact in the contact groups of group High-Full (▮▮) and High-Broken (▣). This is expected, since the unit cells are very similar in this region. All other losses in the unit cell of group High-Full-Small (▮▮) are less than 15 % of the sum of all unit cell losses.

Group High-Full-BSF-Texture (▮▮)

Group High-Full-BSF-Texture (▮▮) has only contacted unit cells. In this group the loss by electron transport in the base is the highest among all losses in this unit cell, causing a power density loss of 9.1 W m^{-2}. The second biggest loss is SRH recombination, however it causes only 7.7 W m^{-2} power density loss due to the high lifetime of 20 μs shown in Section 4.1.1. The recombination at the base contact is only 5.3 W m^{-2} power density loss due to the BSF. The next biggest losses are recombination at the passivated BSF, causing 3.6 W m^{-2} power density loss, and recombination at the passivated emitter, causing 2.6 W m^{-2} power density loss. All other losses in the unit cell of group High-Full-BSF-Texture are less than 12 % of the sum of all unit cell losses. Due to the textured front surface the generated power density is 232 W m^{-2} in this group. The recombination in the bulk and at the surfaces is kept small by a BSF and well passivated surfaces. The recombination in the bulk and at the interfaces only causes a power density loss of 32 W m^{-2} and therefore the extracted power density of the unit cell is 200 W m^{-2}, which corresponds to an efficiency of 20 %.

For the comparison of the simulated and measured power density losses the series resistance-free extracted power densities of simulations and experiments are plotted. The measured series resistance-free power density is $p\eta$ multiplied by the wavelength integrated irradiation. Since the total cell area is measured, the extracted free power density is an average power density over the total cell area. Therefore only measurement results of cells which are homogeneous over the total area can be compared to unit cell simulations. These cells are cells which only consist of contacted unit cells, i.e. High-Full (▮▮), Low-Full (▮▮), High-Full-Small (❙❙) and High-Full-BSF-Texture (▮▮). The simulated series resistance-free power density is calculated by adding the transport losses of the majorities to the extracted power density. This agrees with the simulated power densities of the shifted J_{SC}-V_{OC} curves. The simulated and the measured power densities agree within an uncertainty of 1.6 % in group High-Full (▮▮), 7.1 % in group Low-Full (▮▮), 16 % in group High-Full-Small (❙❙) and 1.3 % in group High-Full-BSF-Texture (▮▮). The deviations in groups Low-Full (▮▮) and group High-Full-Small (❙❙) are mainly due to non ideal recombination in the real cell, which we do not consider in the simulations.

As mentioned in Figure 1.1, the CoBo simulation yields local recombination parameters and current densities. Figure 6.5 shows a cross section of every unit cell. The color quantifies power density losses due to SRH recombination whereas the black lines are the minority carrier current paths. The minority carrier paths start very close to the top of the cells. Only a negligible part of them end at the front surface whereas most of them end in the emitter region (marked in red) where they are conducted to the emitter contact if they do not recombine on their way, as shown in Figure 6.4. Some of the minority carrier paths end at the base contact or the base finger, where the carriers are lost by recombination and do not contribute to the extracted power of the cell. This effect is also called electrical shading [20]. This means that all electron hole pairs which are generated in the region where the paths end in the base contact are lost completely by recombination. This area is also marked by a black line on top of the unit cells. The range of SRH recombination is kept constant for the first five groups shown in Figure 6.5a to e for better comparability. Group High-Full-Small (❙❙) has the highest SRH recombination and is therefore plotted on a wider range.

Groups High-Full (▮▮) and High-Broken (◼) in Figure 6.5a and b

We first analyze the minority carrier current paths of the contacted unit cells. Current paths which start left of the center between the emitter edge and the base contact edge all end at the emitter marked in red. Current paths which start right of the center between the emitter edge and the base contact edge all end at the base contact. This divides the cell into two parts. The minority carriers of the left part contribute to the current, whereas the minority carriers of the right part do not contribute to the current. This means that effectively the power output of the right part of the unit cell, which is 12 % of the total cell area, is lost by recombination. The sum of the power densities of the base contact recombination ($19\,\mathrm{W\,m^{-2}}$) and of the Shockley-Read-Hall (SRH) recombination in this electrical shading area ($1.6\,\mathrm{W\,m^{-2}}$) is $20.6\,\mathrm{W\,m^{-2}}$, which is 11 % of the generated power density. This is close to the area weighted current loss of 12 %. The SRH recombination increases with increasing distance to the emitter due to the increase of the minority carrier concentration. The SRH recombination also increases with increasing distance to the base contact since

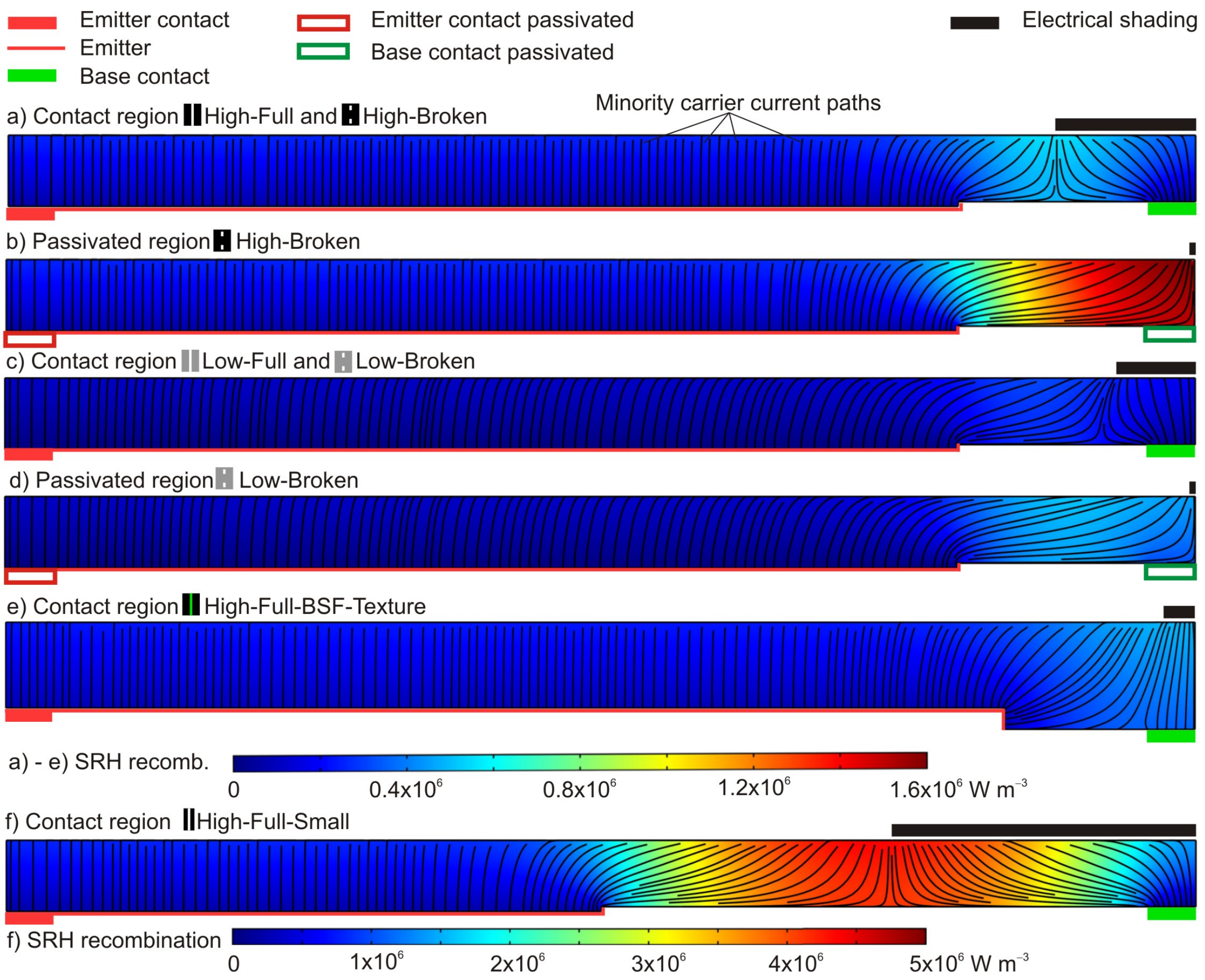

Figure 6.5: *SRH recombination and minority carrier current paths of every unit cell. The first five groups are plotted on the same range for comparison. Group High-Full-Small has the highest SRH recombination and therefore uses a wider range. The minority carrier current paths are plotted by black lines. The region of the contacts, passivated contacts, the region of the emitter as well as the region of the electrical shading is shown for every cell.*

the carrier concentration decreases with decreasing distance to the base contact due to the high recombination at the base contact.

Secondly the minority carrier paths of the passivated unit cell of High-Broken (■) are investigated. In the passivated unit cell nearly every current path ends at the emitter. The SRH recombination increases with increasing distance to the emitter due to an increase in carrier concentration. Since the carrier concentrations are not decreased by base contact recombination the absolute value of the SRH recombination also increases compared to the contacted unit cell.

Groups Low in Figure 6.5c and d

Third we analyze the minority carrier paths of group Low-Full (▮▮) and Low-Broken (▮). At the contacted unit cells of group Low-Full and Low-Broken more minority carrier paths end at the emitter and not at the base contact compared to group High. This is due to a decreasing electron quasi-Fermi-level with increasing distance to the base contact. This decrease is caused by the lower doping concentration compared to group High. The electrical shading affects about 6.7 % of the front side of the contacted region of group Low where most of the carriers are generated. The sum of the power densities of the base contact recombination ($10.7\,\mathrm{W\,m^{-2}}$) and of the Shockley-Read-Hall (SRH) recombination in this electrical shading area ($0.8\,\mathrm{W\,m^{-2}}$) is $11.5\,\mathrm{W\,m^{-2}}$, which is 7.0 % of the generated power density. This is nearly the same value as the area weighted current loss of 6.7 %. The SRH recombination in the unit cells of groups Low is higher than in groups High due to the higher minority carrier concentrations. The passivated unit cell shows similar minority carrier paths to the passivated unit cell of group High-Broken (▮). The higher SRH recombination compared to group High-Broken (▮) is again due to the higher minority carrier concentration in group Low-Broken (▮).

Group High-Full-BSF-Texture (▮▮) in Figure 6.5e

Nearly all of the minority carrier paths of group High-Full-BSF-Texture (▮▮) end at the emitter. Only a small fraction ends at the base contact. This is due to a BSF beneath the base contact, which reduces recombination. The width of the base finger is also smaller ($80\,\mu\mathrm{m}$) than in the other groups, so that the distance to the emitter is shorter for minority carriers. The electrical shading affects about 2.3 % of the front side of the contacted region of group High-Full-BSF-Texture (▮▮) where most of the carriers are generated. The sum of power densities of the base contact recombination ($5.3\,\mathrm{W\,m^{-2}}$) and of the Shockley-Read-Hall (SRH) recombination in this electrical shading area ($0.5\,\mathrm{W\,m^{-2}}$) is $5.8\,\mathrm{W\,m^{-2}}$, which is 2.5 % of the generated power density. This is nearly the same value as the area weighted current loss of 2.3 %. The minority carrier diffusion length is $220\,\mu\mathrm{m}$ and thus the SRH recombination is lower in this particular epitaxial layer compared to the other groups due to quality variance. These facts lead to the highest efficiency of 20 % in this unit cell.

Group High-Full-Small (▮▮) in Figure 6.5f

Finally the minority carrier paths of group High-Full-Small (▮▮) are investigated. This contacted unit cell shows similar qualitative current paths as group High-Full (▮▮). In this unit cell the center between the emitter edge and the base contact is also the line which separates the minority carrier paths which end at the emitter and which end at the base contact. Due to the smaller emitter finger of $500\,\mu\mathrm{m}$ and the wider base finger of $500\,\mu\mathrm{m}$, the area where the minority carrier paths end at the base contact and recombine is 25 % of the total area in this unit cell, which is more than two times of the loss area of the unit cell of group High-Full (▮▮). The sum of the power densities of the base contact recombination ($25\,\mathrm{W\,m^{-2}}$) and of the Shockley-Read-Hall (SRH) recombination in this electrical shading area ($21.6\,\mathrm{W\,m^{-2}}$) is $46.6\,\mathrm{W\,m^{-2}}$, which is 25 % of the generated power density. This is the same value as the area weighted current loss of 25 %. This large influence of the electrical shading effect is the reason for the low short circuit current density of $J_{\mathrm{SC}} = 18.8\,\mathrm{mA\,cm^{-2}}$

in this group. The SRH recombination in this group is the highest of all groups investigated. This is due to a low minority carrier diffusion length of 75 μm combined with long distances of up to 250 μm to the emitter fingers. The scale of the SRH recombination is changed due to much higher SRH recombination in this group.

We describe all losses in the unit cells with the help of the finite element simulations. One of the highest power losses is SRH recombination caused by the low bulk lifetime of the epitaxial layers due to crystal defects. Another significant power loss is recombination at the base contact. This recombination is reduced by a BSF to 5.3 W m^{-2} in group High-Full-BSF-Texture (▮). A lowly doped base of 1.5×10^{15} cm^{-3} induces high transport losses of about 20 W m^{-2} for the majority carriers. Therefore a highly doped base of 3×10^{16} cm^{-3} is used in our optimized cell design in group High-Full-BSF-Texture (▮), reducing the power density loss caused by transport of majority carriers to 1 W m^{-2}.

6.3 Resistance network simulation

The last section determined all recombination losses in the unit cell. This section shows how a series resistance network simulation includes the series resistances which are not considered by the two dimensional unit cell simulation [57]. The geometry of the solar cell is schematically shown in Figure 2.4. The busbar of the solar cell is 2.5 mm wide in the small cells (Groups Low and group High-Full-BSF-Texture (▮)) whereas is is 5 mm wide in the large area cells (Groups High-Full (▮), High-Broken (▮) and group High-Full-Small (▮)). It thus has a low series resistance and introduces no significant resistive losses. Consequently we neglect the busbar in the network simulation and the simulation simplifies to a unit cell finger which is divided into unit cells. Figure 6.6 schematically shows the network of series resistances.

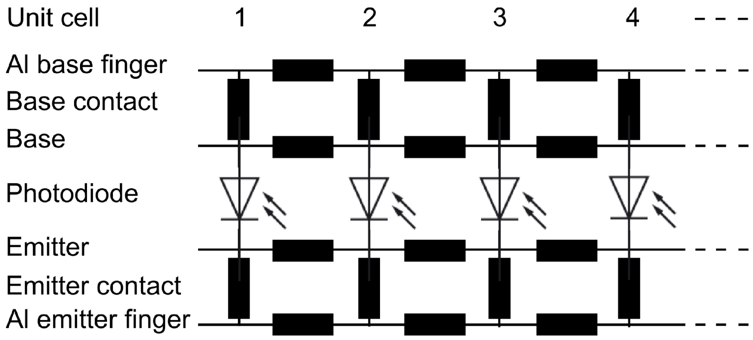

Figure 6.6: *Series resistance network of a unit cell finger consisting of single unit cells. One unit cell consists of a single J V-curve between base and emitter and series resistances which interconnect the J-V curves. The values of the contact resistances of each unit cell depend on whether the unit cell is passivated or contacted.*

The light J-V characteristics as simulated in the first step using the CoBoGUI is used to represent the photodiode between the emitter and the base. The J-V curve and every resistor of each unit cell is individual and might change along the finger. Figure 6.7a shows a schematic top-view prior to the aluminum deposition. The rear surface of the unit cell consists of a base and an emitter finger. The white lines are the continuous full line contact openings. In this configuration every unit cell has the same J-V curve and the same resistor. A second structure has a contact area that is decreased by a factor of three. This is achieved by interrupting the contact lines as shown in Figure 6.7b and is called broken line. The unit cells with and without contacts show different J-V characteristics and contact resistances. The recombination in the contacted unit cells is higher and the resistance to the metal finger is much lower than in the passivated unit cells. Figure 6.7c shows the unit cells that are used in the resistance network simulation. The calculation is done by the user interface SpiceGUI [58] which uses the software LTSpice [57].

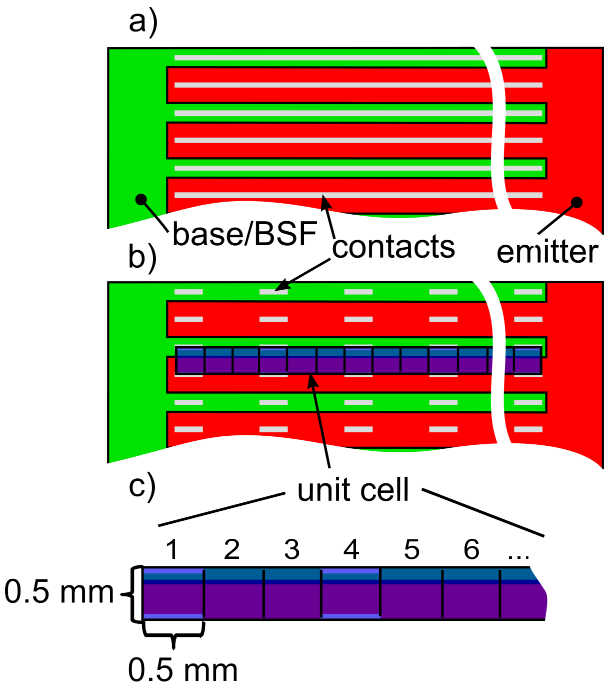

Figure 6.7: *Schematic top view of the local contact openings prior to the aluminum deposition. (a) Configuration with full line contact openings. (b) Configuration with broken line contact openings. (c) Definition of the unit cells for the network simulation. Each unit cell is marked with a box.*

Figure 6.8 shows a power density analysis of the series resistance losses of the network. The power density losses are evaluated at the voltage of the maximum power point of the light J-V curve. The series resistance losses in the unit cells are already implemented in the CoBo simulations and therefore do not appear in this loss analysis.

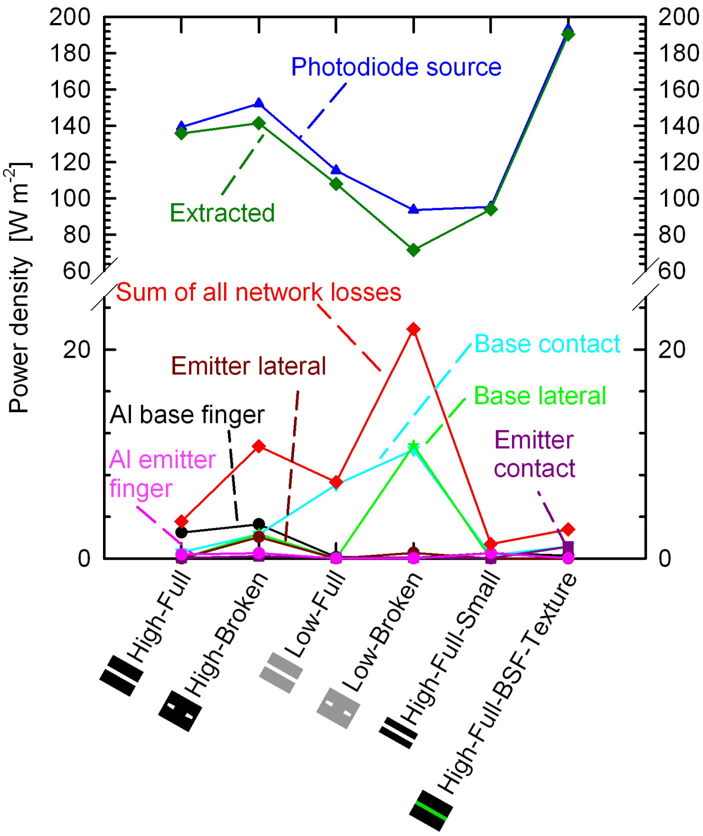

Figure 6.8: *Power density analysis of the series resistance losses of the network of the six investigated cell groups. The power density losses are evaluated at the maximum power point of the resulting J-V curve.*

Group High-Full (▮▮) shows a power density loss of 3.6 W m^{-2} which is mainly limited by the series resistance of the aluminum base finger. This finger is 88 mm long and has a small cross section of only 0.825×10^{-3} mm^2, leading to a power density loss of 2.5 W m^{-2}.

Group High-Broken (▣) has a power density loss of 10.8 W m^{-2} which is also limited by the series resistance of the aluminum base finger (3.3 W m^{-2}). In contrast to group High-Full (▮▮), group High-Broken (▣) also loses nearly the same power density by lateral emitter and base resistance as well as base contact resistance. This is due to the long distance the majority carriers have to diffuse to the contact pads whereas majorities in group High-Full (▮▮) have a shorter distance to the contact lines.

Group Low-Full (▯▯) suffers from a power density loss of 7.3 W m^{-2} which is mainly limited by the huge base contact resistance of 1 Ω cm^2. The other power losses are very small. The power loss of the aluminum base finger, which limits group High-Full (▮▮), is only 0.15 W m^{-2} for this solar cell due to the small cell area of 5.2 cm^2.

Group Low-Broken (▢) has the biggest power density losses of all groups due to a high base contact resistance of 1 Ω cm^2 and the high base sheet resistance of 3000 Ω/□. The distance of the majority carriers through the base to the base contact is much longer in comparison to group Low-Full (▮▮) causing a power density loss in the whole network of $22\,\mathrm{W\,m^{-2}}$.

Group High-Full-Small (▮▮) shows a power density loss of only $1.4\,\mathrm{W\,m^{-2}}$. The resistances of the emitter and the base fingers contribute each $0.5\,\mathrm{W\,m^{-2}}$ to the sum of all network losses. In this case the width of the base and the emitter aluminum finger are equal. The contact resistance at the base contact causes $0.3\,\mathrm{W\,m^{-2}}$ power density loss.

Group High-Full-BSF-Texture (▮▮) has a power density loss of $2.8\,\mathrm{W\,m^{-2}}$. These network losses are almost exclusively due to the contact resistances, which cause $2.3\,\mathrm{W\,m^{-2}}$ power density loss.

The maximum power point voltage of the unit cells differs from the maximum power point voltage of the resulting J-V curves after the network simulation. Since the evaluation of the power density losses caused by the network is done at the maximum power point voltage of the resulting J-V curve, an addition of the power density losses would not result in the power density of the unit cells. For a prediction of an extracted power density with different resistivity values it is not possible to add or subtract evaluated power densities due to a change of the maximum power point voltage but a new network simulation has to be done.

In conclusion, the power density loss analysis of the network simulation determines the limiting series resistance losses at the maximum power point of the solar cells in each group. The limiting resistance losses are induced by long aluminum fingers, which cause up to $2.5\,\mathrm{W\,m^{-2}}$ power density loss in group High-Full (▮▮) and $3.3\,\mathrm{W\,m^{-2}}$ power density loss in group High-Broken (◘) as well as by high contact resistances, especially at interfaces of lowly doped silicon to aluminum, of $1\,\Omega\,\mathrm{cm}^2$, leading to $22\,\mathrm{W\,m^{-2}}$ power density loss in combination with a high resistance in the base of $9\,\Omega\,\mathrm{cm}$.

6.4 Comparison of cell simulations and measurements

Figure 6.9 shows four J-V curves for every group: The black curve shows the measured light J-V curve and the violet curve shows the measured J_{SC}-V_{OC} curve. The other two J-V curves are simulated. The green J-V curve is simulated by combining CoBo simulations of the unit cells and series resistance network simulations, and the red J-V curve is simulated by combining measured J_{SC}-V_{OC} curves and series resistance network simulations. The measured J_{SC}-V_{OC} curves show pFFs of 72 % to 84 % as compared to FFs of 45 % to 80 % for the light J-V curves. This difference is fully accounted for by combining the measured J_{SC}-V_{OC} curve and series resistance network simulations using the resistances listed in Table 5.1. This means that the transport losses are well understood in all groups.

The simulated curves combining CoBo simulations of the unit cells and series resistance network simulations show small deviations from the measured light J-V curves. Nevertheless these deviations are relatively small considering that all cell simulations in this work contain no free parameters. The difference in groups High-Full (▮▮), High-Broken (◘), High-Full-Small (▮▮), and High-Full-BSF-Texture (▮▮) is mainly due to non ideal recombination in the real solar cells, which is not taken into account in the CoBo simulations. The mea-

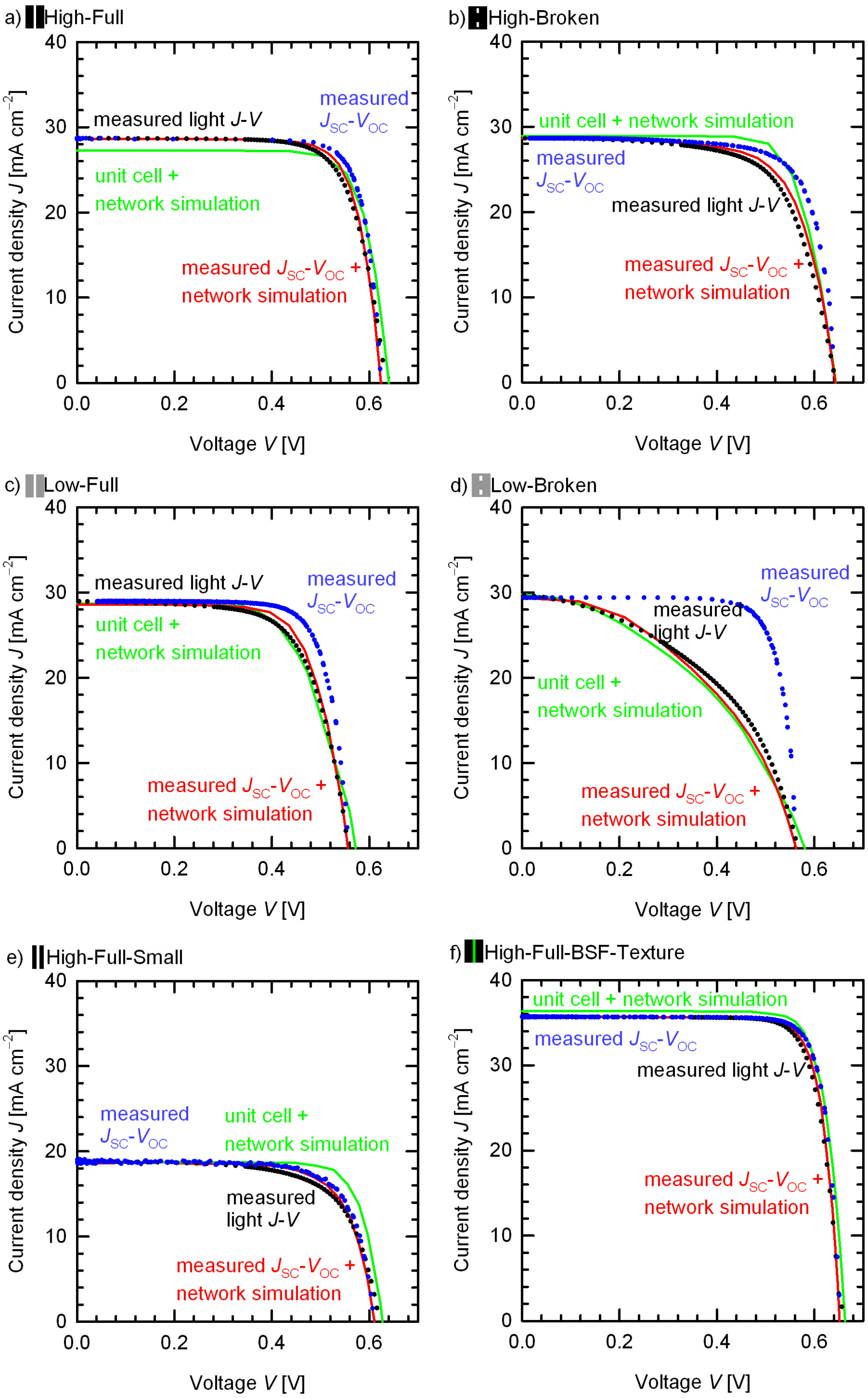

Figure 6.9: *J-V curves of the different cell groups. The measured light J-V curve and the measured J_{SC}-V_{OC} curve are plotted. The simulated J-V curve by combining the CoBo simulation of the unit cells and the series resistance network simulation is shown as well as the J-V curve which is simulated by combining the measured J_{SC}-V_{OC} curve and the series resistance network simulation. The simulations contain no free parameters.*

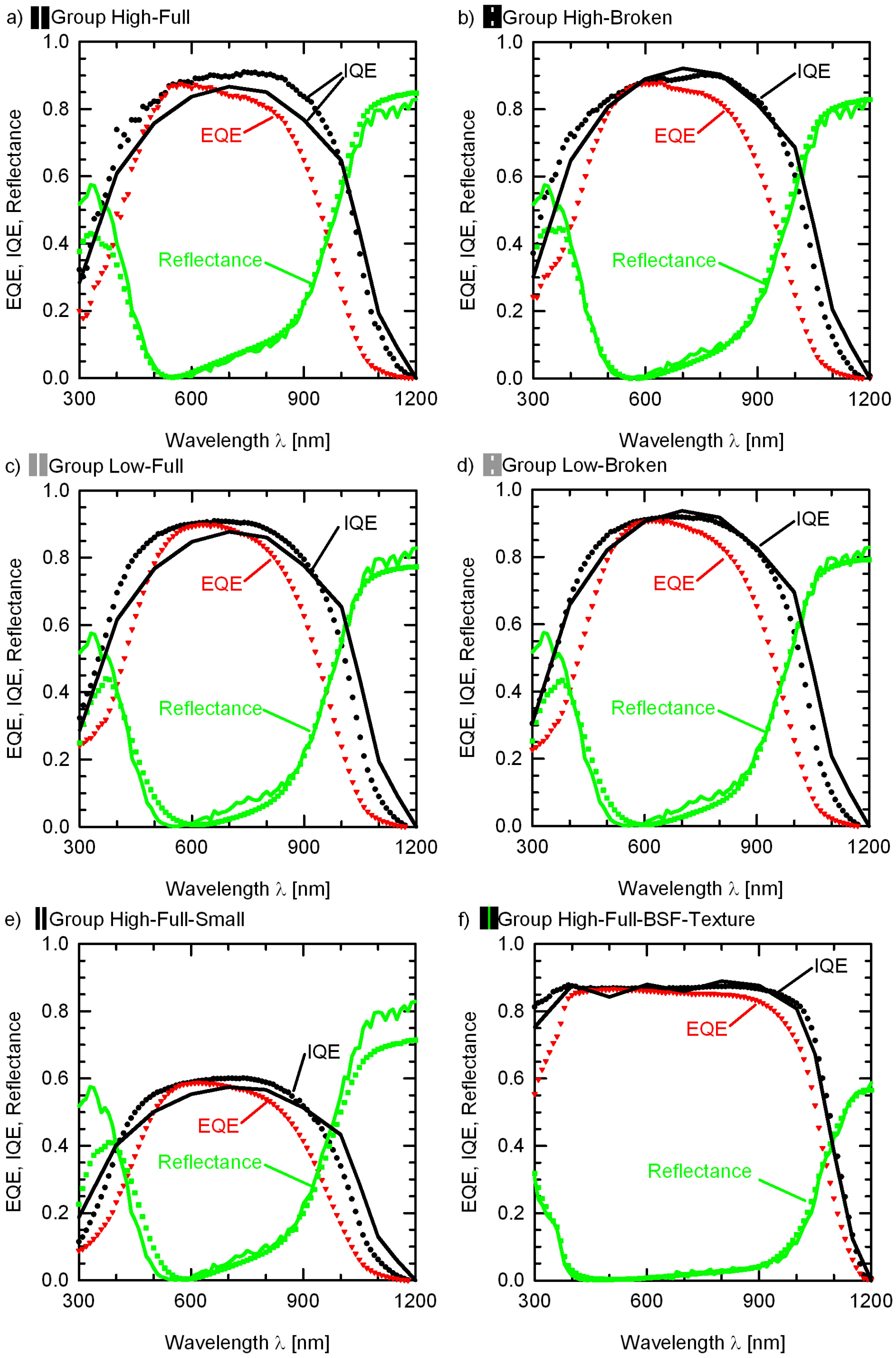

Figure 6.10: *Measured external quantum efficiency and measured and simulated internal quantum efficiency as well as reflection of the different cell groups. The simulations contain the same input parameters as the current-voltage-simulations and therefore no free parameters.*

sured light J-V curve of group High-Full (▮) additionally shows a higher current, which is probably due to a higher generation in this cell. The J-V curves of the CoBo simulated unit cells combined with the network simulation of group Low-Full (▯) and Low-Broken (▯) show lower fill factors than the measured light J-V curves. The effect of transport losses is overestimated in the CoBo simulation since the fill factor is mainly influenced by the transport loss of holes.

The difference between the network simulation of the measured J_{SC}-V_{OC} curve and the light $J-V$ curve is negligibly small. The power densities of these curves agree within an uncertainty of 2.6 %.

Figure 6.10 shows the measured external quantum efficiency and the measured and simulated internal quantum efficiency as well as reflection of the six groups investigated. For groups High-Broken (▮), Low-Broken (▯), High-Full-Small (‖) and High-Full-BSF-Texture (▮) measured and simulated data agree. Group High-Full (▮) shows a higher measured IQE from 400 nm to 1000 nm. This is probably due to a higher generation in this cell which is in agreement with comparison of the the measured light J-V curves. Group Low-Full (▯) shows also a higher measured IQE from 400 nm to 900 nm. This might be due to an overestimation of recombination at the base contact in the simulation. The first five groups show a higher simulated IQE at wavelengths of more than 1000 nm, which is due to an underestimation in parasitic absorption in the rear metal.

In this work, the first produced BC BJ PSI solar cell is from group High-Full-Small (‖) and has an energy conversion efficiency of 7.9 %. This work introduces a loss analysis of thin monocrystalline BC BJ solar cells, which identifies the major loss mechanisms in this and related solar cell concepts. As a result, an optimized layout for a BC BJ PSI solar cell is developed, which yields a conversion efficiency of 18.8 %. The key points for the more than doubled conversion efficiency are the increase of generated power density by a front texture, a decrease of recombination in the epitaxial layer and of base transport and resistance losses. We especially reduce the recombination at the base contact by the implementation of a BSF, we decrease the transport losses of majority carriers in the base by increasing the base doping density, and decrease the resistance of the aluminum fingers by reducing the finger length, respectively the cell area.

7 Luminescence cell measurements

The last section quantified all losses in the cells investigated in this work. This section confirms the simulation results with the interpretation of cell luminescence measurement results. Electroluminescence measurements are used for the analysis of the diffusion length as well as qualitative series resistance effects. Additionaly, the photoluminescence measurements confirm quantitatively the analyzed series resistance losses in the cells.

7.1 Electroluminescence measurements

7.1.1 Theory of electroluminescence

Electroluminescence measurements of the cells are used for qualitative investigations of the series resistance limiting the efficiency of the solar cells in groups Broken, as shown in Section 6.3 on page 69. Electroluminescence measurements are also used for quantitative investigation of the minority carrier diffusion length which limits the solar cell efficiency of all groups and in particular of group High-Full-Small (**II**), as shown in Section 6.2.3 on page 63.

Electroluminescence (EL) is the light which is emitted by band-to-band recombination. By applying a voltage to the cell, excess carriers are generated and transported through the cell. They recombine by different recombination processes on their path through the cell mentioned in Section 4.1.1 on page 30. The EL-emission at room temperature of forward-biased crystalline silicon solar cells can be measured with a commercial silicon CCD greyscale camera. Since the radiative recombination rate is proportional to the product of electrons and holes as described in Section 4.1.1 on page 30, the EL-intensity is also proportional to the product of electrons and holes. Consequently, a high EL-intensity corresponds to a high carrier lifetime, while reduced EL-intensities are an indication of increased Auger- or SRH-recombination [6, 59]. When analyzing EL-images it is important to know the contributions of the band-to-band recombination in the emitter, the base, and in the BSF to the electroluminescence intensity. Considering band-gap narrowing and free-carrier concentration, EL-imaging is sensitive to all effects affecting the rate of radiative recombination in the base of the solar cell whereas the contribution of the emitter and the BSF are negligible [59].

7.1.2 Results of electroluminescence analysis

Figure 7.1 shows a part of an EL-image of each of the six groups investigated. It features the regions of emitter and base finger as well as the region of the contacts. Since the lateral dimensions of the cell are much larger than its thickness, the carrier transport can

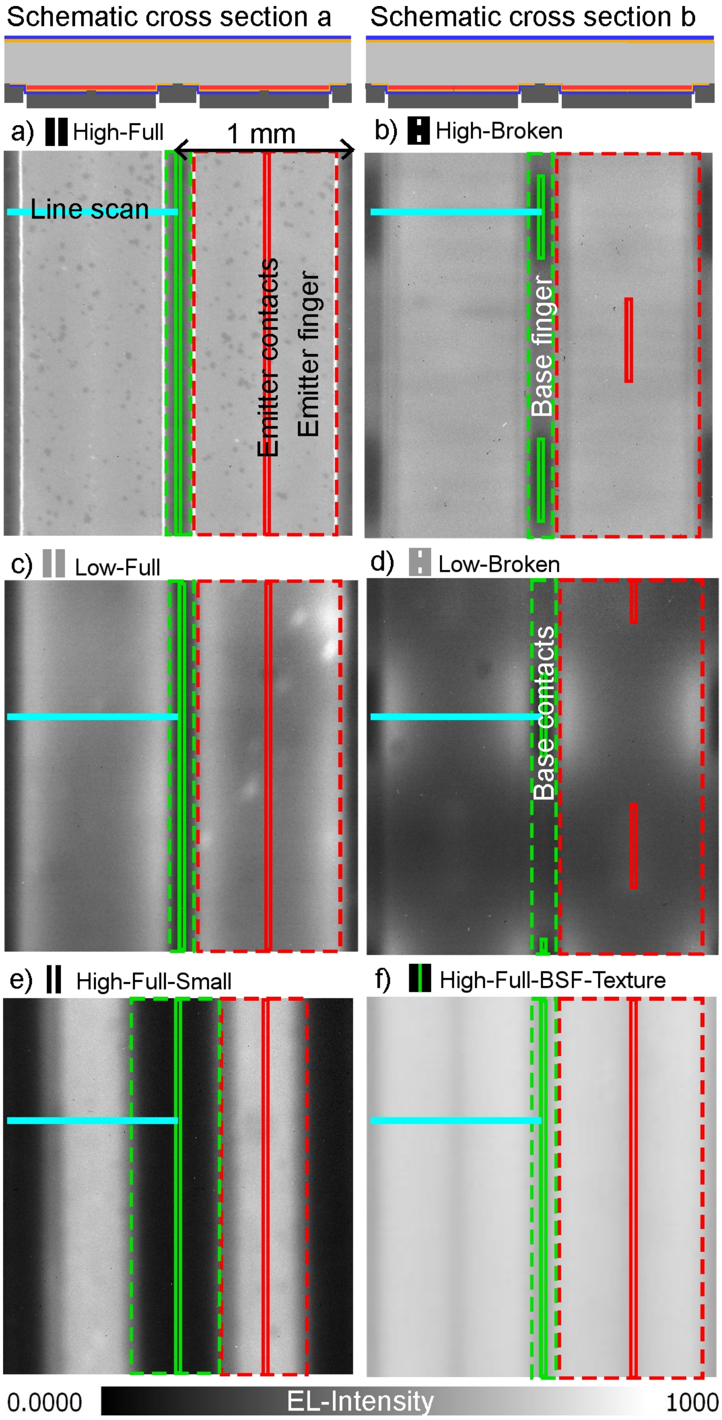

Figure 7.1: *Electroluminescence images of the six cell groups. The images are taken at room temperature. Each image shows a center part of the solar cell consisting of two emitter fingers and two base fingers. The emitter fingers and contacts are marked with red boxes whereas the base fingers and contacts are marked with green boxes. Line scans are marked in cyan. A high EL-intensity is caused by a high band-to-band recombination rate and quasi-Fermi level splitting.*

be assumed to be laterally only. A high series resistance in the base leads to a decrease in hole concentration with increasing distance to the base contact. This effect increases with decreasing doping concentration and is significant in high level injection. As a result, the band-to-band recombination towards the center of the emitter finger decreases.

The recombination losses in the bulk also influence the EL-intensity. The bulk recombination limits the diffusion length of the minority carriers which leads to a decrease of the electron concentration with decreasing distance to the emitter. Equation 7.1 gives the relationship of the minority carrier diffusion length L and the minority carrier lifetime τ

$$L = \sqrt{D_a \times \tau} \tag{7.1}$$

where D_a is the ambipolar diffusion constant depending on the doping concentration. In the base finger region, the electrons have to travel from the edge of the emitter laterally through the base. Therefore the carrier concentration drops exponentially with the distance to the emitter edge:

$$\Delta n(x) = \Delta n(0) \times \exp(-\frac{x}{L_{\mathrm{e}}}), \tag{7.2}$$

where $n(0)$ is the minority carrier concentration at the edge of the emitter, L_{e} is the minority carrier diffusion length and x the distance to the emitter edge.

The base contact recombination decreases the electron concentration significantly. The electron concentration increases with increasing distance to the base contact. If the recombination at the base contact is very high, the electron concentration is not limited by the saturation current density at the base contact but by the diffusion constant in the base.

Since these effects are not independent from each other we analyze the EL-images by comparing linescans of these EL-images with band-to-band recombination linescans that are output parameters of the unit cell transport simulation. This band-to-band recombination is proportional to the EL-intensity but does not consider reflection, which also influences the EL-intensity. The reflection of the cell is not homogeneous across the unit cell due to different layer stacks on the rear side. This leads to deviations between simulated and measured signals. Nevertheless, it is possible to analyze the influence of the series resistance as well as bulk recombination and base contact recombination.

The EL-measurement is the reverse photovoltaic process. This means that regions with a low EL-intensity also contribute only small amounts of electrons to the photocurrent under illumination. In particular the low intensity of the base finger region means that only a few electrons reach the electron contact where they are collected. This effect is known as electrical shading [20] whereas optical shading is the reflection of light by a front side metal finger resulting in no generation beneath this finger. The dark regions in the EL-images fit well to the electrical shading regions determined by the unit cell simulation as shown in Figure 6.5 in Section 6.2.3 on page 63.

The EL-images are taken at different voltages which are mentioned in the following discussion. The voltage drops at the contacts have to be subtracted from the measured voltage to gain the voltage which is used in the unit cell simulations.

7.1.3 Discussion of electroluminescence results

Group Low-Full (▮▮) is measured at a voltage of 670 mV, resulting in a current density of 90 mA cm^{-2}. Due to the high base contact resistance of 1 Ω cm^2 the voltage drops by 90 mV at the contacts. Group Low-Broken (▮) is measured at a voltage of 700 mV where the current density is 80 mA cm^{-2}. Due to the high base contact resistance of 1 Ω cm^2 the voltage drops by 80 mV at the contacts.

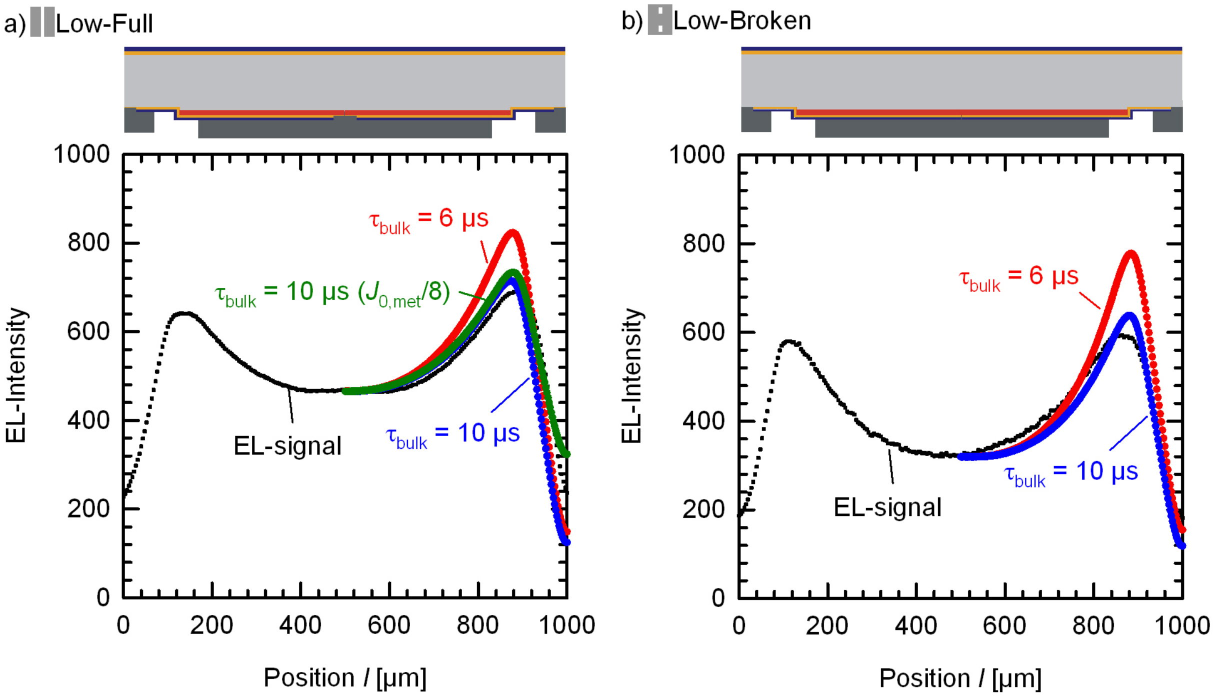

Figure 7.2: *Linescans of the EL-intensity of the groups Low-Full and Low-Broken. The schematic cross sections on top of the graphs show the corresponding region of the solar cell. The linescan begins at the center of a base finger, crosses the emitter finger and ends again in the center of a base finger. We also plot the band-to-band recombination, which is an output parameter of the unit cell transport simulation. This band-to-band recombination is proportional to the EL-intensity but does not consider reflection which influences the EL-intensity. In both groups the simulation with a bulk lifetime of* 10 μs *fits the EL-intensity best.*

The groups Low show a drop of the EL-intensity towards the center of the emitter finger of more than a third of the maximum intensity. This drop is due to the low doping density and the resulting high lateral base resistance, as illustrated in Figure 7.2. The intensity also decreases towards the center of the base finger due to bulk recombination and base contact recombination. Three simulated linescans for group Low-Full (▮▮) are shown in Figure 7.2a. We can determine a bulk lifetime of 10 μs, which mainly influences the band-to-band recombination in the emitter region. The bulk lifetime has no significant influence in the base finger region. This region is mainly influenced by the base contact recombination, as shown by a simulation in Figure 7.2a, which assumes an eight times lower saturation current density at the base contact than the measured value. Figure 7.2b shows the linescans for the group Low-Broken (▮). We can determine a bulk lifetime of 10 μs in this group, too.

Groups High-Full (▮▮) and High-Broken (▮) are measured at 670 mV and 650 mV, respectively. Due to the low base contact resistance of 0.1 $\Omega\,\mathrm{cm}^2$ the voltage drops only by about 10 mV at the contacts. The groups show only small EL-intensity drops to the center of the

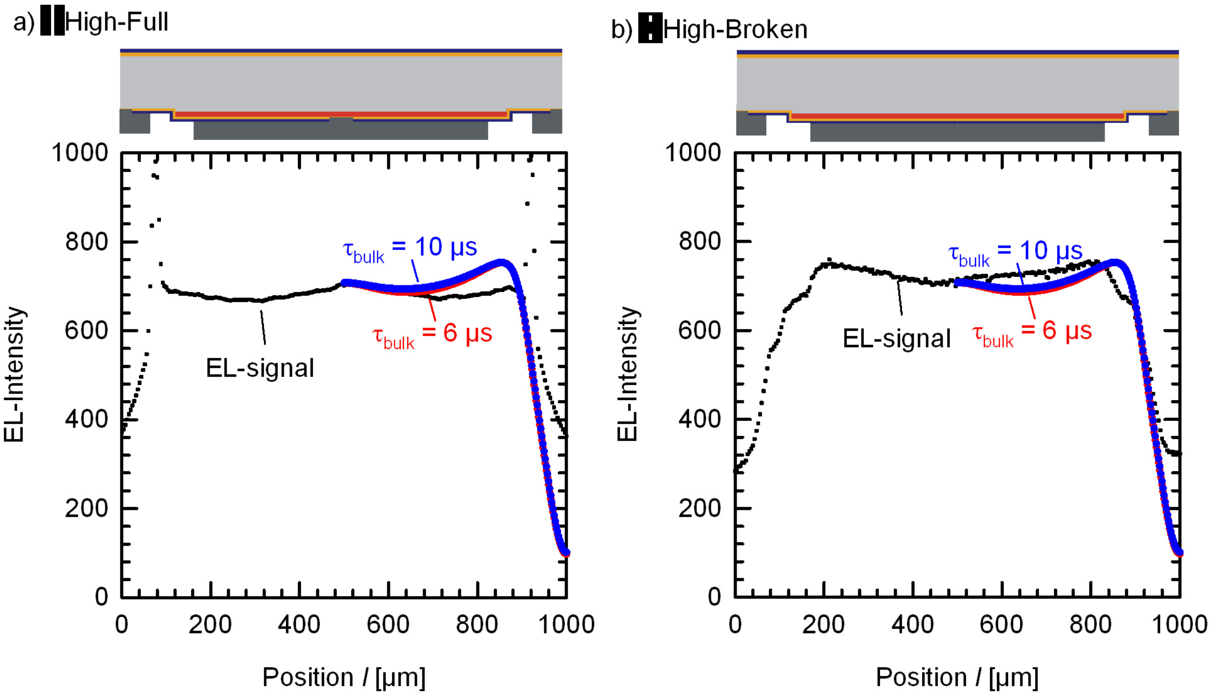

Figure 7.3: *Linescans of the EL-intensity of the groups High-Full and High-Broken. The schematic cross sections on top of the graphs show the corresponding region of the solar cell. The linescan begins at the center of a base finger, crosses the emitter finger and ends again in the center of a base finger. We also plot the band-to-band recombination, which is an output parameter of the unit cell transport simulation. This band-to-band recombination is proportional to the EL-intensity but does not consider reflection which influences the EL-intensity. In both groups the band-to-band recombination is not sensitive to the bulk lifetime.*

emitter finger due to the high doping density and the resulting low lateral base resistance, as illustrated in Figure 7.3. The intensity decreases towards the center of the base finger due to bulk recombination and base contact recombination. Two simulated linescans with different bulk lifetimes for group High-Full (▮▮) and High-Broken (▮) are shown in Figure 7.3a and Figure 7.3b, respectively. The band-to-band recombination in the base finger region is mainly influenced by the base contact recombination causing a diffusion limited recombination. The band to band recombination in these two groups is not sensitive to a bulk lifetime in the order of magnitude of 10 μs. Therefore we cannot extract the bulk lifetime from these measurements. We assume the same bulk lifetime of $10\,\mu$s as in groups Low since the layers were fabricated under the same conditions.

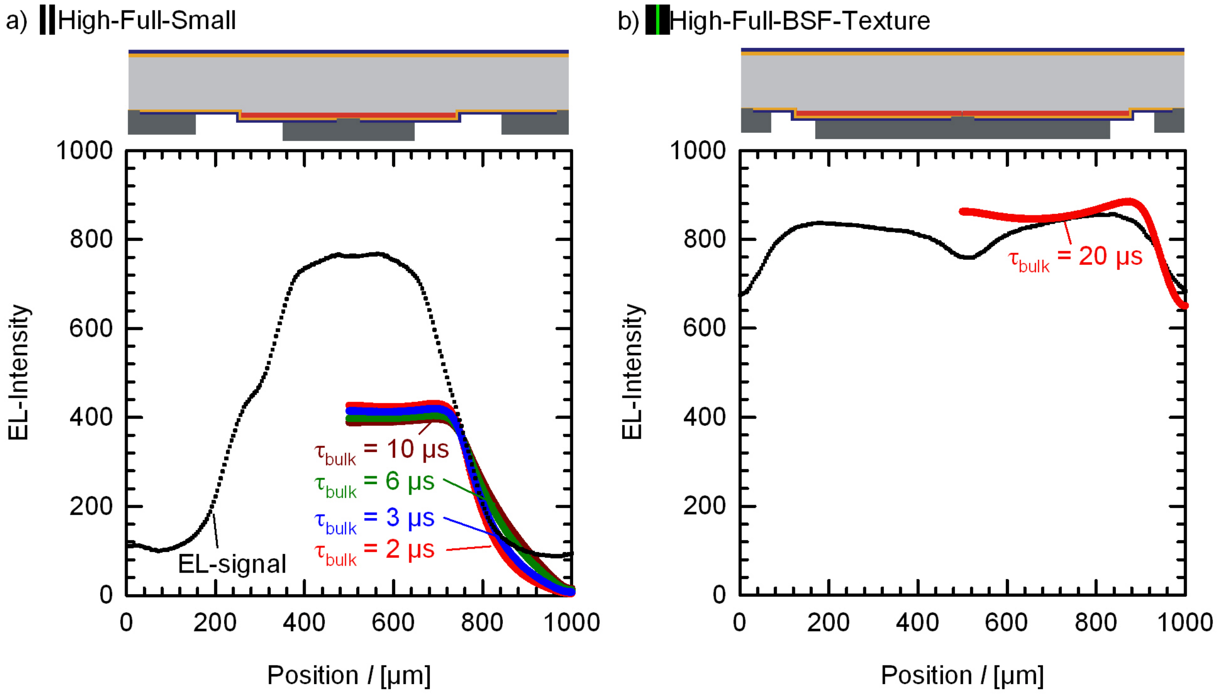

Figure 7.4: *Linescans of the EL-intensity of the groups High-Full-Small and High-Full-BSF-Texture. The schematic cross sections on top of the graphs show the corresponding region of the solar cell. The linescan begins at the center of a base finger, crosses the emitter finger and ends again in the center of a base finger. We also plot the band-to-band recombination, which is an output parameter of the unit cell transport simulation. This band-to-band recombination is proportional to the EL-intensity but does not consider reflection which influences the EL-intensity. In group High-Full-Small the simulation allows for the determination of the bulk lifetime due to the decay of the intensity from the emitter edge. A bulk lifetime of $3\,\mu$s fits the EL-intensity best. The bulk lifetime of group High-Full-BSF-Texture is determined by direct lifetime measurements. The simulation shows some deviations from the EL-intensity.*

Groups High-Full-Small (▮▮) and High-Full-BSF-Texture (▮🟩▮) are measured at 650 mV and 680 mV respectively. Due to the low base contact resistance of $0.1\,\Omega\,\mathrm{cm}^2$ the voltage drops only by about 10 mV at the contacts. The simulated linescans with different bulk lifetimes for group High-Full-Small (▮▮) are shown in Figure 7.4a. In this group the base finger is 2.5 times wider than in the other groups. Therefore the band-to-band recombination in the base finger next to the edge of the emitter is mainly influenced by bulk recombination, whereas the influence of the base contact and the passivated base finger is negligible. According to Equation 4.18 the effective lifetime differs less than 8 % from the bulk lifetime, if the a surface recombination velocity is less than $14\,\mathrm{cm\,s^{-1}}$ which is true for the passivated base finger region. By fitting the minority carrier diffusion length to the measured EL-intensity as well as to the simulated band-to-band recombination with a bulk lifetime of $3\,\mu$s, according to Equation 7.2, we extract an minority carrier diffusion length of $84\,\mu$m.

The bulk lifetime of group High-Full-BSF-Texture (▮) is determined by direct lifetime measurements as shown in Section 4.3.3 on page 49. The simulation of the band-to-band recombination with the measured bulk lifetime of $20\,\mu$s shows some deviations from the EL-intensity, as shown in Figure 7.4b. This is partly due to small differences in the recombination properties as well as to the inhomogeneous reflection, which influences the EL-intensity.

Table 7.1 summarizes the minority carrier bulk diffusion lengths and bulk lifetimes of all groups determined by EL-analysis. For the sake of completeness the table also shows the minority carrier lifetime of group High-Full-BSF-Texture (▮), which is directly measured by by quasi-staedy-state photoconductance decay.

In summary, the EL-image evaluation shows the impact of the series resistances and the recombination parameters on the EL-intensity. The analysis allows for the determination of the minority carrier diffusion length if some boundary conditions are fulfilled. It proves the applicability of the exponential decay method to the EL-images for the direct determination of minority carrier diffusion length in thin BC BJ cells with a planar front surface, wide base fingers and a low bulk lifetime. The analysis of photoluminescence measurements allows for the quantitative determination of the series resistance losses by separating the series resistance effects from the recombination effects as shown in the following Section 7.2.

7.2 Photoluminescence measurements

7.2.1 Theory of photoluminescence

Photoluminescence (PL) measurements are capable of quantitative analysis of series resistance losses [7]. Furthermore, the PL-analysis, in contrast to the EL-analysis, allows for separating recombination from resistance losses. As described in the last Section 7.1, dark areas in the EL image are either caused by high series resistance, high recombination, or low shunt resistance, whereas dark areas in the PL-image are only due to high recombination or low shunt resistance, whereas high series resistance areas are bright.

In electroluminescence measurements, excess carriers are generated by application of an external voltage. In photoluminescence measurements, on the other hand, excess carriers are generated through illumination. When measuring solar cells, an additional bias light might also be applied. In the used setup the cell is irradiated by a laser at a wavelength of 808 nm and the light is homogeneously distributed across the whole cell area. The luminescence is again detected by a CCD camera. One PL-image is taken at open-circuit conditions with a low illumination intensity and another one is taken at the MPP of the cell at higher illumination intensity [7]. Both images are corrected for the diffusion-limited carrier density with an image taken at the corresponding illumination intensity but at short-circuit conditions. The evaluation of the image taken at open-circuit conditions assumes

Table 7.1: *Minority carrier diffusion length L_{e} evaluated by EL-measurements and measured by quasi-staedy-state photoconductance decay (group High-Full-BSF-Texture).*

	High-Full (■)	High-Broken (■)	Low-Full (▨)	Low-Broken (▨)	High-Full-Small (■)	High-Full-BSF-Texture (🟩)
Minority carrier diffusion length L_{e} [μm]	153	153	184	184	84	217
Bulk lifetime τ_{bulk} [μs]	10	10	10	10	3	20

that the local voltage is equal to the terminal voltage, which is the case, if the lateral series resistances are negligible. This assumption only holds for the emitter region in our BC BJ cells. Therefore only the series resistances in the emitter region are evaluated with the PL-method.

7.2.2 Results and discussion of photoluminescence analysis

Figure 7.5 shows series resistance images of the six groups investigated. In the following we discuss the measurements of each group separately.

Group High-Full (▮▮)

Figure 7.5 shows that group High-Full suffers from series resistances ranging from 0 to $5\,\Omega\,\mathrm{cm}^2$. Most of the cell area shows series resistances from 1 to $2\,\Omega\,\mathrm{cm}^2$. Only three broken fingers show the high series resistances of up to $5\,\Omega\,\mathrm{cm}^2$. The image in the lower right corner shows a center part of the cell including six fingers. The different areas like base finger, base contacts, emitter finger and emitter contacts are marked with boxes.

Figure 7.6 shows two linescans of the PL-image of the cell indicated in Figure 7.5a. The left graph shows the linescan across half of a base finger a full emitter finger and half of a base finger again. As already mentioned the evaluation is only valid in the emitter region which, is indicated by the black box. The series resistance is $1.45\,\Omega\,\mathrm{cm}^2$ and nearly constant across the emitter region, which is in agreement with the EL analysis in Figure 7.3. We determine a lumped series resistance of $1.2\,\Omega\,\mathrm{cm}^2$ by the two-diode model in Table 3.1 on page 17 in Section 3.1.2, which is similar to the local series resistance analyzed by PL.

The right graph in Figure 7.6 shows a linescan of the series resistance along an emitter finger of the whole cell. There is a significant difference in series resistance of $1\,\Omega\,\mathrm{cm}^2$ from one end to the other of the emitter finger. This difference is due to the high voltage drop along the base finger which has a small cross section and is 88 mm long.

Group High-Broken (▮)

Figure 7.5b shows that group High-Broken has series resistances from 1.5 to $2.5\,\Omega\,\mathrm{cm}^2$. A center part of the cell with ten fingers is shown. The linescan which is shown in Figure 7.7 is across half of the base finger, the full emitter finger and half of the base finger again. The series resistance in the emitter region is $1.85\,\Omega\,\mathrm{cm}^2$ and increases by only $0.05\,\Omega\,\mathrm{cm}^2$ towards the center of the emitter finger. This value is $0.4\,\Omega\,\mathrm{cm}^2$ higher than in group High-Full due to the broken contact layout. The small increase towards the center of the emitter finger in the PL-linescan is in agreement with the small decrease towards the center of the emitter finger in the EL linescan in Figure 7.3.

Groups Low

Figure 7.5c and d show series resistance images, both of groups Low-Full and Low-Broken of the whole cell as well as a center part of the cell comprising six fingers. Group Low-Full has series resistances from 0 to $7\,\Omega\,\mathrm{cm}^2$ whereas group Low-Broken has series resistances from 0 to $14\,\Omega\,\mathrm{cm}^2$. Linescans of the series resistances across the emitter fingers indicated in the detailed image with six fingers are shown in Figure 7.8c and d. The left graph shows the

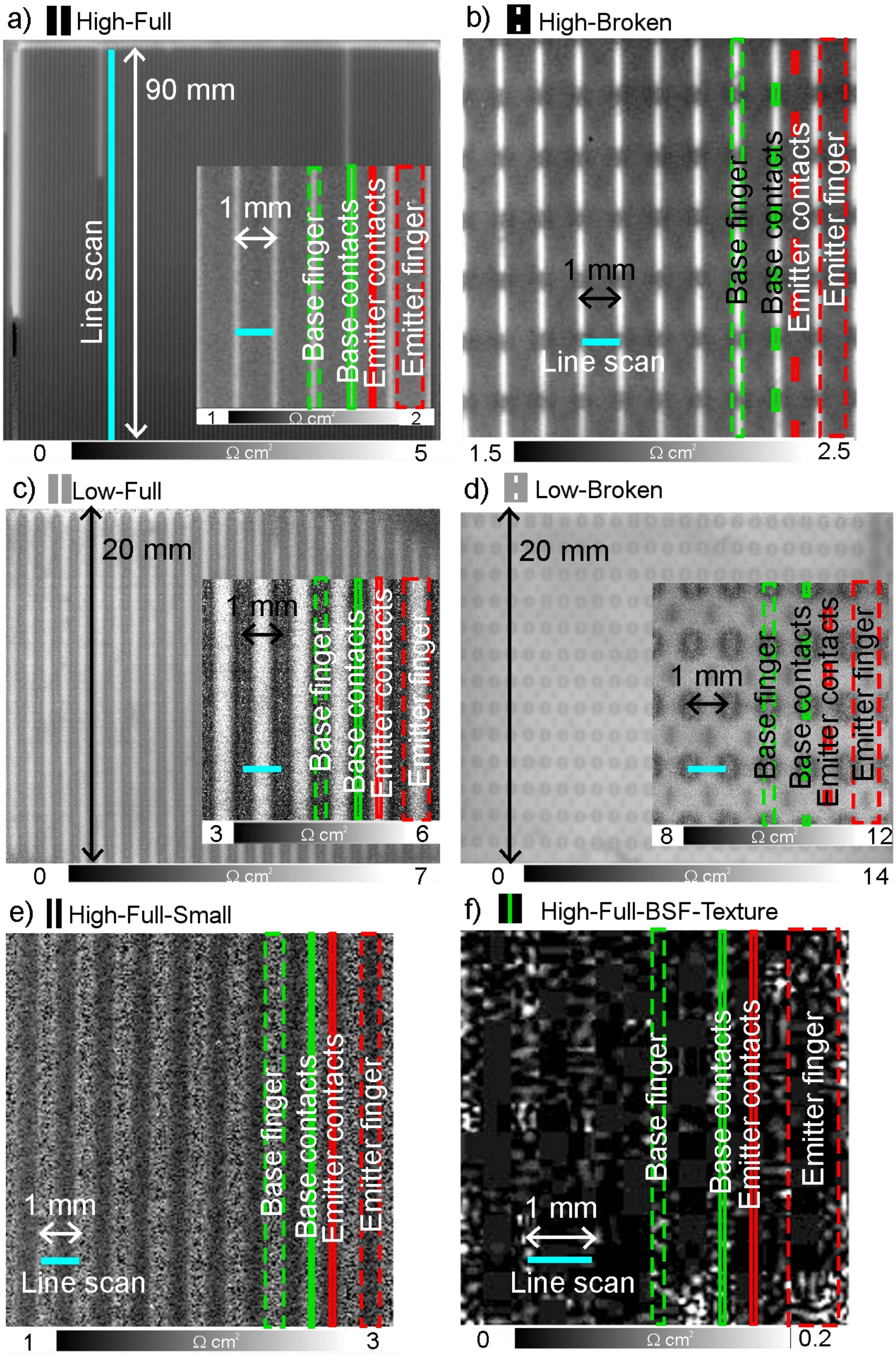

Figure 7.5: *Series resistance images of the six investigated cell groups. For groups High-Full, Low-Full and Low-Broken a series resistance image of the whole cell is shown. In addition, an image of the center part of the cell is shown for every group. The evaluation is valid in the emitter region of the cell.*

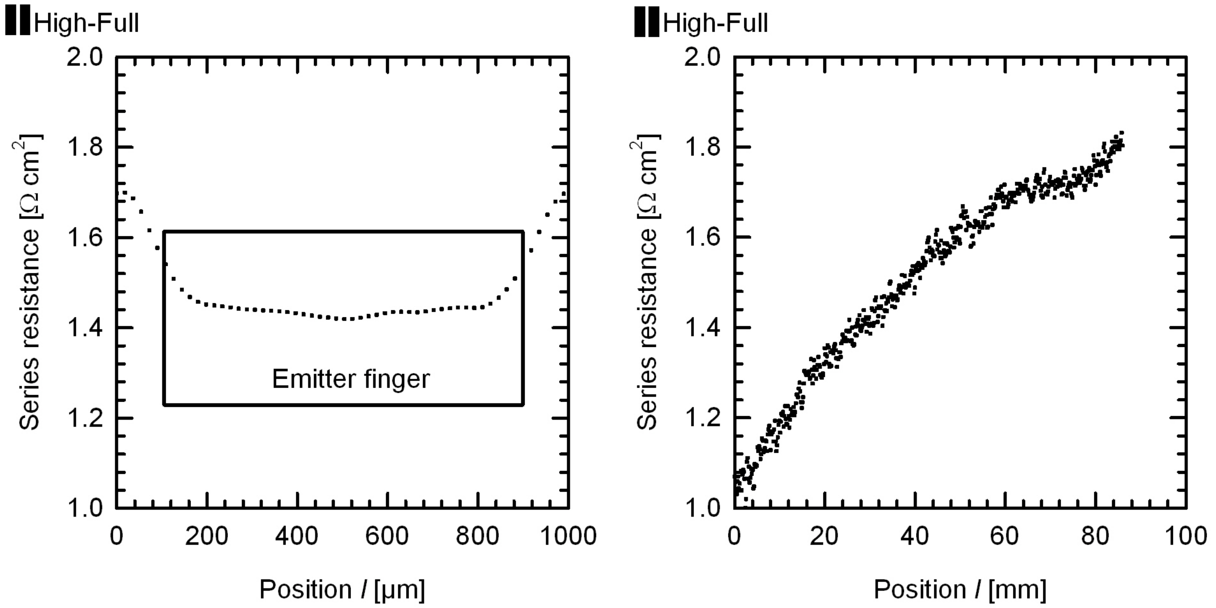

Figure 7.6: *Series resistance linescans of group High-Full. The left graph shows a linescan across an emitter finger and the right graph shows a linescan along an emitter finger. Both linescans are indicated in Figure 7.5*

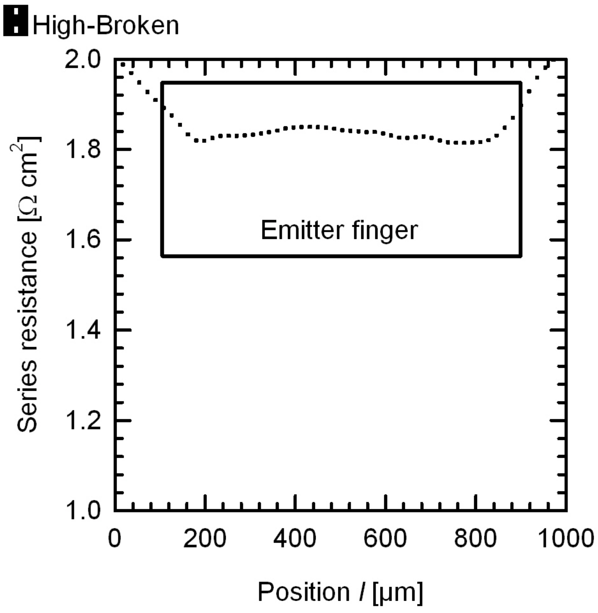

Figure 7.7: *Series resistance linescan across an emitter finger of group High-Broken. The linescan is indicated in Figure 7.5b*

series resistance across an emitter finger of group Low-Full whereas the right graph shows the series resistance across an emitter finger of group Low-Broken. The series resistance increases towards the center of the emitter finger due to the high resistance (low doping) in

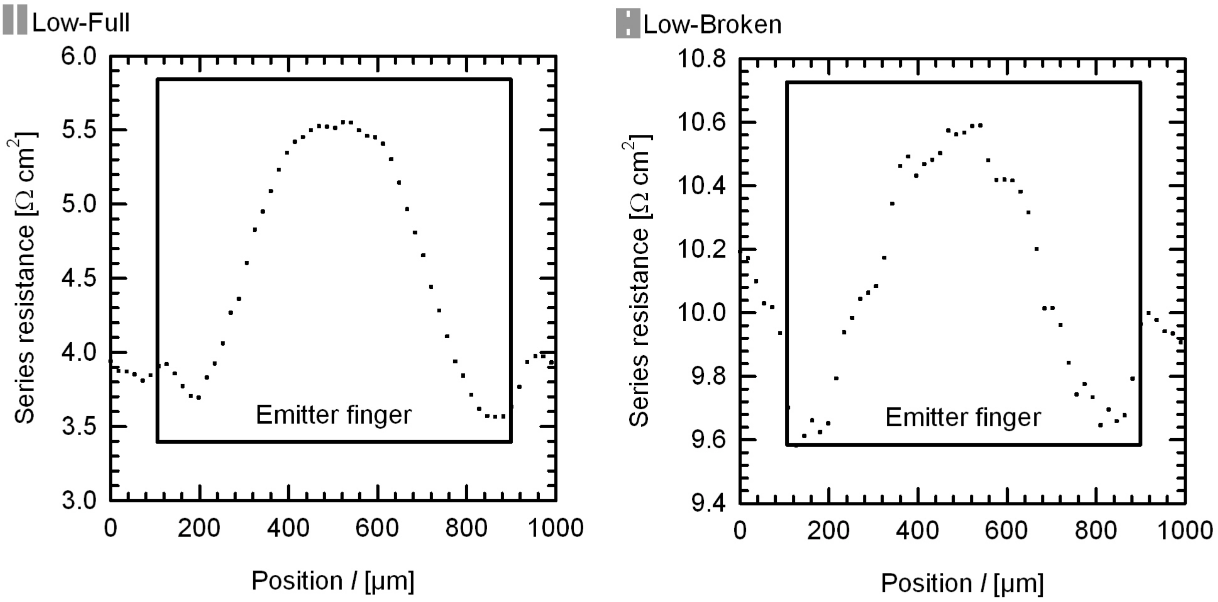

Figure 7.8: *Series resistance linescans across emitter fingers of group Low-Full and group Low-Broken. Both linescans are indicated in Figure 7.5c and d*

the base of these groups. In group Low-Full the series resistance increases up to 5.5 Ω cm^2 whereas in group Low-Broken the series resistance increases to 10.6 Ω cm^2 due to the broken contact layout. These results are in agreement with the results of the EL analysis which are discussed in Section 7.1, where the large voltage drop causes a large decrease of the EL-intensity towards the center of the emitter finger.

Group High-Full-Small (II)

Figure 7.5e shows that group High-Full-Small has series resistances from 1 to 3 Ω cm^2. A center part of the cell with 10 fingers is shown. The linescan which is shown in Figure 7.9 is across half of the base finger, the full emitter finger and half of the base finger again. The series resistance in the emitter region is about 1.6 Ω cm^2. The intensity of the base finger, which cannot be evaluated, influences the intensity of the edge of the emitter finger. The series resistance of 1.6 Ω cm^2 is comparable to the series resistance in group High-Full (1.45 Ω cm^2) due to the same base doping and contact layout. The differences between both groups are only the width of the fingers and the bulk lifetime. The PL-linescan is in agreement with the EL-linescan in the left graph of Figure 7.4. We determine a lumped series resistance of 1.5 Ω cm^2 by the two-diode model in Table 3.1 on page 17 in Section 3.1.2, which is similar to the local series resistance of 1.6 Ω cm^2 analyzed by PL.

Group High-Full-BSF-Texture (II)

Figure 7.5f shows that group High-Full-BSF-Texture has series resistances in the range of 0 to 0.2 Ω cm^2. A center part of the cell with six fingers is shown. The linescans indicated in Figure 7.5f are plotted in Figure 7.9.

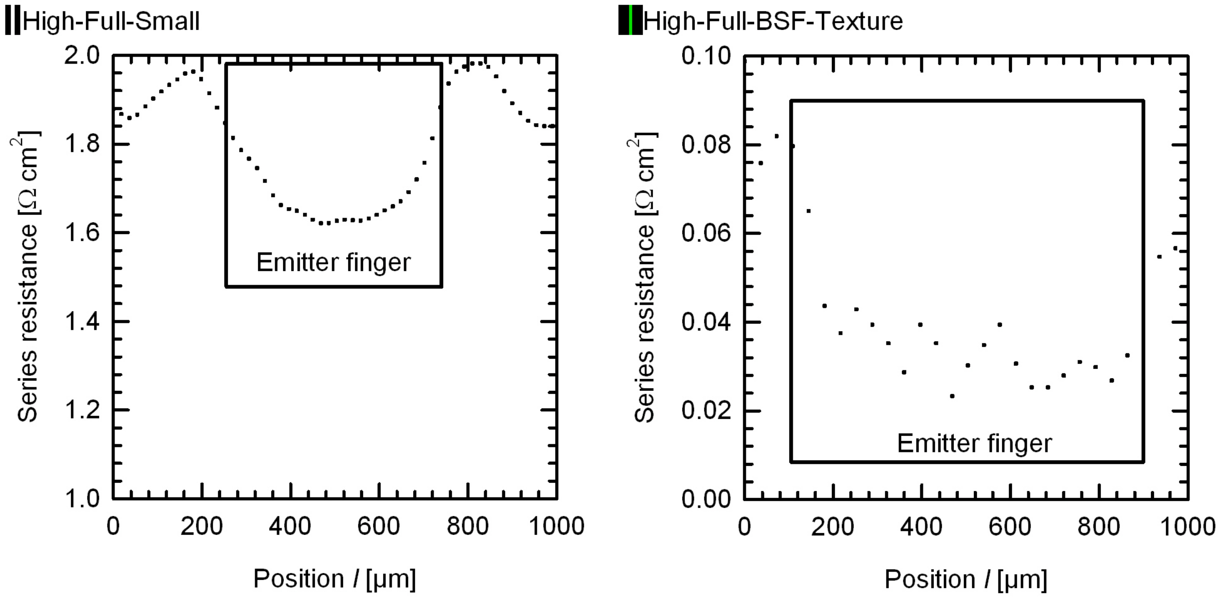

Figure 7.9: *Series resistance linescans across emitter fingers of group High-Full-Small and group High-Full-BSF-Texture. Both linescans are indicated in Figure 7.5e and f*

The linescan which is shown in Figure 7.9 is across half of the base finger, the full emitter finger and half of the base finger again. The linescan shows that the series resistance is less than 0.2 Ω cm^2. This very low series resistance is due to the low lateral resistances in the base and emitter (highly doped), the low contact resistances (highly doped silicon/metal interfaces) and low resistances in the metal grid due to short fingers of 20 mm. We determine a lumped series resistance of 0.4 Ω cm^2 by the two-diode model in Table 3.1 on page 17 in Section 3.1.2, which is similar to the local series resistance of 0.2 Ω cm^2 analyzed by PL.

This PL series resistance evaluation quantitatively analyzes the resistance losses with a spatial resolution. The results are in agreement with the qualitative tendencies demonstrated by the EL evaluation in Section 7.1 on page 77 and with the *J*-*V* characterization of Section 3 on page 15.

8 Simulation study

This chapter studies the solar cell conversion efficiency in dependence on various limiting cell loss mechanisms. The sensitivity analysis is based on measured parameters which are varied in a physically and technologically reasonable range. Chapter 6 showed that the limiting loss mechanisms of the best group (High-Full-BSF-Texture) are SRH-recombination as well as base contact and BSF recombination. The high SRH-recombination is caused by a high defect density created during the epitaxial growth process. The SRH-recombination can be reduced by optimizing the growth conditions. A reasonable lower limit for the SRH-recombination in an epitaxial layer is the SRH-recombination in a float zone wafer. Therefore we vary the base lifetime between the measured values of the epitaxial layers used in these investigations and the measured values of a float zone wafer.

Chapter 6 also showed a strong influence of the emitter fraction on the solar cell conversion efficiency due to the low diffusion length of minority carriers and a high recombination of the minorities at the base contact. Therefore we vary the emitter fraction by changing the emitter and base finger widths in a technologically reasonable range. We keep the sum of both widths constant. By increasing the emitter fraction all recombination losses decrease a lot, in contrast to a small increase of the emitter recombination. At the same time the resistive losses in the metal grid increase due to a decreased cross section of the metal base finger. The metal finger, which contacts the base, could overlap with the emitter, however, that would require an electrical insulating layer. The increased resistive losses limit the cell size since the series resistance increases quadratically with the finger length.

Another possibility to avoid high losses by minority carrier recombination in the base and at the base contact is the implementation of a doped layer with the opposite polarity of the base, also called floating emitter. The floating emitter allows for a transport of the electrons from the base finger region to the emitter finger region where the electrons only face a low recombination. The saturation current density of $20\,\mathrm{fA\,cm^{-2}}$ and the sheet resistance of

Table 8.1: *Simulation parameter space for the sensitivity analysis and measured values of group High-Full-BSF-Texture*

Parameter	High-Full-BSF-Texture	Lower limit	Upper limit
Minority carrier lifetime [μs]	20	2	3000
Emitter fraction	0.84	0.5	0.94
Floating emitter	No	No	Yes
Cell thickness [μm]	45	18	290

$200\,\Omega/\square$ of the floating emitter is determined by measurements and used for the following simulations.

We also analyze the dependence of the cell thickness on the cell efficiency since the energy which is used for production and the costs of the final cell are strongly related to the amount of the used epitaxial material. Therefore we vary the cell thickness in a technologically reasonable range of $18\,\mu$m to $290\,\mu$m.

Table 8.1 shows the parameter space used in the following unit cell simulations. We plot the efficiency and the main power losses as a function of the cell thickness and emitter fraction. These plots are done for each of the different minority carrier lifetimes.

8.1 Minority carrier lifetime of $20\,\mu$s

The highest lifetime which we measure in our solar cell devices fabricated by the PSI process is $20\,\mu$s (in group High-Full-BSF-Texture (■)). The emitter fraction of this group is 0.84 and the cell thickness is $45\,\mu$m. The experimentally achieved conversion efficiency is plotted in Figure 8.1a. Figure 8.1 shows the conversion efficiency and main power losses in absolute efficiency points. The left column shows the results without a floating emitter whereas the right column shows the results with a floating emitter. We indicate the impact of the free energy of generation as well as loss mechanisms by arrows in the conversion efficiency plots.

The generated free energy increases with increasing cell thickness. The main power losses are the SRH recombination, as shown in Figure 8.1e and f, and the recombination at the base contacts and at the BSF, as shown in Figure 8.1c and d. The SRH recombination increases with increasing cell thickness. The minority carriers diffuse from the front surface of the cell, where most of the carriers are generated, to the rear emitter, where they are collected. Due to the diffusion length of $217\,\mu$m many minority carriers recombine in thick cells. This leads to a decrease of minority carrier concentration with increasing distance to the front surface. The SRH recombination decreases only slightly with a floating emitter.

With decreasing cell thickness the number of electron paths in the base finger region, which end at the BSF or base contact, and thus the eletricial shading, increases. For this, the recombination at the base and the base contact increases. It also increases with decreasing emitter fraction without a floating emitter shown in Figure 8.1c. The recombination at the base and the base contact is reduced with the implementation of a floating emitter and shows nearly no dependence on the emitter fraction, as shown in Figure 8.1d. Figure 8.2 shows cross section plots of the unit cells with an emitter fraction of 0.5 and a cell thickness of $45\,\mu$m. Figure 8.2a (without a floating emitter) shows a large area of electrical shading where the carriers all recombine at the base contact and the BSF (whole base finger width). Figure 8.2b shows that the cell with a floating emitter shows no electrical shading. The minority carrier paths in the cell without a floating emitter start at the front surface and end at the rear BSF or base contact where the minority carriers recombine. The minority carrier paths in the cell with a floating emitter start at a certain distance to the front surface of the cell. Most of the minority carriers are generated above this line and follow the paths into the floating emitter. There, they are conducted to the emitter finger region and from

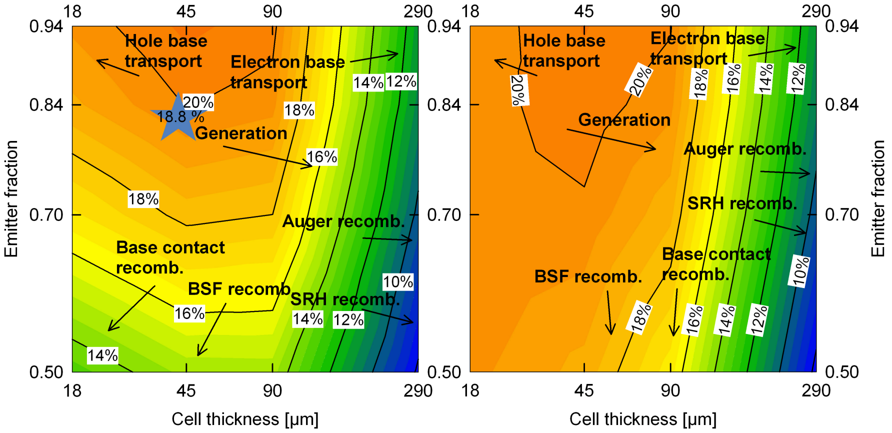

Without floating emitter

a) Conversion efficiency

With floating emitter

b) Conversion efficiency with fl. em.

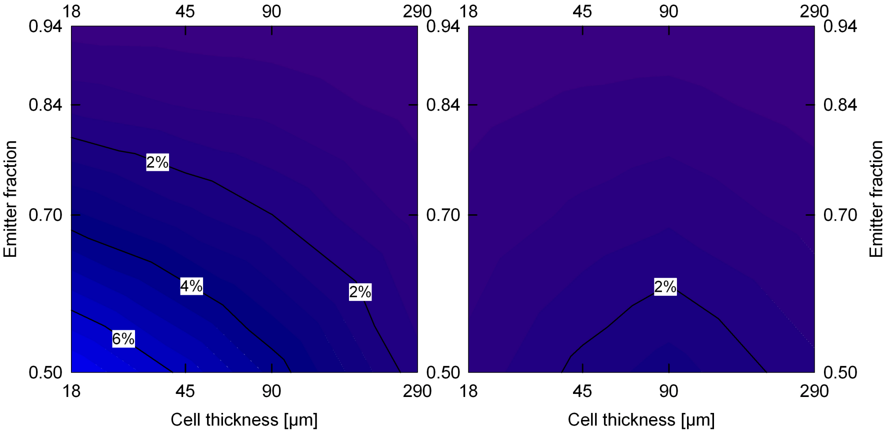

c) Base contact and BSF recombination

d) Base contact and BSF recombination with fl. em.

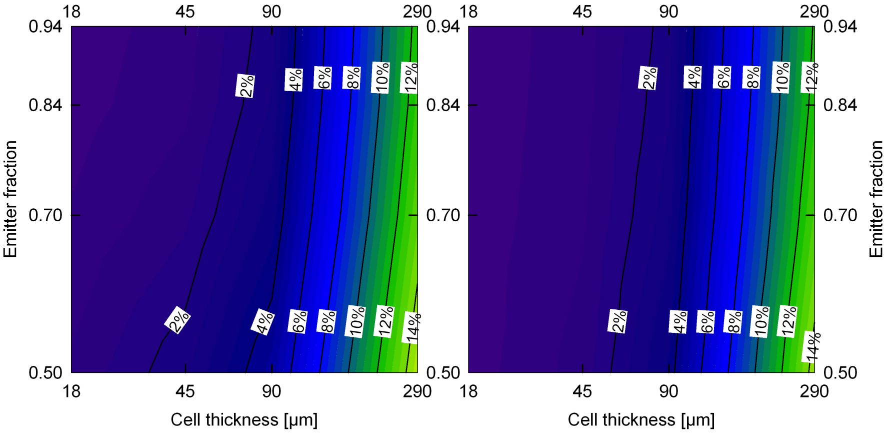

e) SRH recombination

f) SRH recombination with fl. em.

Figure 8.1: *Conversion efficiency and main power losses in absolute efficiency points at a bulk lifetime of* 20 μs. *The results with and without floating emitter are shown. The conversion efficiency as well as the power losses are plotted as a function of cell thickness and emitter fraction. We indicate the impact of the free energy of generation as well as loss mechanisms by arrows in the conversion efficiency plots. The experimentally achieved efficiency of* 18.8 % *is marked in plot (a).*

there they follow the paths from the floating emitter through the base to the emitter where they are collected. Only a few carriers are generated beneath this line, as shown by the generation profiles in Figure 6.3 on page 60, and recombine at the BSF or base contact.

The SRH recombination in the base finger region is about five times higher without a floating emitter. Without a floating emitter the minority carriers diffuse up to 250 μm laterally through the base. Due to the low diffusion length of 217 μm many of them recombine on their way to the emitter. With a floating emitter the minority carriers are conducted via the floating emitter, which has a low saturation current density of 20 fA cm^{-2}.

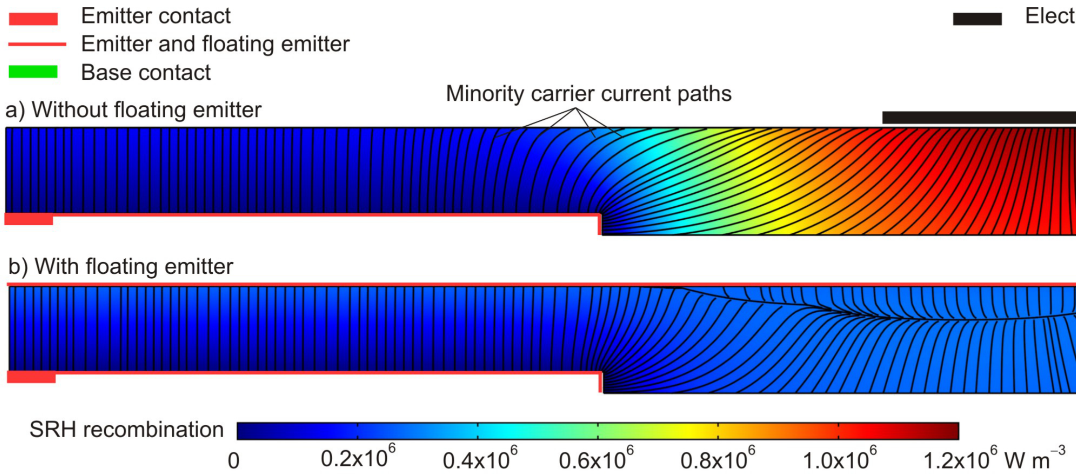

Figure 8.2: *SRH-recombination and minority carrier current paths of the unit cells without and with floating emitter. The minority carrier current paths are plotted by black lines. The region of the contacts, as well as the region of the emitter and, if present, floating emitter is shown in every unit cell. The cell without a floating emitter shows a large area of electrical shading.*

Besides SRH recombination, Auger recombination and electron transport losses also increase with increasing cell thickness, as indicated by arrows in Figures 8.1a and b. The free energy transport loss of electrons is a quadratic function of the electron quasi-Fermi level gradient. The quasi-Fermi level gradient is a result of the decay of the minority carrier concentration with increasing distance to the front surface. Since the electron quasi-Fermi level gradient decreases with increasing distance to the emitter, the total electron transport loss $F_{\mathrm{bt_e}}$ increases with an exponent x of less than one with increasing distance to the emitter and thus increasing cell thickness d ($F_{\mathrm{bt_e}} \propto d^x$, $x < 1$). The Auger recombination also increases with increasing cell thickness due to the electron quasi-Fermi level gradient to the front surface which results in a higher quasi-Fermi level splitting. On the other hand, hole transport losses increase with decreasing cell thickness in addition to BSF and base contact recombination. The holes are transported laterally through the base to the base contact. The losses by this transport increase with decreasing cell thickness due to an increased sheet resistance in the base.

In summary, thinner cells benefit from lower recombination in the base and lower electron transport losses but at the same time suffer from a reduced generation, increased recombination losses at the rear surface (BSF and base contacts) and increased hole transport losses. Thus a low recombination in the BSF and the base contact becomes more important for thinner cells. Without a floating emitter the maximum efficiency for the base lifetime of 20 μs is 20.5 % at an emitter fraction of 0.94 and a cell thickness of 45 μm. The implementation of a floating emitter decreases the recombination at the BSF and base contact and thus increases the conversion efficiency by up to 6 % absolute for thin cells with a low emitter fraction.

8.2 Minority carrier lifetime of 2 μs

We also measure a bulk lifetime of only 3 μs in the epitaxial layers. Figure 8.3 shows the conversion efficiency and main power losses in absolute efficiency points for a bulk lifetime of 2 μs. The left column shows the results without a floating emitter whereas the right column shows the results with a floating emitter. We indicate the impact of the free energy of generation as well as loss mechanisms by arrows in the conversion efficiency plots.

The main power losses at a bulk lifetime of 2 μs are SRH recombination, as shown in Figure 8.3e and f, and the recombination at the base contacts and at the BSF, as shown in Figure 8.3c and d. Since the diffusion length is only 69 μm the power loss by SRH recombination significantly increases compared to a bulk lifetime of 20 μs. The efficiency is less than 2 % at a cell thickness of 290 μm. The SRH recombination decreases with a floating emitter for thin cells with a low emitter fraction. The recombination at the base and the base contact shows the same tendencies as for a bulk lifetime of 20 μs. The absolute power losses by these mechanisms decrease since the increased SRH recombination decreases the minority carrier concentration much more significantly. The other power losses are similar to the losses at a bulk lifetime of 20 μs. Nevertheless, a conversion efficiency of more than 18 % is possible at a cell thickness of 18 μm. This efficiency is nearly independent on the emitter fraction after the implementation of a floating emitter.

8.3 Minority carrier lifetime of 200 μs and 3000 μs

Epitaxial layers are monocrystalline without any impurities such as oxygen or metals. Therefore a bulk lifetime of 200 μs and even up to 3000 μs, as is measured on float zone wafers, is feasible. Figure 8.4 and Figure 8.5 show the conversion efficiency and main power losses in absolute efficiency points for a bulk lifetime of 200 μs and 3000 μs, respectively. The left columns show the results without a floating emitter whereas the right columns show the results with a floating emitter. We indicate the impact of the free energy of generation as well as loss mechanisms by arrows in the conversion efficiency plots.

At a bulk lifetime of more than 200 μs the main power density loss is the recombination at the base contacts and at the BSF, as shown in Figure 8.4c and d, and Figure 8.5c and d, respectively. Compared to the 20 μs lifetime case, this recombination increases due

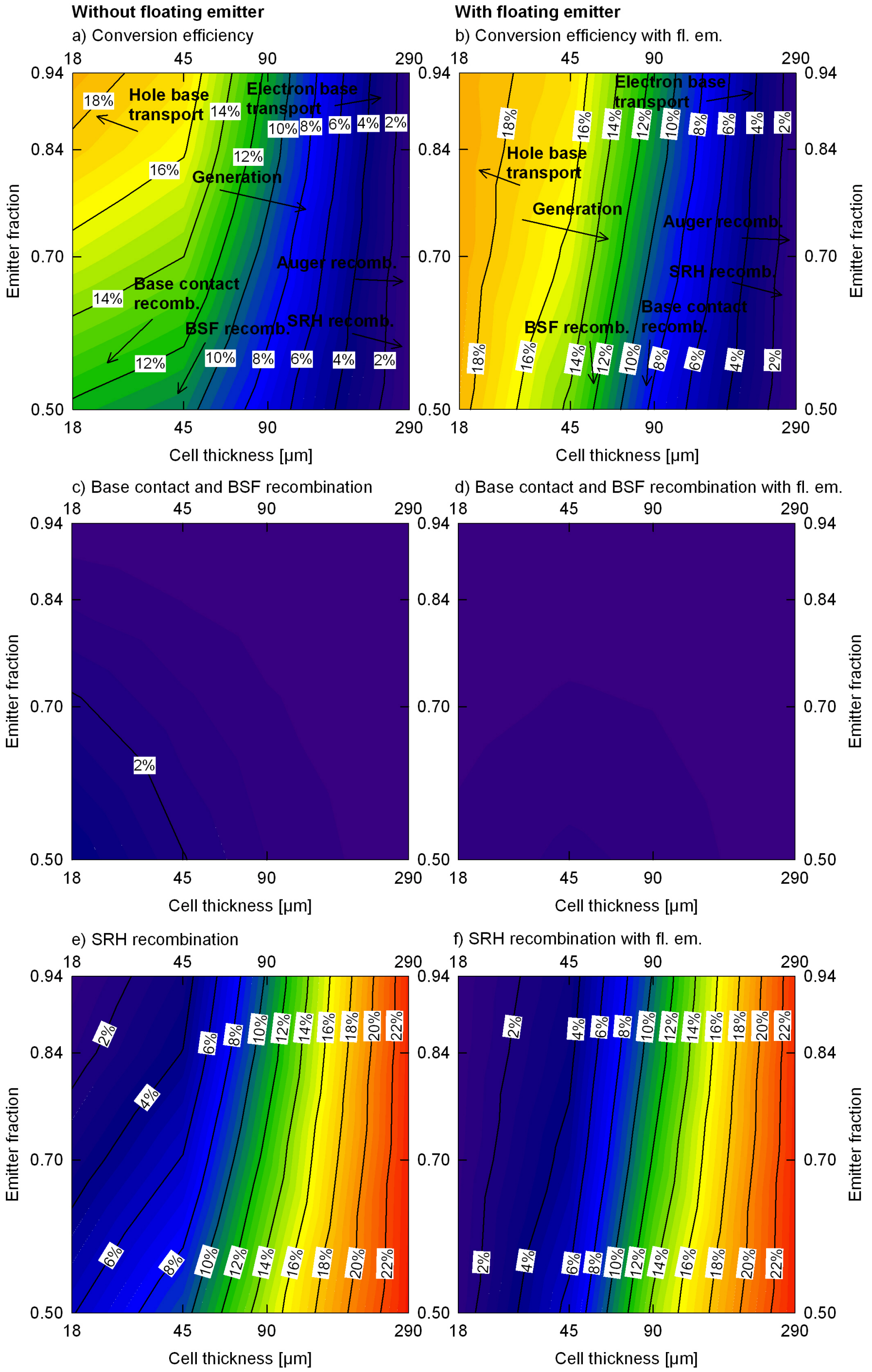

Figure 8.3: *Conversion efficiency and main power losses in absolute efficiency points for a bulk lifetime of* 2 *µs. The results with and without floating emitter are shown. The conversion efficiency as well as the power losses are plotted as a function of cell thickness and emitter fraction. We indicate the impact of the free energy of generation as well as loss mechanisms by arrows in the conversion efficiency plots.*

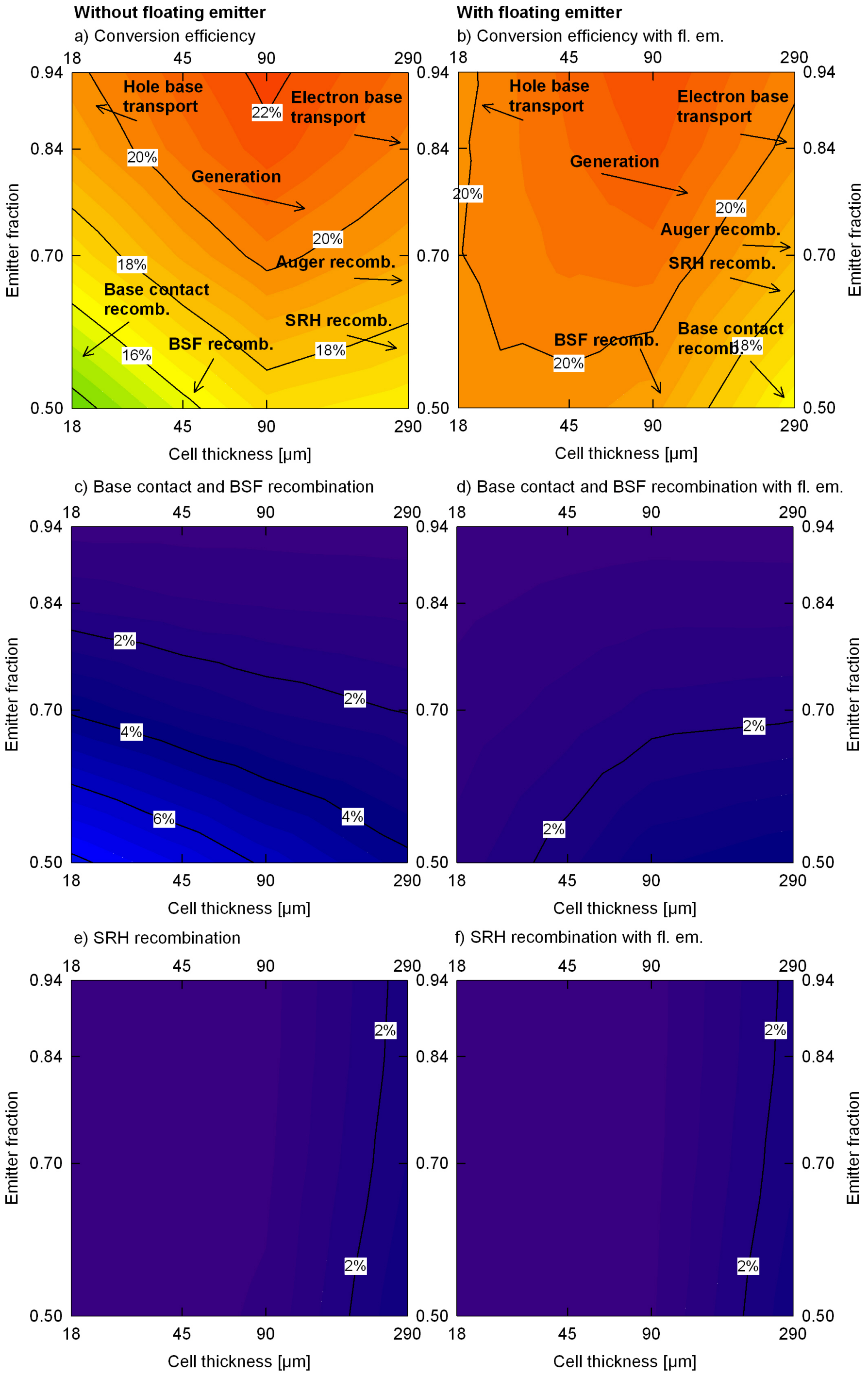

Without floating emitter

With floating emitter

a) Conversion efficiency

b) Conversion efficiency with fl. em.

c) Base contact and BSF recombination

d) Base contact and BSF recombination with fl. em.

e) SRH recombination

f) SRH recombination with fl. em.

Figure 8.4: *Conversion efficiency and main power losses in absolute efficiency points for a bulk lifetime of* 200 μs*. The results with and without floating emitter are shown. The conversion efficiency as well as the power losses are plotted as a function of cell thickness and emitter fraction. We indicate the impact of the free energy of generation as well as loss mechanisms by arrows in the conversion efficiency plots.*

to an increased minority carrier concentration, which is a result of the decreased SRH-recombination and the corresponding higher bulk diffusion lengths of 688 μm and 2660 μm, respectively, as shown in Figure 8.4e and f. The SRH-recombination causes less than 0.2 % absolute efficiency loss for a bulk lifetime of 3000 μm. As already observed at lower lifetimes the rear recombination at the base contact and BSF increases with decreasing cell thickness. By the implementation of a floating emitter these losses are decreased for thin cells, as shown in Figure 8.4d and Figure 8.5d, respectively. The conversion efficiency of cells with a floating emitter are less dependent on cell thickness and emitter fraction. The efficiency for lower emitter fractions is increased. However, a floating emitter enables the highest efficiencies of more than 22.5 % (at an emitter fraction of 0.94, a cell thickness of 290 μm and a bulk lifetime of 3000 μm) whereas the highest efficiency for cells without floating emitter is reduced to less than 22 %. We experimentally achieve 21.1 % at an emitter fraction of 0.84, a cell thickness of 90 μm and a bulk lifetime of 3000 μs as well as 21.8 % at an emitter fraction of 0.84, a cell thickness of 290 μm and a bulk lifetime of 3000 μs without using a floating emitter as shown in Figure 8.5a.

At a cell thickness of 290 μm and a bulk lifetime of 3000 μs Auger recombination is also a limiting loss mechanism. Since Auger recombination is proportional to $(n \times p^2)$ it decreases by a factor of about 9 at low level injection, when decreasing the base doping p by a factor of 3 (i.e. from $3 \times 10^{16}\,\mathrm{cm}^{-3}$ to $1 \times 10^{16}\,\mathrm{cm}^{-3}$). At a base doping of $1 \times 10^{16}\,\mathrm{cm}^{-3}$ efficiencies of more than 23 % are possible. At a doping density of $1 \times 10^{16}\,\mathrm{cm}^{-3}$, a bulk lifetime of 4000 μs and an emitter fraction of 0.84, we experimentally achieve 22.5 % on a cell thickness of 290 μm as well as 22.6 % on a cell thickness of 130 μm without using of a floating emitter.

In summary, at high bulk lifetimes of more than 200 μs and low emitter fraction the base contact and BSF recombination have to be reduced or a floating emitter has to be implemented. On the other hand, the highest efficiencies of more than 23 % are predicted for high emitter fractions without using a floating emitter and by reducing the base doping to $1 \times 10^{16}\,\mathrm{cm}^{-3}$.

In conclusion, the simulation study shows that the maximum efficiency increases and shifts from thin cells to thick cells with increasing bulk lifetime. BSF and base contact recombination losses increase with decreasing emitter fraction and are reduced by the implementation of a floating emitter. A floating emitter reduces the loss by electrical shading to less than 1 % absolute and thus 4 % relative. This is still in the same order of magnitude as the optical shading by a metal grid of a two side contacted cell. Therefore recombination losses at the base finger and the BSF have to be reduced further to gain higher efficiencies than the two side contacted solar cells.

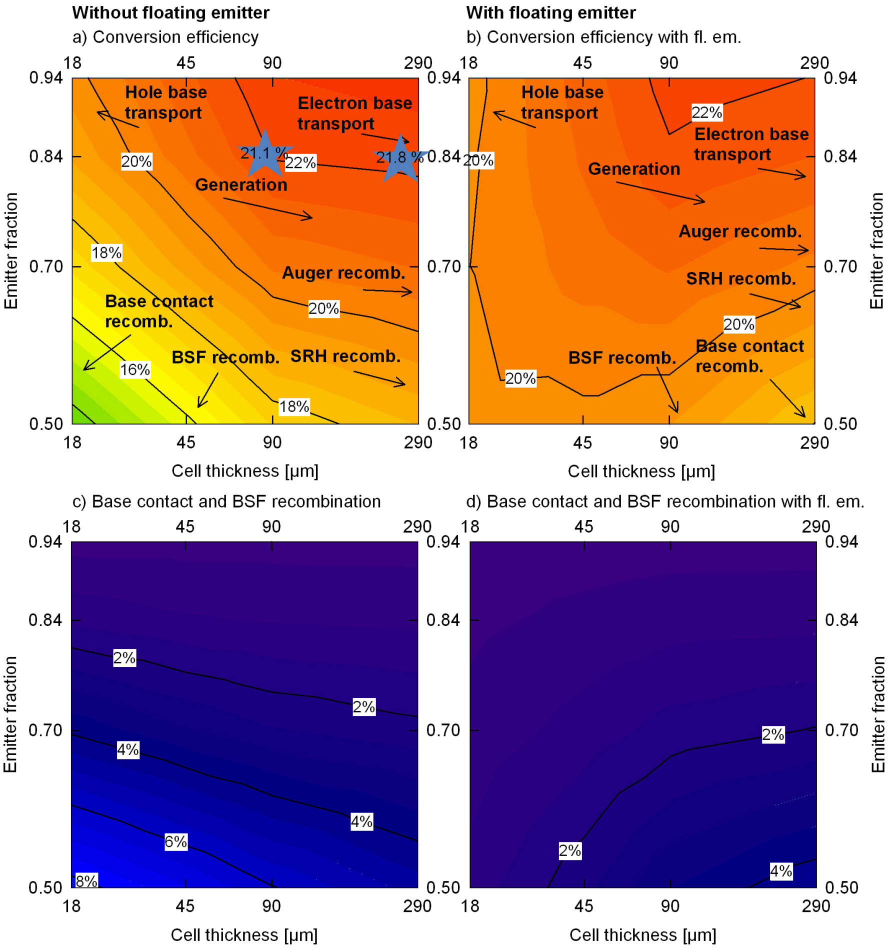

Figure 8.5: *Conversion efficiency and main power losses in absolute efficiency points for a bulk lifetime of* 3000 *μs. The results with and without floating emitter are shown. The conversion efficiency as well as the power losses are plotted as a function of cell thickness and emitter fraction. We indicate the impact of the free energy of generation as well as loss mechanisms by arrows in the conversion efficiency plots. The experimentally achieved efficiency of* 21.1 % *at a cell thickness of* 90 *μm and* 21.8 % *at a cell thickness of* 290 *μm are marked in plot (a).*

9 Summary

This work presents for the first time a loss analysis of thin-film monocrystalline back-contact back-junction silicon solar cells. We apply this loss analysis to a BC BJ PSI solar cell that has an energy conversion efficiency of 7.9 % and identify the limiting loss mechanisms as: (1) reduced power generation, resulting from a planar front surface, (2) low bulk lifetime, and (3) high recombination at the base contact. The planar surface limits the generated free energy to 19.1 % efficiency points. The low bulk lifetime of 3 μs caused by SRH recombination reduces the efficiency by 5.3 % absolute efficiency points, while the high saturation current density of 50000 fA cm^{-2} at the base contact leads to an efficiency loss of 2.5 % absolute. In an improved cell concept we implement a texture for enhanced light trapping, increasing the generated free energy to 23.2 % efficiency points. A higher bulk lifetime of 20 μs, achieved by using an improved epitaxial layer reduces the power loss by SRH recombination to 0.8 % absolute. The saturation current density at the base contact is reduced to 850 fA cm^{-2} by reducing the minority carrier concentration a the contacts with the implementation of a highly doped BSF. This reduces the efficiency loss by contact recombination to 0.5 % absolute. These changes require an adapted process flow with a free-standing thin layer. The adapted process flow led to the fabrication of a BC BJ cell with an increased conversion efficiency of 18.8 %.

The analysis is based on investigations on the generation, recombination, and series resistances in the cell device. The first step is the investigation of the generation in thin solar cell. For this, measurements of cells are compared to simulations, which use the optical properties of the different components of the solar cells as input parameters. We find, that using an appropriate light trapping, 87 % of the incoming light is absorbed in the bulk layer. 8 % of the light is reflected and the rest is absorbed in the dielectric layers and at the metalized rear side. Secondly the recombination at the surfaces of the solar cell as well as in the bulk is determined on test samples which are processed in parallel to the cells.

The infrared lifetime mapping technique allows for a spatially resolved measurement of the lifetime of non-metalized as well as of metalized samples. This technique is used for the measurement of the partly metalized samples for the determination of the saturation current densities and surface recombination velocities at the silicon/metal interfaces. Since the cells are in low injection at the maximum power point surface recombination velocities can be calculated in terms of saturation current densities. The analysis reveals that surface recombination velocities as well as saturation current densities are injection independent. However, the saturation current density increases with decreasing base doping density. Metalized and unpassivated base surfaces yield the same saturation current densities. The saturation current density is 50000 fA cm^{-2} at a base doping of 3×10^{16} cm^{-3} and 800000 fA cm^{-2} at a base doping of 1.5×10^{15} cm^{-3}. The recombination at these surfaces is limited by the diffusion of the carriers to the contact and thus the saturation current densities are lower limits. The saturation current density of a $100\,\Omega/\Box$ emitter increases from $110\,\mathrm{fA\,cm^{-2}}$ (passivated) to about $5000\,\mathrm{fA\,cm^{-2}}$ (metalized). The saturation current density of a $70\,\Omega/\Box$ emitter meanwhile increases only from $80\,\mathrm{fA\,cm^{-2}}$ to about $900\,\mathrm{fA\,cm^{-2}}$. For a base contact without BSF the saturation current density of a base contact without BSF increases from $6\,\mathrm{fA\,cm^{-2}}$ to about $50000\,\mathrm{fA\,cm^{-2}}$, whereas it increases only from $260\,\mathrm{fA\,cm^{-2}}$ to about $850\,\mathrm{fA\,cm^{-2}}$ with a BSF at the base contact.

The bulk lifetimes of some samples cannot be measured by measuring a carrier decay in a passivated sample due to the DRM modulation [38]. With certain boundary conditions it is possible to analyze the minority carrier diffusion length by evaluating electroluminescence measurements. Since the cell thickness is only about $30\,\mu$m and the unit cell is $500\,\mu$m wide, the current flow in the base region of the epitaxial layer can be assumed to be parallel to the cell surface. The minority carrier concentration decreases exponentially with increasing the distance to the emitter edge due to the SRH recombination in the bulk. A diffusion length of the minority carriers is extracted from this decay. This method works for thin planar cells with wide base fingers and low bulk lifetimes.

In a third step the resistances of each part of the cell are determined. The resistances, respectively the doping concentrations of the cells, are determined by four point probe measurement. The contact resistance of the silicon/metal interface is determined by the transfer length method. The specific contact resistance at the base contact increases by a factor of 10, if the base doping is decreased by a factor of 20.

After the investigations on all recombination paths and resistances in the cell these parameters are the input for unit cell simulations as well as resistance network simulations. The unit cell is simulated by a finite element simulation with the conductive boundary model (CoBo) [12] that is implemented by using COMSOL [55]. The free energy loss analysis is used for calculating power losses of every single loss in the maximum power point of the solar cell. This simulation reveals the limiting loss mechanisms in the unit cell. A resistance network simulation accounts for the series resistances between the unit cells. The simulation is performed with the user interface SpiceGUI [58] which uses the software LT-Spice [57]. Only one finger of the cell is simulated since the busbar is wide and introduces nearly no resistance losses. A power loss analysis is also performed at the maximum power point of the resulting J-V curves. The highest resistance losses appear at low base doping concentrations of $1.5 \times 10^{15}\,\mathrm{cm^{-3}}$ combined with long distances in the base, for example due to a broken line contact layout, which causes up to $2.2\,\%$ absolute efficiency loss. Large area cells with finger lengths of 88 mm also suffer from the resistance losses in the aluminum fingers contacting the base, which have a cross section of $0.825 \times 10^3\,\mathrm{mm^3}$ leading to an absolute efficiency loss of $0.3\,\%$. However, after taking into account the information obtained in this work, the sum of all resistance losses are reduced to $0.28\,\%$ absolute efficiency loss in the improved cell concept developed in this work.

Finally the simulated and measured J-V curves as well as the simulated and measured quantum efficiencies are compared. The combination of measured J_{SC}-V_{OC} curves with a network simulation shows only small deviations to the measured light J-V curves. The power densities of these curves agree within an uncertainty of 2.6 %. The combination of the unit cell simulation with the network simulation shows slightly higher deviations to the measured light J-V curves, which can be explained by non ideal recombination in the real solar cell, which are not taken into account in the simulations. An underestimation of the series resistances in the unit cell simulations.

In the end we study the conversion efficiency in dependence on the cell thickness as well as on the limiting loss mechanisms (SRH recombination and electrical shading). The simulation study is based on measured parameters which are varied in a physically and technologically reasonable range. The simulation study shows an increasing efficiency with increasing cell thickness and a shift of the maximum efficiency from thin cells to thick cells with increasing bulk lifetime. BSF and base contact recombination losses increase with decreasing emitter fraction and are reduced by the implementation of a floating emitter. A floating emitter reduces the loss by electrical shading to less than 1 % absolute and thus 4 % relative. However, this is still in the same order of magnitude as the optical shading by a front metal grid of a two side contacted cell. Therefore recombination losses at the base finger and the BSF have to be reduced further to gain higher efficiencies than with two side contacted solar cells.

This work analyzes the different loss mechanisms in thin-film monocrystalline back-contact back junction silicon solar cells. The analysis allows for increasing all parameters of the light J-V curve, resulting in an improved cell concept with a experimentally achieved conversion efficiency of 18.8 %. Simulations based on the measured recombination values predict a potential of more than 21 % for 45 μm thin epitaxial layer cells and a bulk lifetime of 200 μs.

A Layer selective laser ablation

Section 6.2 showed that a main loss mechanism in the BC BJ PSI cells is the base contact recombination, especially if no BSF is implemented. A BSF reduces the recombination at this contact as also shown in Section 6.2. An alternative process to the implementation of a BSF is the formation of the base contact by a process which induces nearly no additional defects. Various techniques exist to form local metal contacts to silicon that is surface passivated by dielectric layers. Laser fired contact [60] (LFC) formation is one approach. After full area evaporation of metal on top of a dielectric layer, commonly aluminum, a local contact formation is realized by firing the metal through the dielectric. This approach is well suited for contacting the solar cell base but fails for contacting thin emitters because shunts or crystallographic defects within the depletion region of the pn-junction are introduced. An alternative approach for local contacting is to open the dielectric layer before metallization. This can either be done by etching after masking by ink-jet printing [61] or by direct laser ablation [62]. While ink-jet printing consists of at least three process steps, laser ablation consists of only one. However, laser ablation is challenging since the laser light is not only absorbed in the dielectric layer but also in the silicon substrate. Detailed investigations of laser ablated single silicon dioxide (SiO_2) and silicon nitride (SiN_x) layers revealed the occurrence of crystal defects within a depth of about 20 nm in the laser treated areas [63]. Aiming at contacting thin emitters it is indispensable to avoid any damage of the silicon substrate to minimize the risk for shunt formation. Krister Mangersnes et al. already showed a damage free process to ablate a SiO_2 layer from a 500 nm thick amorphous silicon buffer layer [64]. However they conclude this process would be more relevant with thinner buffer layers due to their long deposition time.

Using the COSIMA [11] approach local contacts are formed to silicon passivated by a hydrogenated amorphous silicon (a-Si:H) by means of annealing. After local evaporation of aluminum low resistive contacts form by annealing at around 300 °C in air by dissolution of the a-Si:H underneath the Al layer. Unfortunately, this process requires masking during the evaporation process.

This work for the first time combines full area metallization with the local COSIMA contacting scheme. The approach is based on a layer selective ablation (LASA) of silicon nitride from a stack system consisting of a SiN_x layer on top of a-Si. By laser ablation the SiN_x is removed locally. After full area metallization the SiN_x acts as a diffusion barrier for the aluminum. In a subsequent annealing step at 300 °C the COSIMA contacts to the silicon substrate then only form in the laser treated areas.

In the following the functionality of the LASA process is described and the requirements that have to be fulfilled are discussed. The formation of COSIMA contacts and its electrical properties are investigated. Finally, the structure of the LASA contact openings is analyzed by scanning electron microscopy (SEM) and transmission electron microscopy (TEM).

A.1 The layer selective laser ablation process

The LASA process is demonstrated on monocrystalline silicon (c-Si) p-type FZ wafers with a doping density of $10^{16}\,\mathrm{cm}^{-3}$ which serve as substrate. Figure A.1 sketches the sample. The surface of the samples is passivated by a double layer. The stack consists of 35 nm plasma enhanced chemical vapor deposited (PECVD) a-Si and a capping layer of 70 nm remote PECVD $\mathrm{SiN_x}$ layer. The capping layer has a refractive index of 2.8. We apply a $\mathrm{Nd : YVO_4}$ laser with a pulse length of 8 to 9 ps (full duration at half maximum) and a wavelength of 355 nm. The laser beam has a rotationally symmetric Gaussian profile with a beam radius of 32 μm. The radius is defined by an intensity decline of a factor of $\exp(-2)$. The diameter of the ablated spots is about 20 μm. We find the ablation threshold at an average laser fluence of $H_{\mathrm{av}} = 0.095\,\mathrm{J\,cm^2}$. We find damage of the silicon substrate for an average laser fluence of $H_{\mathrm{av}} > 0.112\,\mathrm{J\,cm^2}$. Therefore an average laser fluence of $H_{\mathrm{av}} = 0.096\,\mathrm{J\,cm^2}$ is used in the following if not stated elsewise.

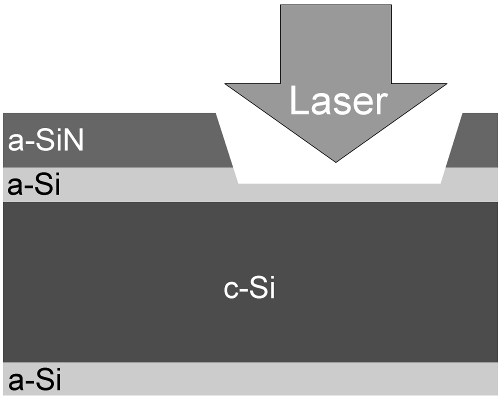

Figure A.1: *Schematic of the selective laser ablation of* $\mathrm{SiN_x}$ *from a-Si:H.*

A.2 Characterization

In order to demonstrate that the selective laser ablation is damage free and that local contacts with a low resistivity are forming during the process, we perform two experiments. First the selectivity is shown by local effective carrier lifetime measurements by means of the microwave detected photoconductance decay (MW-PCD) method before and after laser treatment. Secondly the measurement of the contact resistance using the transfer length method shows the low resistivity of the contacts. Scanning electron microscopy (SEM) shows the structure of the opened contact and its surrounding whereas transmission electron microscopy (TEM) investigates details of the contact opening proving the selectivity of the process.

A.2.1 Electrical characterization

The electrical characterization consists of two parts. The first part shows that an a-Si layer remains after the process which is still passivating the sample with the same electrical quality. The second part shows that the $\mathrm{SiN_x}$ layer is removed completely after the process so that an evaporated aluminum is able to form an ohmic COSIMA contact to the c-Si sample.

To demonstrate the selective laser ablation we perform lifetime measurements on $3 \times 3\,\mathrm{cm}^2$ monocrystalline p-type float zone silicon (FZ) samples having a resistivity of $100\,\Omega\,\mathrm{cm}$ and a thickness of $300\,\mu\mathrm{m}$. The samples are prepared as described in Section A.1. For the lifetime evaluation it is important to treat a significantly high ratio of the whole area. For this the distance between two adjacent spots is $p = 33\,\mu\mathrm{m}$ so that $28\,\%$ of the area is laser treated. Full area processing on half of the sample is realized by scanning the laser beam across the sample.

Figure A.2 shows the effective lifetime mappings of the samples measured by the microwave-detected photoconductance decay (MW-PCD) technique. The left half of each sample serves as an untreated reference. The lifetime is not homogeneous across the samples due to the inhomogeneous passivation. In both regions of both samples the effective carrier lifetime exceeds values of $2000\,\mu\mathrm{s}$. No discontinuity between both regions is observed. This demonstrates that neither the bulk nor the passivating effect of the a-Si layer is degraded during the laser process.

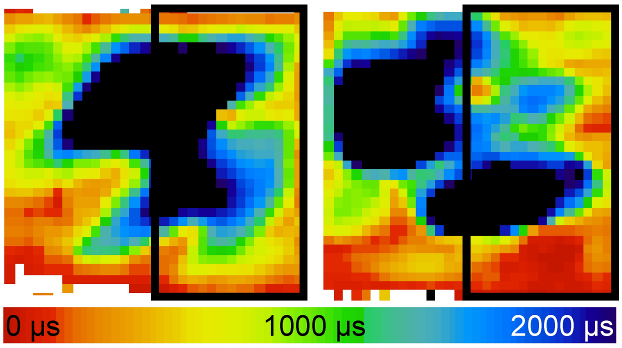

Figure A.2: *MW-PCD effective carrier lifetime mappings of two* $3 \times 3\,\mathrm{cm}^2$ *monocrystalline p-type float zone silicon (FZ) samples determined at a generation rate of about* $2 \times 10^{18}\,\mathrm{s}^{-1}\,\mathrm{cm}^{-3}$. *The right half of each sample is laser treated on full area. The left sample was treated by an average laser fluence of* $H_{\mathrm{av}} = 0.096\,\mathrm{J\,cm}^2$ *and the right sample by an average laser fluence of* $H_{\mathrm{av}} = 0.112\,\mathrm{J\,cm}^2$.

For the evaluation of the process window we vary the layer properties as well as the laser parameters. Table A.1 lists the parameter variations which are combined with each other. The sample preparation for this parameter variation is the same as shown except the resistivity of the material is now $0.5\,\Omega\,\mathrm{cm}$. The laser fluence was adjusted slightly above the ablation threshold of the $\mathrm{SiN_x}$ layer used. Figure A.3 shows the effective carrier lifetimes

Table A.1: *Parameter variations for the evaluation of the process window of LASA.*

Parameter	Values		
a-Si thickness [nm]	10	50	
SiN_x thickness [nm]	70	140	
SiN_x refractive index	1.9	2.4	2.8
laser pulse length [ps]	8	8000	
laser wavelength [nm]	355	532	
laser fluence	Ablation threshold		

of the samples after laser treatment. The samples are all passivated with 50 nm thick a-Si and treated by a laser with a pulse length of 8 ps.

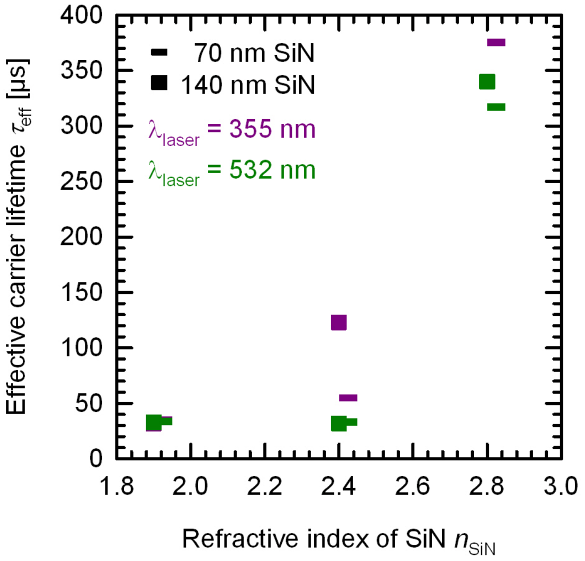

Figure A.3: *Effective carrier lifetimes of p-type float zone silicon (FZ) samples with a resistivity of* 0.5 Ω cm *after laser treatment. The wavelength of the laser is varied between* 355 nm *and* 532 nm*, the thickness of the* SiN_x *layer is varied between* 70 nm *and* 140 nm *and the refractive index is varied between 1.9 and 2.8.*

Figure A.3 shows tendencies in the parameters which allow for a selective ablation of the SiN_x layer. The first tendency is that the higher the refractive index of the SiN_x layer the higher the effective carrier lifetime after laser treatment. The second tendency is that the shorter the wavelength of the laser pulse the higher the effective carrier lifetime. Finally we find that the thicker the SiN_x layer the higher the effective carrier lifetime. This final tendency is only visible if a SiN_x layer with a refractive index of 2.4 is used.

All samples processed with a pulse length of 8000 ps show effective carrier lifetimes below 40 μs which indicates a poorly passivated surface as the non laser treated reference shows effective carrier lifetimes of 400 μs. Samples passivated with a 10 nm-thick a-Si layer or a $\mathrm{SiN_x}$ layer with a refractive index of 1.9 also show effective carrier lifetimes below 40 μs which indicates a poorly passivated surface.

The highest effective carrier lifetime is reached using short wavelength, a short pulse length, and a high refractive index of the $\mathrm{SiN_x}$ layer. The combination of these special parameters allows for an absorption of the laser fluence in the $\mathrm{SiN_x}$ layer and the upper part of the a-Si layer. Longer laser wavelength and lower refractive indices of $\mathrm{SiN_x}$ on the other hand have a greater absorption length, while longer pulse lengths heat the material to a greater depth. Since not all of the laser fluence is absorbed in the $\mathrm{SiN_x}$, the a-Si layer also has to be thick enough so that a part of the layer remains after the laser treatment. TEM investigations in Section A.2.3 confirm these results.

The second part of the electrical analysis is the verification of the complete removal of the $\mathrm{SiN_x}$ layer. To demonstrate the low resistivity of the local contacts, we perform contact resistance measurements on two different sets of samples being relevant to high efficiency silicon solar cells due to the low recombination in the samples. The first set consists of $3 \times 3\,\mathrm{cm^2}$ monocrystalline *p*-type float zone silicon samples having a resistivity of $1.5\,\Omega\,\mathrm{cm}$ and a thickness of 300 μm. For the second set the same wafers are used but in addition a phosphorous emitter diffusion is performed, resulting in a sheet resistance of $100\,\Omega/\Box$ with a surface doping density of $2 \times 10^{20}\,\mathrm{cm^{-3}}$. All samples of this experiment are covered by the same stack of dielectric layers as described in Section A.1. Again the $\mathrm{SiN_x}$ of each sample is locally ablated using the same parameter range and the same contact layout as in Section A.1. A wet chemical reference is processed by dipping the sample in HF to remove the $\mathrm{SiN_x}$ on the whole area. Aluminum fingers with a thickness of 5 μm, a width of 500 μm and spacing of 150 μm to 500 μm are evaporated on each sample. Finally the samples are annealed at 300 °C for 10 minutes. The contact resistance is measured by the transfer length method. The result is an average contact resistivity consisting of the contact resistivity of the metal/silicon interface and the metal/$\mathrm{SiN_x}$/a-Si/silicon interface. Assuming that the contact resistivity of the metal/$\mathrm{SiN_x}$/a-Si/silicon interface is infinite, the contact resistivity of the metal/silicon interface is calculated by area weighting.

The samples are measured at different current densities to confirm that the contacts are ohmic. The samples without a diffusion show a contact resistivity of $(3.8 \pm 0.2)\,\mathrm{m\Omega\,cm^2}$ (HF reference $(5.0 \pm 1.5)\,\mathrm{m\Omega\,cm^2}$) and the samples with a phosphorous diffusion show lower values of $(0.8 \pm 0.3)\,\mathrm{m\Omega\,cm^2}$ (HF reference $(1.1 \pm 0.3)\,\mathrm{m\Omega\,cm^2}$). These results confirm the applicability of the COSIMA approach for a low resistive local contact formation to silicon surfaces passivated by a $\mathrm{SiN_x}$/a-Si:H stack.

A.2.2 Scanning electron microscopy

After the demonstration of the good quality of the contact openings of the LASA process the structure of the contacts is investigated with scanning electron microscopy (SEM). Figure A.4 shows a SEM image of a tilted top view of a single LASA contact opening.

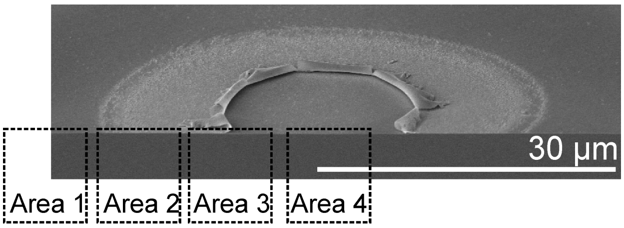

Figure A.4: *Scanning electron microscopy image of the selective laser ablation of* SiN_x *from a-Si:H. The areas of the transmission electron microscopy investigations are marked with boxes.*

The image shows 4 areas of the spot and the spot surroundings. Area 1 is the completely laser untreated area. Area 2 is already influenced by the laser irradiation and Area 3 is the edge of the opened area. Area 4 is the center region of the contact opening. Due to the Gaussian laser intensity beam profile the fluence of the laser light decreases from the center to the edge of the spot. In the center Area 4 the fluence is above the threshold fluence and ablates the SiN_x layer, whereas it is lower in Area 2 and only changes the structure of the SiN_x layer. Area 3 shows the edge of the SiN_x layer, which is turned around back on the passivation layer. This indicates a high gas pressure beneath the SiN_x layer directly after the absorption of the laser pulse in the SiN_x and a-Si layer. This plasma pressure lifts the SiN_x layer in Area 4 until the SiN_x layer breaks in Area 3 and is lifted off completely in Area 4.

The structure of the layers or layer stacks in Areas 1 to 4 cannot be analyzed with SEM. Therefore transmission electron microscopy (TEM) investigates these topics in the next section.

A.2.3 Transmission electron microscopy

Transmission electron microscopy (TEM) is capable of investigation of the structure of a material in the atomic scale and thus can distinguish between amorphous and crystalline materials. For the measurement a stabilization layer consisting of a carbon containing glue is deposited on the area of interest. A low voltage focused ion beam sputters a lamella perpendicular to the surface and electron transparence samples are obtained without damaging the samples.

Figure A.5 shows bright field TEM cross sectional micrographs of Areas 1 and 2 that are indicated in Figure A.4. Figure A.5a shows the layer stack of 35 nm a-Si and 70 nm SiN_x located in Area 1 with no laser treatment. The layers of Area 2 are only partially ablated due to a low laser fluence in the outer region of the Gaussian profile. Figure A.5b still shows the a-Si/SiN_x stack, but the structure of the upper part of each layer is porous. The presence of pores is confirmed by an energy dispersive X-ray analysis (EDX). The ratio of the intensity of the CKα peak over the intensity of the SiKα peak is much higher in the region of a pore. The CKα signal is caused by glue infiltration into the pore during the preparation process.

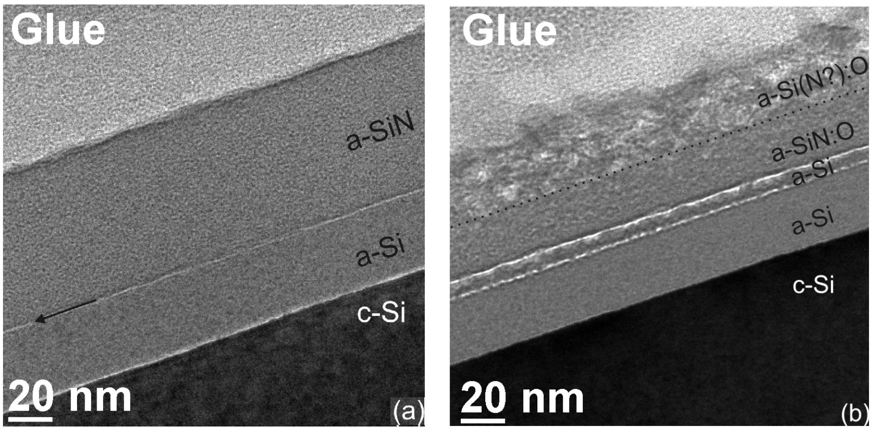

Figure A.5: *(a) TEM image of the reference Area 1 without laser treatment. (b) TEM image of Area 2 which is treated with a low fluence of the laser pulse.*

We interpret the formation of the stack structure composed of a-Si/porous a-Si/$\mathrm{SiN_x}$/porous $\mathrm{SiN_x}$ as follows: The laser fluence is partially absorbed in the $\mathrm{SiN_x}$ layer forming pores by sublimating the material. But a fraction of the laser light intensity passes through this layer and is absorbed at the a-Si layer that has a higher absorption coefficient than a $\mathrm{SiN_x}$ at a wavelength of 355 nm. Hence pores also form in the upper part of the a-Si layer.

Figure A.6 shows a 3 μm wide region composed from various bright field TEM images of Area 3. The laser fluence increases with decreasing distance to the centre of the laser spot (Figure A.6a through A.6g) due to the Gaussian profile. In Area 3 the gas pressure of the sublimated a-Si is high enough to remove the $\mathrm{SiN_x}$ top layer. Figure A.6d shows the edge of the $\mathrm{SiN_x}$ layer. Figures A.6e through A.6g represent Area 4, where no a $\mathrm{SiN_x}$ is left. Here the stack is c-Si/a-Si/porous a-Si.

High resolution TEM images demonstrate that the a-Si layer is purely amorphous and that the c-Si layer has no dislocations or other crystal defects. These layers are also not electronically degraded by the laser treatment as described in Section A.2.1. The LASA process thus removed the $\mathrm{SiN_x}$ layer selectively from the a-Si layer and the wafer surface remains passivated.

Therefore the LASA process is capable of forming local ohmic COSIMA contacts. This process is especially useful for contacting thin emitters since the c-Si is not influenced by this process.

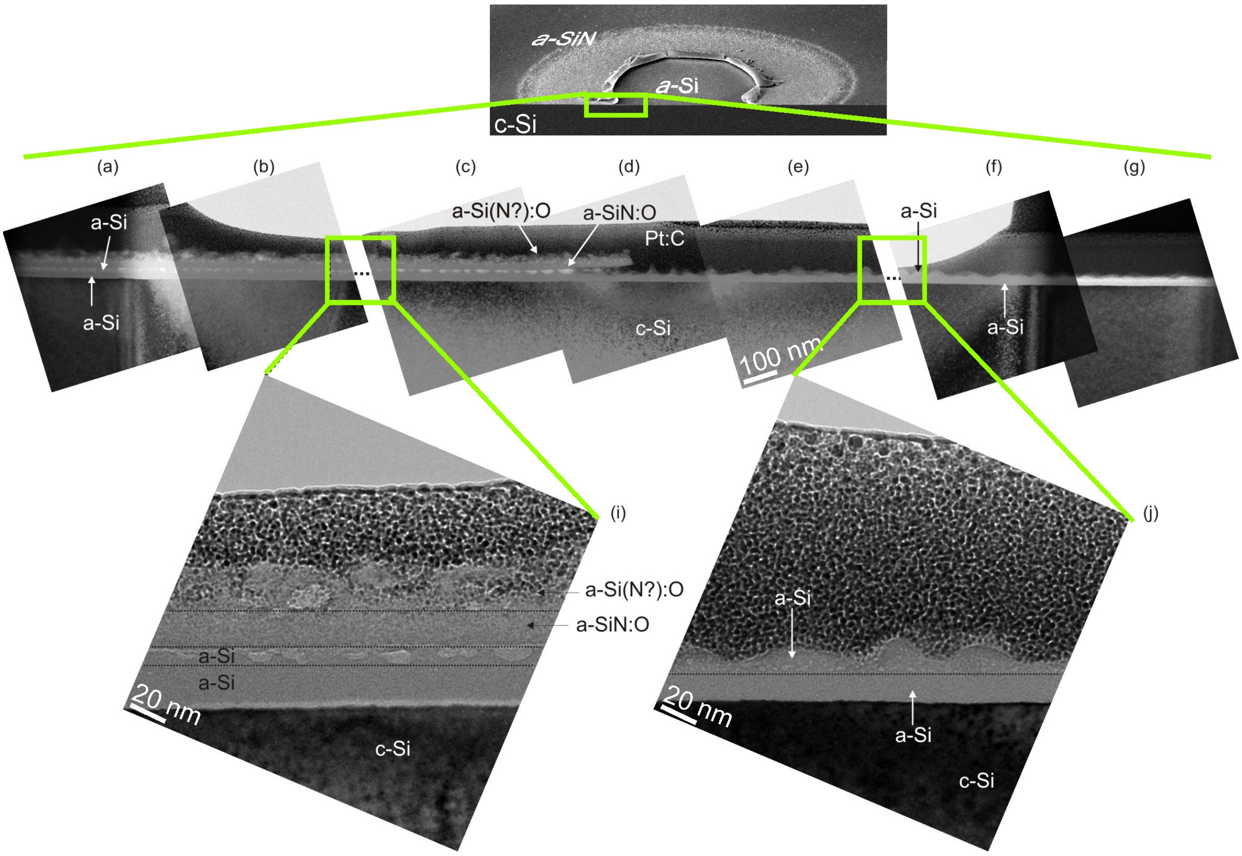

Figure A.6: *TEM images of Area 3. In images (a) to (c) and (i) a low laser fluence of the laser causes an a-Si/porous a-Si/SiN$_x$/porous SiN$_x$ layer stack. Image (d) shows the edge of the SiN$_x$ layer. In images (e) to (g) and (j) a higher laser fluence ablates the SiN$_x$ layer completely and a layer stack of a-Si/porous a-Si remains.*

References

[1] http://www.itrpv.net/, (accessed on March 19, 2012).

[2] D. M. Powell, M. T. Winkler, H. J. Choi, C. B. Simmons, D. Berney Needleman, and T. Buonassisi, Crystalline silicon photovoltaics: a cost analysis framework for determining technology pathways to reach baseload electricity costs, *Energy and Environmental Science* **5**, 5874 – 5883 (2012).

[3] http://www.appliedmaterials.com/, (accessed on Januar 24, 2012).

[4] R. Brendel, A novel process for ultrathin monocrystalline silicon solar cells on glass, *Proc. 14th EUPVSC*, p. 1354–1358 (1997).

[5] R. Horbelt, B. Terheiden, R. Auer, and R. Brendel, Demonstration of the manifold use of growth substrates in the porous silicon process, *Proc. 31st IEEE PVSC*, 1193–1196 (2005).

[6] T. Fuyuki, H. Kondo, Y. Kaji, A. Ogane, and Y. Takahashi, Analytic findings in the electroluminescence characterization of crystalline silicon solar cells, *Journal of Applied Physics* **101**(2), 023711 (2007).

[7] T. Trupke, E. Pink, R. A. Bardos, and M. D. Abbott, Spatially resolved series resistance of silicon solar cells obtained from luminescence imaging, *Applied Physics Letters* **90**(9), 093506 (2007).

[8] F. M. Smits, Measurement of sheet resistivities with the four-point probe, *Bell System Technical Journal* **37**, 711 (1958).

[9] G. K. Reeves and H. B. Harrison, Obtaining the specific contact resistance from transmission line model measurements, *IEEE Electron Device Letters* **3**, 111 (1982).

[10] R. Brendel, S. Dreissigacker, N.-P. Harder, and P. P. Altermatt, Theory of analyzing free energy losses in solar cells, *Applied Physics Letters* **93**(17), 173503 (2008).

[11] H. Plagwitz, M. Nerding, N. Ott, H. P. Strunk, and R. Brendel, Low-temperature formation of local Al contacts to a-Si:H-passivated Si wafers, *Progress in Photovoltaics: Research and Applications* **12**(1), 47–54 (2004).

[12] R. Brendel, Modeling solar cells with the dopant-diffused layers treated as conductive boundaries, *Progress in Photovoltaics: Research and Applications* **20**, 31–43 (2012).

[13] H. Tayanaka, K. Yamauchi, and T. Matssushita, Thin-film crystalline silicon solar cells obtained by separation of a porous silicon sacrificial layer, *Proc. 2nd World Conference on Photovoltaic Energy Conversion*, p. 1272 (1998).

[14] B. Terheiden, R. Horbelt, and R. Brendel, Thin-film solar cells and modules from the porous silicon process using 6" Si substrates, *Proc. 21st EUPVSEC*, p. 247 (2006).

[15] C. S. Solanki, R. R. Bilyalov, J. Poortmans, G. Beaucarne, K. Van Nieuwenhuysen, J. Nijs, and R. Mertens, Characterization of free-standing thin crystalline films on porous silicon for solar cells, *Thin Solid Films* **451 - 452**, 649 – 654 (2004). Proceedings of Symposium D on Thin Film and Nano-Structured Materials for Photovoltaics, of the E-MRS 2003 Spring Conference.

[16] M. Reuter, W. Brendle, O. Tobail, and J. H. Werner, 50 μm thin solar cells with 17.0 % efficiency, *Solar Energy Materials and Solar Cells* **93**(6 - 7), 704 – 706 (2009).

[17] J. H. Petermann, D. Zielke, J. Schmidt, F. Haase, E. Garralaga Rojas, and R. Brendel, 19 %-efficient and 43 μm-thick crystalline Si solar cell from layer transfer using porous silicon, *Progress in Photovoltaics: Research and Applications* **20**, 1–5 (2011).

[18] M. A. Green, K. Emery, Y. Hishikawa, W. Warta, and D. E. Dunlop, Solar cell efficiency tables (version 39), *Progress in Photovoltaics: Research and Applications* **20**(1), 12–20 (2012).

[19] R. Tait, A paste manufacturer's view of the hybrid industry, *Microelectronics Reliability* **21**(6), 801 – 811 (1981).

[20] M. Hermle, G. Filip, O. Schultz-Wittmann, and S. W. Glunz, Shading effects in back-junction back-contacted silicon solar cells, *Proc. 33rd IEEE PVSC*, p. 1064–1068 (2008).

[21] R. Brendel and R. Auer, Photovoltaic mini-modules from layer transfer by the porous silicon process, *Progress in Photovoltaics: Research and Applications* **9**(6), 439–443 (2001).

[22] S. Hermann, P. Engelhart, A. Merkle, T. Neubert, T. Brendemühl, R. Meyer, N.-P. Harder, and R. Brendel, 21.4 %-efficient emitter wrap-through rise solar cell on large area and picosecond laser processing of local contact openings, *Proc. 22nd EUPVSEC*, p. 247 (2007).

[23] R. A. Sinton, P. Verlinden, D. E. Kane, and R. M. Swanson, Development efforts in silicon backside-contact solar cells., *Proc. 8th EUPVSEC*, p. 1472 (1988).

[24] A. Hovinen, Fitting of the solar cell IV -curve to the two diode model, *Physica Scripta* **1994**(T54), 175 (1994).

[25] P. P. Altermatt, A. Schenk, F. Geelhaar, and G. Heiser, Reassessment of the intrinsic carrier density in crystalline silicon in view of band-gap narrowing, *Applied Physics Letters* **93**, 1598 (2003).

[26] H. Schlangenotto, H. Maeder, and W. Gerlach, Temperature dependence of the radiative recombination coefficient in silicon, *Physica Status Solidi A: Applications and Materials Science* **21**, 357 (1974).

[27] M. J. Kerr and A. Cuevas, General parameterization of Auger recombination in crystalline silicon, *Journal of Applied Physics* **91**, 2473 (2002).

[28] W. Shockley and W. T. Read, Statistics of the recombination of electrons and holes, *Physical Review* **87**, 835–842 (1952).

[29] R. N. Hall, Electron-hole recombination in germanium, *Physical Review* **87**, 387 (1952).

[30] M. A. Green, Intrinsic concentration, effective density of states, and effective mass in silicon, *Journal of Applied Physics* **67**, 2944 (1990).

[31] I. E. Tamm, Über eine mögliche Art der Elektronenbindung an Kristalloberflächen, *Physikalische Zeitschrift der Sowjetunion* **1**, 733 (1932).

[32] W. Shockley, On the surface states associated with a periodic potential, *Physical Review* **56**, 317 (1939).

[33] W. Mönch. *Semiconductor surfaces and interfaces*, chapter 9 and 14. Springer series in surface science. Springer-Verlag, Berlin/Heidelberg, 3rd Edition, (2001).

[34] B. Fischer, *Loss analysis of crystalline silicon solar cells using photoconductance and quantum efficiency measurements*, PhD thesis, University of Konstanz (2003). (Cuvillier Verlag) Chapter 4.

[35] T. Oredian, Separate contactless measurement of the bulk lifetime and the surface recombination velocity by the harmonic optical generation of the excess carriers, *Solid-State Electronics* **36**(2), 153–162 (1993).

[36] D. Macdonald and A. Cuevas, Trapping of minority carriers in multicrystalline silicon, *Applied Physics Letters* **74**(12), 1710–1712 (1999).

[37] M. Bail, M. Schulz, and R. Brendel, Space-charge region-dominated steady-state photoconductance in low-lifetime Si wafers, *Applied Physics Letters* **82**(5), 757–759 (2003).

[38] P. J. Cousins, D. H. Neuhaus, and J. E. Cotter, Experimental verification of the effect of depletion-region modulation on photoconductance lifetime measurements, *Journal of Applied Physics* **95**(4), 1854–1858 (2004).

[39] P. P. Altermatt, J. Schmidt, M. Kerr, G. Heiser, and A. G. Aberle, Exciton-enhanced Auger recombination in crystalline silicon under intermediate and high injection conditions, *Proc. 16th EUPVSEC*, p. 247 (2000).

[40] H. Nagel, C. Berge, and A. G. Aberle, Generalized analysis of quasi-steady-state and quasi-transient measurements of carrier lifetimes in semiconductors, *Journal of Applied Physics* **86**, 6218 (1999).

[41] K. Ramspeck, *Characterization techniques for silicon solar cells and material using an infrared-camera based approach*, PhD thesis, Institute for Solar Energy Research Hamelin (ISFH) (2009). Chapter 4.

[42] K. Ramspeck, S. Reissenweber, J. Schmidt, K. Bothe, and R. Brendel, Dynamic carrier lifetime imaging of silicon wafers using an infrared-camera-based approach, *Applied Physics Letters* **93**(10), 102104 (2008).

[43] R. Brendel, Note on the interpretation of injection-level-dependent surface recombination velocities, *Applied Physics A* **60**, 523 (1995).

[44] J. Schmidt, Measurement of differential and actual recombination parameters on crystalline silicon wafers, *IEEE Transactions on Electron Devices* **46**, 2018 (1999).

[45] D. E. Kane and R. M. Swanson, Measurement of the emitter saturation current by a contactless photoconductivity decay method, *Proc. 18th IEEE PVSC*, p. 578 (1985).

[46] E. Yablonovitch, D. L. Allara, C. C. Chang, T. Gmitter, and T. B. Bright, Unusually low surface-recombination velocity on silicon on germanium surfaces, *Physical Review Letters* **57**, 249 (1986).

[47] J. Müller, K. Bothe, S. Gatz, F. Haase, C. Mader, and R. Brendel, Recombination at laser-processed local base contacts by dynamic infrared lifetime mapping, *Journal of Applied Physics* **108**(12), 124513 (2010).

[48] B. Fischer, *Loss analysis of crystalline silicon solar cells using photoconductance and quantum efficiency measurements*, PhD thesis, University of Konstanz (2003). (Cuvillier Verlag) Chapter 2.3.

[49] P. P. Altermatt, S. Steingrube, Y. Yang, C. Sprodowski, T. Dezhdar, S. Koc, B. Veith, S. Herrman, R. Bock, K. Bothe, J. Schmidt, and R. Brendel, Highly predictive modelling of entire Si solar cells for industrial applications, *Proc. 24th EUPVSEC*, p. 901 (2009).

[50] J. D. Cutnell and K. W. Johnson, *Physics 3rd Edition*, John Wiley & Sons Inc. (1995).

[51] R. Brendel, Sunrays: a versatile ray tracing program for the photovoltaic community., *Proc. 12th EUPVSC*, p. 1339–1342 (1994).

[52] E. D. Palik. *Handbook of optical constants of solids*, 400, 759, 761. Academic Press, (1985).

[53] M. A. Green. *High Efficiency Cells*, p. 228. Trans Tech Publications, (1987).

[54] R. L. Hulstrom, R. E. Bird, and C. J. Riordan, Spectral solar irradiance data sets for selected terrestrial conditions, *Solar cells* **15**, 365 (1985).

[55] COMSOL 3.5, (2009).

[56] S. Eidelloth, U. Eitner, S. Steingrube, and R. Brendel, Open source graphical user interface in Matlab for two dimensional simulations solving the fully coupled semiconductor equations using COMSOL, *Proc. 25th EUPVSEC*, 2477–2485 (2010).

[57] LTspice IV, (accessed on Feb. 16, 2011).

[58] S. Eidelloth, F. Haase, and R. Brendel, Simulation tool for equivalent circuit modeling of photovoltaic devices, *IEEE Journal of Photovoltaics* **2 (4)**, 572–579 (2012).

[59] K. Bothe, P. Pohl, J. Schmidt, T. Weber, P. P. Altermatt, B. Fischer, and R. Brendel, Electroluminescence imaging as an in-line characterisation tool for solar cell production., *Proc. 21st EUPVSEC*, 1024 – 1027 (2006).

[60] E. Schneiderlöchner, R. Preu, R. Lüdemann, and S. W. Glunz, Laser-fired rear contacts for crystalline silicon solar cells, *Progress in Photovoltaics: Research and Applications* **10**(1), 29–34 (2002).

[61] N. Mingirulli, R. Keding, J. Specht, A. Fallisch, D. Stüwe, and D. Biro, Hot-melt inkjet as masking technology for back-contacted cells, *Proc. 34th IEEE PVSC*, p. 1064–1068 (2009).

[62] P. Engelhart, N.-P. Harder, T. Horstmann, R. Grischke, R. Meyer, and R. Brendel, Laser Ablation of Passivating $\mathrm{SIN_x}$ Layers for Locally Contacting Emitters of High-Efficiency Solar Cells, *Conference record of IEEE 4th World conference*, 1024 – 1027 (2006).

[63] S. Hermann, T. Dezhdar, N.-P. Harder, R. Brendel, M. Seibt, and S. Stroj, Impact of surface topography and laser pulse duration for laser ablation of solar cell front side passivating $\mathrm{SiN_x}$ layers, *Journal of Applied Physics* **108**(11), 114514 (2010).

[64] K. Mangersnes, S. E. Foss, and A. Thogersen, Damage free laser ablation of $\mathrm{SiO_2}$ for local contact opening on silicon solar cells using an a-Si:H buffer layer, *Journal of Applied Physics* **107**(4), 043518 (2010).

List of Figures

List of publications

Publications arising from the work in this thesis:

Refereed journal papers

1. J. Müller, K. Bothe, S. Gatz, F. Haase, C. Mader, and R. Brendel, Recombination at laser-processed local base contacts by dynamic infrared lifetime mapping, *Journal of Applied Physics* **108**, 124513 (2010)
2. F. Haase, T. Neubert, R. Horbelt, B. Terheiden, K. Bothe, and R. Brendel, Local aluminum–silicon contacts by layer selective laser ablation, *Solar Energy Materials and Solar Cells* **95**, 2698–2700 (2011)
3. F. Haase, S. Eidelloth, R. Horbelt, K. Bothe, E. Garralaga Rojas, and R. Brendel, Loss analysis of back-contact back-junction thin-film monocrystalline silicon solar cells, *Journal of Applied Physics* **110**, 124510 (2011)
4. J. H. Petermann, D. Zielke, J. Schmidt, F. Haase, E. Garralaga Rojas, and R. Brendel, 19%-efficient and 43 μm thick crystalline Si solar cell from layer transfer using porous silicon, *Progress in Photovoltaics: Research and Applications* **20**, 1–5 (2012)
5. S. Eidelloth, F. Haase, and R. Brendel, Simulation tool for equivalent circuit modeling of photovoltaic devices, *IEEE Journal of Photovoltaics* **2**, 4 (2012)

Refereed papers presented at international conferences

1. F. Haase, R. Horbelt, B. Terheiden, H. Plagwitz, and R. Brendel, Back-contact monocrystalline thin-film silicon solar cells from the porous silicon process, *Proceedings of the 34th IEEE Phototovoltaic Specialists Conference*, 244-246 (2009)
2. F. Haase, E. Garralaga Rojas, K. Bothe, and R. Brendel, Layer selective laser ablation for local contacts to thin emitters, *Energy Procedia* **8**, 577–580 (2011)
3. F. Haase, S. Eidelloth, R. Horbelt, K. Bothe, E. Garralaga Rojas, and R. Brendel, Loss analysis of back-contact back-junction thin-film monocrystalline silicon solar cells, *Proceedings of the 37th IEEE Phototovoltaic Specialists Conference*, 2874-2877 (2011)
4. F. Haase, R. Winter, S. Kajari-Schröder, M. Nese, and R. Brendel, High efficiency back-contact back-junction silicon solar cells with cell thicknesses of 45 μm, 90 μm, 130 μm and 290 μm, *Proceedings of the 27th EUPVSEC*, 580 - 585 (2012)

5. F. Haase, U. Römer, T. Neubert, J. H. Petermann, R. Peibst, N.-P. Harder, S. Kajari-Schröder, R. Brendel, Front side degradation of silicon solar cells by rear side laser processing, *Proceedings of the 22nd Photovoltaic Science and Engineering Conference*, (2012)
6. U. Römer, F. Haase, T. Neubert, J. H. Petermann, R. Peibst, N.-P. Harder, S. Kajari-Schröder and R. Brendel, Limits for short-pulse laser processing of high efficiency crystalline silicon solar cells on thin wafers, *Proceedings of the 22nd Photovoltaic Science and Engineering Conference*, (2012)

Patent application

1. B. Terheiden, F. Haase, and T. Neubert, Verfahren zur Herstellung eines Halbleiterbauelementes, insbesondere einer Solarzelle, mit einer lokal geöffneten Dielektrikumsschicht sowie entsprechendes Halbleiterbauelement *German patent application no. DE 10 2009 018 112.1-33*

Danksagung

Vielen Dank möchte ich all denen sagen, die zum Gelingen dieser Arbeit beigetragen haben. Besonders bedanken möchte ich mich bei

Prof. Dr.-Ing. Rolf Brendel für die Möglichkeit dieses spannende Thema im Rahmen einer Dissertation zu bearbeiten, für die wissenschaftliche Betreuung und für die stets sehr hilfreichen Anmerkungen bei wissenschaftlichen Veröffentlichungen,

Prof. Dr. H. Jörg Osten für die Übernahme des Korreferats und *Prof. Dr. Holger Frahm* für die Übernahme des Prüfungsvorsitzes bei meiner Disputation,

Dr. Barbara Terheiden, Dr. Heiko Plagwitz, Dr. Karsten Bothe, Dr.-Ing. Enrique Garralaga Rojas und Dr. Sarah Kajari-Schröder für die wissenschaftliche Betreuung meiner Arbeit und anregende Diskussionen,

Dr. Karsten Bothe, Dr. Sarah Kajari-Schröder und Dr. Bianca Lim für das Korrekturlesen meiner Arbeit,

dem PSI-Team bestehend aus Dr. Barbara Terheiden, Dr. Heiko Plagwitz, Dr.-Ing. Enrique Garralaga Rojas, Dr. Sarah Kajari-Schröder, Renate Horbelt, Renate Winter, Dörthe Schiewe, Jan Hensen, Verena Steckenreiter, Alwina Knorr, Jörg Käsewieter, Jan-Hendrik Petermann, Dr. Andreas Wolf, Julia Nehmann, Marita Steinhof, Chris Britze, Hilke Fischer und Manuel Startmann für die tolle Zusammenarbeit, für die Hilfe bei der Probenprozessierung und für eine Arbeitsatmosphäre, in der es Spaß gemacht hat zu arbeiten,

Renate Winter und Dörthe Schiewe für die exzellente Unterstützung bei der Prozessierung von Teststrukturen und vor allem hervorragenden Solarzellen,

Jan Hensen für die Porosizierung der Substratwafer,

Verena Steckenreiter für die Unterstützung beim Kleben, Passivieren und Plasmaätzen,

Jörg Käsewieter für die Unterstützung beim Ablösen der Epitaxieschichten,

Stefan Eidelloth für die äußerst Verständnis fördernden Diskussionen rund um Simulationen,

Martin Wolf, Arne Schmidt, Jens Müller, Sandra Herlufsen, Dr. Klaus Ramspeck und Dr. David Hinken für die Unterstützung bei Messungen von Solarzellen und Teststrukturen,

Tobias Neubert, Till Brendemühl, Peter Giesel und David Sylla für die Unterstützung bei verschiedensten Laserprozessen,

Prof. Dr. Pietro Altermatt für die Durchführung von DESSIS Simulationen zum Vergleich mit den CoBo Simulationen,

Agnes Merkle, Dr. Sonja Hermann und Dr. Peter Engelhardt für die hilfreichen Diskussionen bei der Planung von Test- und Zellchargen,

Stefan Beisse, Michael Weiß und Willy Gisecke für die kompetente Instandhaltung der Anlagen und Messtechnik.

Dr. Bianca Lim für die stete Bereitschaft alles Mögliche zu diskutieren und Probleme des Büroalltags zu lösen,

und allen anderen Kolleginnen und Kollegen am ISFH für das angenehme und freundliche Arbeitsklima.

Außerdem herzlichen Dank an *Dr. Erik Sauar, Dr. Martin Nese, Dr. Andreas Bentzen und Dr. Daniel Nilsen Wright* für die kreative Projektzusammenarbeit und der Renewable Energy Corporation (REC) für die Finanzierung des Projekts,

und an meine Frau Anne und meine Familie für die Unterstützung während dieser Zeit.

Persönliche Daten

Name	Felix Haase
Anschrift	Reherweg 46, 31787 Hameln
Geburtsdatum	18. August 1981
Geburtsort	Nürnberg
Nationalität	deutsch
Familienstand	verheiratet

Schulbildung

1988 - 1992	Grundschule Kersbach
1992 - 2001	Ehrenbürg-Gymnasium Forchheim Abschluss der allgemeinen Hochschulreife im Juni 2001

Universitätsausbildung

Oktober 2001 - März 2007	Friedrich-Alexander-Universität Erlangen-Nürnberg Studium der Physik Diplomprüfung im März 2007
September 2003 - Dezember 2003	University of Joensuu, Finnland Auslandssemester

Anstellung

seit April 2007	Institut für Solarenergieforschung (ISFH) Hameln/Emmerthal: Wissenschaftlicher Mitarbeiter im Bereich Si-Dünnschichtforschung